Empirical modelling of site-specific errors in GPS observations

Michael Moore

A thesis submitted for the degree of
Doctor of Philosophy
of The Australian National University

June 2016

Except where otherwise indicated, this thesis is my own original work.

Michael Moore
21 June 2016

Acknowledgments

First of all I'd like to thank Simon McClusky for his unwavering support and for sharing his passion for Geodesy. Simon has been much more than just a supervisor, and I'll forever be grateful for his help. I would also like to thank my co-supervisors Paul Tregoning, Christopher Watson, and John Dawson for their help and encouragement throughout my PhD studies. Matt King for his help with publishing a paper on the ESM technique.

I owe a special thanks to Geoscience Australia for supporting me through my PhD studies at ANU, and in particular Barry Drummond and Gary Johnston who made sure I was in a position to have this opportunity. This research was undertaken on the NCI National Facility in Canberra, Australia, which is supported by the Australian Commonwealth Government.

I would like to thank the postdocs and PhD candidates at ANU that helped to make it an enjoyable experience, in particular Achraf, Sebastien, Salim and Jean-Phillipe.

I would like to thank my family, and in particular my two daughters Alison and Elizabeth, for keeping me grounded and the endless hugs. Finally I'd like to thank my wife Jess for her love, encouragement and support.

Abstract

GPS is an essential element of the global geo-spatial information infrastructure, it is free, open and dependable. Precise positioning and navigation enabled by GPS has led to the development of hundreds of applications affecting every aspect of modern life, and is now found in everything from mobile phones to bulldozers.

Underpinning the day-to-day operation of GPS is the International Terrestrial Reference Frame (ITRF). Without an accurate earth-centred, earth-fixed reference frame, such as ITRF, it would not be possible to accurately determine station location and position as a function of time. To achieve an accurate reference frame precise models of all aspects of the GPS system are required, including; the satellites, their orbits, the signal propagation medium, the ground receivers and antennas, and the orientation and motion of the Earth's crust.

For more than two decades GPS observations have been integral to the determination of the ITRF. GPS is the critical technique that provides the connection, through collocation, between other terrestrial observation systems, SLR and VLBI necessary to define accurately the origin, orientation and scale of the ITRF. GPS solutions provide the most precise and accurate estimates of polar motion, and is the geodetic technique most commonly used to access the ITRF. The main weaknesses of GPS observations today are due to unmodelled site-specific errors, particularly at collocated stations, orbit mismodelling errors (such as solar radiation pressure), errors in the conventional model for diurnal and semi-diurnal variations in Earth orientation due to ocean tides [Griffiths and Ray, 2013], and an under-determined TRF scale due to uncalibrated satellite antenna phase centre offsets

Analysis and modelling techniques have continuously been refined and improved. Despite these advances there has been little progress on addressing site-specific biases in GPS processing. In this thesis we are mainly concerned with site-specific biases due to reflections of the incoming GPS signal, as well as errors in the antenna model. These site-specific errors can alias into the GPS station position time series producing time-correlated errors which do not average out over time. The result is a GPS time series which will have unmodelled biases that can affect the interpretation of geophysical signals. This is particularly a problem for reference frames if there are site-specific biases at GPS stations used to collocate the different observation techniques.

This thesis presents a methodology that can account for site-specific errors at the

observational level, which is applicable to historic and future data sets. The technique relies on using carrier phase residuals obtained from the processing of a large network of GPS stations. These residuals are then used to model the errors at individual stations, and those associated with individual satellites. We have investigated the applicability of carrier phase residuals to model site-specific biases, through the use of simulations. The technique has then been tested and verified by applying the models to short-baseline kinematic solutions for 3 different collocation stations. We also investigate the impact of applying the model to large global solutions, in particular we investigate the impact upon coordinate and velocity estimates as well as orbit and clock products, key products used to access and determine the reference frame.

Contents

Acknowledgments **v**

Abstract **vii**

1 Introduction **1**
1.1 Thesis outline . . . 2
1.2 Site-specific error sources . . . 3
1.2.1 Antennas characteristics . . . 3
1.2.2 Antenna calibration . . . 4
1.2.3 Antenna calibration errors . . . 6
1.2.4 Radomes . . . 7
1.2.5 Satellite antennas . . . 10
1.3 Multipath errors . . . 12
1.3.1 Theory . . . 13
1.3.2 Multipath model . . . 14
1.4 Summary . . . 15

2 Background, theoretical basis and methodology **17**
2.1 Related work . . . 17
2.2 Theoretical basis . . . 20
2.3 Reference solution . . . 23
2.3.1 GPS data modelling and processing scheme . . . 24
2.3.2 Process strategy . . . 24
2.3.3 Orbit estimation . . . 27
2.3.4 Clock estimation . . . 28
2.4 Time-series analysis techniques . . . 29
2.4.1 Wavelets . . . 29
2.4.2 Nature of noise in GPS time series . . . 33
2.5 Summary . . . 34

3 Impact of site-specific errors **35**
3.1 Simulator . . . 35
3.2 Short-term impact of site-specific errors . . . 36

3.2.1 Observed satellite elevation angle and antenna height 36
3.2.2 Multipath estimation error 36
3.2.3 Interaction of multipath with weighting and mapping functions 39
3.2.4 Processing parameters 39
3.2.5 Elevation cut-off angle 42
3.2.6 Frequency of position estimates 43
3.2.7 Influence of station location 43
3.2.8 Antenna 44
3.2.9 Radomes 45
3.2.10 Pillar width 48
3.3 Long term effects of multipath 48
3.3.1 Noise models 49
3.3.2 Monument height 49
3.3.3 Antenna calibration uncertainty 52
3.3.4 Uncalibrated radome 55
3.3.5 Variation with latitude 57
3.3.6 Pillar width 57
3.3.7 Time variable multipath 59
3.4 Summary 60

4 Empirical modelling of site-specific errors 63
4.1 Undifferenced phase residuals 63
4.2 ESM method 64
4.2.1 Optimising model resolution 66
4.2.2 Grid resolution 66
4.2.3 Integration interval 69
4.3 Satellite specific-errors 70
4.4 Nadir approach 72
4.4.1 Distribution of observations 73
4.4.2 Post-fit residuals 77
4.4.3 Comparison of stacking and adjustment site models 80
4.5 Summary 80

5 Case studies 85
5.1 Goddard geophysical and astronomic observatory 85
5.1.1 Multipath characteristics of the Goddard stations 87
5.1.2 Kinematic processing results 87
5.1.3 Spectral analysis 90

5.2 Wettzell geodetic observatory, Germany . . . 94
5.2.1 Multipath characteristics . . . 94
5.2.2 Kinematic processing results . . . 97
5.3 Yarragadee geodetic observatory, Western Australia . . . 100
5.3.1 Multipath characteristics . . . 101
5.3.2 Kinematic processing results . . . 101
5.3.3 Spectral analysis . . . 103
5.4 Summary . . . 106

6 Global solutions **107**
6.1 Phase residuals . . . 108
6.1.1 Station stacked phase residuals . . . 108
6.1.2 Nadir stacked phase residuals . . . 110
6.2 Time series comparison . . . 113
6.2.1 Solution Spectra . . . 116
6.3 Orbit overlaps . . . 118
6.3.1 Periodicities in orbit overlaps . . . 120
6.3.2 Station and satellite clock estimates . . . 120
6.4 Comparison with GRACE estimates of elastic deformation . . . 123
6.5 Summary . . . 123

7 Conclusion **127**

A Appendix A **129**
A.1 Reference systems . . . 129
A.1.1 International Earth Rotation and Reference Systems Service . . . 129
A.1.2 International GNSS service . . . 129
A.1.3 Reference systems and realisations . . . 131

B Appendix B **133**
B.1 GPS observation modelling . . . 133
B.1.1 Ionosphere free linear combination . . . 134

List of Figures

1.1 Diagrams depicting phase variation of satellite and receiver antennas (adapted from [Görres *et al.*, 2006]) 5

1.2 Satellite Antenna beam width and path loss 11

2.1 Network Selected for 2012 DoY 100 25

2.2 Number of GPS stations processed, and ambiguity resolution success rate 26

2.3 An example of a Morlet CWT transform. The left axis is the Fourier period in years, the black contour lines enclose regions of great than 95% confidence for an estimated background noise level and the thick grey line demarcates the region of 'cone of influence' where edge effects become important. 33

3.1 Simulations showing the variation of the magnitude of multipath biases as a function of elevation angle, for monument heights of 0.10 and 1.50m, and for the GPS frequencies L1 (a), L2 (b) and the linear combination L3 (c), based on eq 1.7 37

3.2 Simulated L3 multipath bias and the modelled multipath bias obtained from the simulated least squares residuals for a monument height of 0.5m. The MPE error is calculated from the difference between the two (shown in red) 38

3.3 Multipath estimation error as a function of monument heights for surface roughness (S) values of 0.3, 0.5 and 0.7. This shows that materials with a higher S value reflect more of the input signal power, which will increase the MPE error. The MPE error peaks for a monument height of 0.17m 39

3.4 Correlation coefficient of the simulated multipath with a simplified troposphere zenith delay mapping function ($1/sin(e)$) and a simplified data weighting function ($1/sin(e)^2$), calculated for a range of monument heights 40

3.5 The impact of processing parameters on the propagation of multipath bias and resulting effect on the estimated parameters for different monument height 41
3.6 Impact of changing the elevation cut-off angle upon the propagation of a multipath bias into the estimated parameters of height, TZD, clock, and the effects upon MPE for monument heights of (a) h = 0.17 m and (b) h = 1.50 m. 42
3.7 The impact of the multipath bias upon estimated parameters when the frequency of positioning estimates is increased from once a day, to every epoch. 43
3.8 The influence of a stations latitude upon the MPE for two different monument height scenarios of 0.17 m and 1.5 m. At latitudes above $\pm 60^{\circ}$ (denoted by dashed vertical lines) there was a poleward increase in the MPE RMS for the low monument scenario. 44
3.9 The impact of antenna type on the propagation of multipath biases, shown over varying monument heights. 45
3.10 The effect of pillar width for a monument 1.5 m high, for two different values of surface roughness, (a) S = 0.3 and (b) S = 0.5. 49
3.11 The height time series obtained from a multipath simulation for monument heights of h = 0.17 m and h = 1.50 m over the period January 1st 2000 to December 31st 2013. The three best fitting noise models obtained from Hector program [Bos *et al.*, 2013] are overlaid. 50
3.12 The height time series obtained from the simulation of multipath for a monument height of h = 0.17 m, starting from January 1st 2000, to December 31st 2013. 51
3.13 The height time series obtained from a multipath simulation for a monument height of h = 0.17 m, with no clock estimation. 53
3.14 The height time series obtained from a multipath simulation for a monument height of h = 1.50 m 54
3.15 Antenna calibration comparison between GEO++ results and Geoscience Australia Results on L1, L2 and the Ionosphere free linear combination LC 55
3.16 Morlet CWT of the height bias time series from 2000 to 2014 from simulations of antennas at a range of latitudes varying from 0° to -70°, at a height of 0.17m 58
3.17 PSD and Morlet CWT of height time series using two different pillar widths of 0.3 and 0.6 m at the same monument height, h = 1.5 m, surface roughness S= 0.5. 59

4.1 Illustrative example showing the process to create an ESM (b) and publishing for re-processing (c). 65
4.2 (a): Multipath bias for a monument height of 2.00m sampled at 0.001° (black line) and 5° (red line). (b): Error in grid intervals of 5°,2°,1°,0.5°, and 0.1° for the simulated L3 Multipath bias for a range monument heights (0.01 to 2.0m) compared to a higher resolution of 0.001° 68
4.3 The number of stations which have an optimum grid resolution of 5°,2°, 1°, 0.5° and 0.1° based upon the grid spacing which produced the smallest MAE metric. 69
4.4 The computed mean absolute error as more phase residuals are accumulated with time for a block median ESM with a grid resolution of (a) 2° (b) 0.5°. 70
4.5 Relationship between satellite and receiver antenna phase centre variations.(Adapted from [Schmid and Rothacher, 2003]) 71
4.6 Change Δr of the phase centre offset interpreted as a change of $\delta\phi'(z')$ (nadir dependent PCV) of the phase pattern. 72
4.7 The calculated adjustment to the NADIR PCV model and distribution of observations with nadir angles for SVN G062. The results were obtained from a global network of 85 stations using the post-fit residuals for 2012 only, with a 10 mm constraint on the Satellite Nadir PCV. . . . 74
4.8 Comparison of estimates for nadir angle corrections obtained from five different global networks, using residuals stacked over 4 years from 2010 to 2013.The black dashed line is the mean solution for all of the networks, and the error bars represent 1 standard deviation from the mean. 75
4.9 Comparison of estimates for nadir angle corrections obtained from five different global networks consisting of 80 stations in each network, using residuals stacked over 4 years from 2010 to 2013. Network 6 is a larger network comprised of over 500 station phase residuals. 76
4.10 Estimates of Nadir PCV corrections without consistent satellite results, obtained from and PWL adjustment of phase residuals from 2010 to 2013. 78
4.11 Estimates of Nadir PCV corrections with significant individual satellite departures from the block mean, obtained from and PWL adjustment of phase residuals from 2010 to 2013. 79
4.12 Estimated Nadir PCV corrections for SVN56, obtained from and PWL adjustment of phase residuals from over 456 ground stations from 2010 to 2013. 81

4.13 Post-fit residuals for the IGS station COCO, using the nadir modelling approach. 82
4.14 Piecewise linear site models for COCO from and adjustment of phase residuals accumulated between 2010 to 2013 (a) without nadir PCV corrections applied, (b) with nadir PCV corrections applied, (c) difference between the two models. 83

5.1 GPS stations installed near the Goddard Observatory, (a) GODE, (b) GODS, and (c) GODN. Photos obtained from Fancher *et al.* [2012] . . . 86
5.2 GODS L3 azimuth and elevation phase residuals, note the prominent stripes to the east and south east. 87
5.3 GODE elevation only L3 phase residuals, (a) JPLA radome installed, and (b) after JPLA radome removed. There is a small change in the residuals above 85◦ in elevation, however the large elevation dependent bias remains. 88
5.4 PSD of the difference in height from GODE to GODN for (a) standard kinematic solution, and (b) with an ESM model applied. The application of the ESM has removed a significant portion of the high frequency noise. 91
5.5 Morlet CWT variogram of the height difference between GODE to GODN for (a) standard kinematic solution, and (b) kinematic solution with the ESM modelling applied. The application of the ESM has reduced the high frequency noise components. 92
5.6 PSD of the difference in height from GODS to GODN for (a) standard kinematic solution, and (b) with an ESM model applied. The application of the ESM has removed a significant portion of the high frequency noise. 93
5.7 The GPS stations installed at the Wettzell Observatory, WTZZ, WTZA, WTZR and WTZS. Photos obtained from http://www.igs.org, map obtained from [Schlüter *et al.*, 2005] (WTZS is not shown). 95
5.8 WTZA L3 residuals vs Azimuth and Elevations 96
5.9 Azimuth and Elevation L3 phase residual plots for (a) WTZZ and (b) WTZS 96
5.10 PSD of the difference in height from WTZA to WTZR for (a) standard kinematic solution, and (b) with an ESM model applied. The application of the ESM has removed a significant portion of the high frequency noise. 98

5.11 Morlet CWT variogram of the height difference between WTZZ to WTZS for (a) standard kinematic solution, and (b) kinematic solution with the ESM modelling applied. There is a significant change in spectral characteristics following a receiver firmware change at WTZZ near 2012.5. The application of the ESM has reduced the high frequency noise components. 99
5.12 The YAR2 GPS station installed at the Yarragadee Observatory (photo provided by Nicholas Dando). 100
5.13 YAR3 elevation dependent L3 phase residuals vs. elevation angle 101
5.14 YAR2 L3 elevation only phase residuals for (a) JPLA radome installed, and (b) after JPLA radome removed. There is a small change in the residuals above 80° in elevation, however the large elevation dependent bias remains. 102
5.15 PSD of the difference in height from YAR2 to YAR3 for (a) standard kinematic solution, and (b) with an ESM model applied. The application of the ESM has removed a significant portion of the high frequency noise. 104
5.16 Morlet CWT variogram of the height difference between YAR2 to YAR3 for (a) standard kinematic solution, and (b) kinematic solution with the ESM modelling applied. 105

6.1 Map showing the selected stations with over 1000 observations between the period of 2010 to 2013, and a horizontal random walk less than $0.5\text{m}^2/\text{yr}$ (a total of 183 stations). 108
6.2 Phase residual RMS for standard, ESM and nadir solutions. The ESM solution has significantly improved the phase RMS 109
6.3 Stacked phase residuals for the GPS station CEDU obtained from the standard, ESM and nadir solutions. A block median fit at resolution of 0.5° was used to calculate the RMS of the model. 109
6.4 The calculated adjustments to the Nadir PCV model obtained from the (a) standard, (b) ESM , and (c) nadir solutions 111
6.5 Comparison of Nadir Phase residual RMS for standard, ESM, and nadir solutions for each SVN. The dashed line indicates a cut-off RMS where the adjustments to the nadir PCVs may be considered significant. Adjustments from the standard solution which fall below this line should not have been applied. 112
6.6 Comparison of nadir adjustment models derived from the standard and ESM solutions. 112

6.7 Comparison of Nadir phase residuals stacked for the standard and nadir solution for SVN 23 . . . 113
6.8 Comparison of the median RMS of weekly height estimates, for all of the stations processed, for the standard solution (blue), the ESM (top - green), and nadir (bottom -green) solutions. . . . 115
6.9 Comparison of a Lomb periodogram stack of the stable stations, for the standard,ESM, and nadir solutions. The draconitic and harmonics are marked by vertical red solid lines. . . . 117
6.10 Overlap differences in Total position for the standard solution . . . 119
6.11 Mean RMS Orbit overlap error, broken down into radial, along and cross track components obtained from the standard, ESM, and nadir solutions . . . 119
6.12 Mean difference in the RMS between the standard solution and the nadir solution orbit overlap errors, for the radial component of satellite PRN29. The red-dashed line is the mean rms difference (0.007m), a positive difference indicates that the nadir solution orbits have a closer agreement . . . 119
6.13 PSD of Orbit overlaps for the different solutions . . . 121
6.14 The difference in daily mean of station clock rms, between the standard, ESM and nadir solutions . . . 122

List of Tables

2.1 Summary of multipath mitigation approaches 21
2.2 Processing parameters applied to global solution 27
2.3 Factors influencing the choice of wavelet are often dependent upon the type of analysis being carried out 30

3.1 Simulation of uncalibrated radomes. 46
3.2 Serial numbers of SCIGN radome before and after the change of material 47
3.3 Results from simulations of the effect of concentric radome made from materials with a different refractive index. An the influence processing parameters have upon the results. 47
3.4 Time correlation parameters for different simulated time series. Where d is the slope of the spectra, multiply by 2 to get the equivalent spectral index k. 56

4.1 Official satellite block designations [Navstar, 2004], space vehicle number (SVNs) and manufacturers 77
4.2 IGS designations for the Block IIR satellites and the corresponding SVNs [Dorsey *et al.*, 2006] 77

5.1 GPS stations located at the Goddard Observatory. 86
5.2 Kinematic Processing results for GODE, GODS, GODN, and there differences with terrestrial survey results obtained from NGSWASH1206A.SNX 89
5.3 GPS stations located at the Wettzell Observatory. 94
5.4 Kinematic L3 processing results for WTZZ, WTZA, WTZS, WTZR, and terrestrial survey results. 97
5.5 GPS stations located at the Yarragadee Observatory. 100
5.6 Kinematic Processing results for YAR2, YAR3, and terrestrial survey height differences 103

6.1 Median Random walk (m^2/yr), minimum number of observations = 1000, nsigma = 4 , maxsigma 0.02 114
6.2 mean height rate uncertainty derived from a power law + white noise model 116

6.3 RMS of differenced time series of GPS Height - GRACE height elastic deformation, for the standard, ESM, and nadir solutions. 124

B.1 The advantages gained from the ionosphere-free linear combination is a significant decrease in ionosphere noise, however this comes at the expense of an increased measurement noise. 134

Chapter 1

Introduction

Accurate reference frames are fundamentally important for Earth science studies, for satellite navigation, for applications relying on geo-spatial information, and increasingly for commercial applications. For more than two decades GPS has been used to not only help determine reference frames, but to study temporal changes in the Earth's crust, atmosphere and oceans. Over this time, analysis and modelling techniques have been continuously refined and improved. Such as the improvements in GPS analysis obtained through improved modelling of the troposphere delays using time-varying mapping functions [Boehm *et al.*, 2006a,b], a priori modelling of hydrostatic delays [Tregoning and Herring, 2006], and enhanced models of the receivers [Wübbena *et al.*, 1996] and satellite antennas [Schmid *et al.*, 2007].

Despite the numerous advances in modelling GPS error sources, there has been very little agreement on how to address site-specific errors in GPS processing. A major component of a site-specific errors are due multipath, caused by reflections of the incoming GPS signal, other sources include errors in the antenna model being applied, or changes to the antenna characteristics due to the near-field effects introduced by the station antenna mount. It is now well known that multipath errors can alias into the GPS time series producing time-correlated errors [King and Watson, 2010]. This results in a GPS time series which will have unmodelled biases that can affect the interpretation of geophysical signals, particularly those which occur near annual and draconitic frequencies and there harmonics. This is potentially a limiting factor in using GPS time series to derive reference frame parameters and the investigation of geophysical phenomena. The introduction of additional time correlated noise degrades the certainty of the velocity estimates. This then degrades the ability to detect offsets, and in addition potentially introduces systematic biases into the derived reference frame.

The main objective of this thesis is to investigate the impact of different site-specific errors upon the coordinate time-series, and then develop and implement a procedure to mitigate for these errors. To achieve this, it is important that other

sources of error are not inadvertently included, or other geophysical effects are not 'absorbed' into the site-specific model. In order to be applicable to reference frame determination the technique developed needs to be suitable for historic data sets, as well as being applicable to future data sets.

1.1 Thesis outline

1. **Chapter One: 'Introduction'** - The remainder of this chapter will provide background information relevant to proceeding chapters and an overview of site-specific errors, which can affect GPS time series.
2. **Chapter Two: 'Background, theoretical basis and methodology'** - Gives an overview of previous multipath mitigation techniques, as well as an overview of previous work similar to that presented in this thesis. We then present a theoretical background to utilising least squares residuals as a way of capturing unmodelled site-specific errors.
3. **Chapter Three: 'Impact of site-specific effects'** - Focuses on the theoretical impact of the propagation of multipath errors under different site conditions. We investigate both the short-term impact of multipath on positioning, and then the long-term impact on GPS station position time series. We then assess the plausibility of using least squares residuals to model the simulated multipath error.
4. **Chapter Four: 'Empirical modelling of site-specific errors'** - Presents two different methodologies to empirically derive site-specific models. The first technique uses a stacking and gridding of the residuals to obtain a model for each station. The second technique applies a two step adjustment procedure, first to account for satellite specific errors, and then creates the site-specific model accounting for satellite specific effects.
5. **Chapter Five: 'Case studies'** - Details the application of the ESM technique to kinematic processing for short baselines at three different case study locations located around the world, where a ground truth from a terrestrial survey is available to provide a comparison of the position solutions.
6. **Chapter Six: 'Global solution'** - Presents the results from applying the two ESM techniques to a global solution. We investigate the impact the modelling techniques had upon IGS products, and the positioning time series as compared to the IGS repro2 solution computed by ANU/MIT.

7. **Chapter Seven: 'Conclusion'** - We provide a summation of our findings from this thesis, provide some recommendations in the application of ESM the modelling technique developed in this thesis, and then we highlight future areas of research into this topic.

1.2 Site-specific error sources

Site-specific errors can be divided into three categories. The first categories of errors are caused by variations in the site characteristics, which intermittently affect GPS measurements such as precipitation, atmospheric pressure loading and atmospheric gradients. The second category are concerned with effect associated with the long-term stability of a site, such as the location of the site, ground type, and construction of the monument. These effects may seriously affect the reference frame, and geodynamic projects.

Finally errors caused by the receiver, antenna and radome make up the final category. It is this category of site-specific biases that will be focused on in this thesis. These are errors derived from the receiver, antenna and radome, which can introduce biases into the position solution. These biases should remain constant, unless the equipment at the station has been changed, the bias in the position solution will remain approximately constant. One should also consider the scenario of equipment degradation, antenna performance decay, and tracking loop failures in receivers [e.g. Park *et al.*, 2004; Hill *et al.*, 2009]. However, a substantive change of the satellite elevation angles will change the way the bias propagates in the position solution. This is most noticeable as a bias introduced in the vertical component of the position, and when the analysis of the precipitable water vapour is carried out. As will be detailed later these errors caused by the receiver, antenna and radome can seriously affect the interpretation of the GPS measurements.

1.2.1 Antennas characteristics

Different types of antennas have distinctly different characteristics that can influence how site-specific errors are propagated into the GPS observations. In an ideal case, all components of the GNSS signals are received at a single point. For phase measurements, this point is known as the antenna phase centre (APC). The APC is a virtual point, usually in or above the antenna, which cannot be used to link the measurement with the measurement point on the ground. For this reason, an antenna reference point (ARP) is necessary to refer the virtual APC to the physical mounting of the antenna. By convention, the ARP of receiver antenna is the crossing point of

the antenna centre line and the bottom side of the antenna. For satellite antennas the convention is to use the satellite centre of mass (COM) as the ARP, as the offset between the antenna mounting point and the satellite's COM are not commonly known [Rothacher *et al.*, 1996]. For both terrestrial and satellite antennas, the relationship between the APC and the ARP is described by the phase centre offsets (PCOs) (see Figure 1.1).

Another factor that can introduce error is the variation in the sensitivity of the antenna. Antennas are not equally sensitive to signals, regardless of their direction, frequency and polarisation. It has been well established that phase centre patterns differ between antenna models and manufacturers. Research has also found that the addition of a radome or the choice of antenna mount can significantly alter the a priori phase centre patterns. It is particularly important to know the phase centre pattern for GPS applications requiring high position accuracy, especially when there is a range of antenna types in use. In such cases it is necessary to know how the phase centre varies in both elevation and azimuth in the antenna reference frame, and incorporate these models into analysis software. Consequently, the PCV is defined as being different from the optimal spherical wavefront. The total phase centre correction (PCC), the contribution from the PCO and PCV, is determined through an antenna calibration technique.

1.2.2 Antenna calibration

Before 2006 the PCC for receiving antennas was determined by a relative calibration technique [Rothacher *et al.*, 1996; Mader, 1999]. A relative antenna calibration makes use of a reference antenna, typically this was the AOADM/_T (Allen Osborne Associates Dorne Margolin T) and setting the PCVs, for the reference antenna, to be zero. This assumption, together with various other limitations of this technique, lead to systematic errors [Schmid *et al.*, 2005].

Today there are essentially three different approaches to absolute antenna calibration in practise: two independent field techniques [Wübbena *et al.*, 1996; Bilich and Mader, 2010], and an anechoic chamber [Schulper and Clark, 2001; Zeimetz and Kuhlmann, 2008]. All three methods provide reasonable results. Since the introduction of absolute antenna calibrations [Schmid *et al.*, 2005] it has also been necessary to also account for satellite antennas. Schmid and Rothacher [2003] demonstrated a method for the estimation of elevation-dependent satellite antenna PCVs.

The antenna working group of the IGS provides a consistent set of antenna calibrations for satellite antenna, as well as for all common geodetic receiver antenna. The calibration values of the receiver antenna are type mean values from an absolute

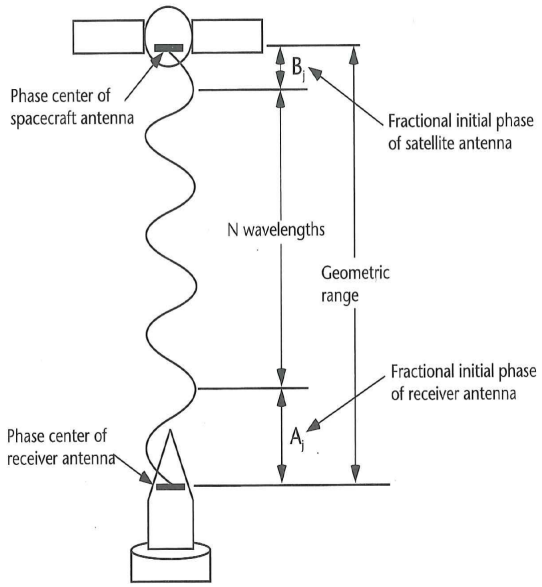

(a) Relationship between the geometric range and the APC of the satellite and receiver antenna

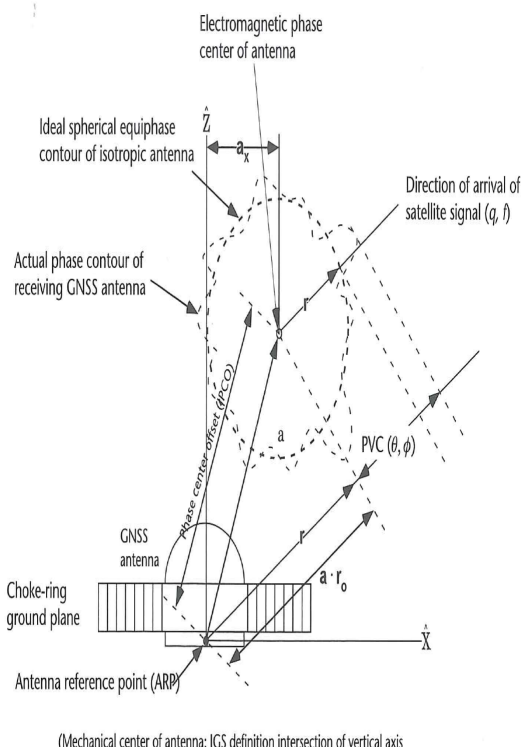

(b) Relationship between a receiver antenna PCO and PCV to obtain a PCC

Figure 1.1: Diagrams depicting phase variation of satellite and receiver antennas (adapted from [Görres *et al.*, 2006])

field calibration [Wübbena *et al.*, 1996], whereas the satellite antenna calibrations are the result of a global least squares estimation using the receiver antenna calibration tables. An overview of the topic of antenna calibration can be found in Schmid *et al.* [2007].

1.2.3 Antenna calibration errors

The use of the mean assume that the PCCs of each antenna type can be represented with sufficient accuracy for any manufactured antenna of that type. In order for this to be valid, the antennas must have little variation in their antenna characteristics throughout their lifespan.

The bureau for the European reference frame has implemented a policy of using the original individual antenna calibrations, which are linked to a specific antenna/radome type and antenna serial number. Baire *et al.* [2013] examined the effect of applying a type mean calibration instead of an individual antenna calibration model, as well as comparing the effect of using individual antenna calibrations obtained from different calibration facilities. The University of Bonn performs calibration in an anechoic chamber, while GEO++ developed a robotic outdoor calibration system. They also obtained calibrations from the University of Hannover, and the state survey authorities of Berlin, which both use the same robotic calibration system obtained from GEO++. They found large differences for the LEIAR25.R3/LEIT antenna type with position offsets of -1cm in height for SOFI and VALE, and +8mm for HOE2. Smaller but statistically significant offsets were found for other antenna types. Earlier, Schmid *et al.* [2005] found that PCC of individual antennas can easily differ by up to 1cm from the type mean. Using individual calibration instead of type mean calibrations can thus have a significant impact on the estimated station positions, and caution is necessary when comparing solutions computed from type means and individual calibrations.

While the individual antenna calibrations will be more representative than a type mean calibration, they will still be subject to the difference in near-field environments between where the antenna has been calibrated, and where the antennas has been deployed for observations. For instance when calibration results are compared between different institutions systematic effects can be seen especially when using different methodologies i.e. anechoic chamber compared to a robot calibration. There are strong indications that the dominant error for both chamber and robot calibrations is near field multipath. Zeimetz and Kuhlmann [2008] found differences of up to 2cm on L2 when comparing results obtained from an anechoic chamber, and robotic calibrations. Robot measurements reveal up to 5mm [Dilßsner *et al.*, 2008] change in

GPS L2 PCCs for different antenna mounts.

Antenna-pillar interaction

The antenna and the pillar mount interact with each other by electromagnetic coupling of the antenna and its nearby environment. The total electromagnetic field of the antenna, which radiates and interacts with nearby conducting structures, can be expressed as a superposition of the transmitted field and the scattered fields (reflected and refracted by nearby structures). The significance of the scattered field depends on the degree of electromagnetic coupling between the antenna and the scattering object, the size and reflectivity of the scattering object and its distance from the antenna. The signal scattering introduced by the pillar affects both the amplitude and phase of the received GPS signal, which varies according to the antenna and pillar properties of each site.

Scattering from structures in the vicinity of the antenna effectively changes the antenna phase pattern, and affects the precision of the carrier phase measurements. Elòsegui *et al.* [1995] and Jaldehag *et al.* [1996] showed that estimates of the vertical component of baselines formed between sites using identical antennas were dependent on the minimum elevation angle of the data processed. Both studies found that the elevation-angle-dependent systematic effect was associated with non-identical pillar arrangements, causing differential phase errors. Therefore, even when an antenna has a perfect calibration, the antenna phase pattern will change when it is attached to a different structure. Modelling of the scattering effect, or the complete phase response of the antenna system (including the pillar) is an important issue for future improvements to rigorously account for antenna effects.

1.2.4 Radomes

A radome is a cover or structure placed over an antenna that protects the antenna from its physical environment. Ideally, the radome is radio frequency (RF) transparent to avoid degrading the electrical performance of the enclosed antenna in any way. Radomes are widely used within the geodetic community to protect GPS antennas at permanent sites from snow, debris accumulation and vandalism. They are generally designed to have a uniform thickness to minimise the impact on the electrical phase centre of the antenna. Kozakoff [2010] found that the antenna performance can be reduced by a range of radome effects which alter the antenna's original designed characteristics, such as:

- An introduction of a boresight error (BSE) by the radome

- An introduction of a boresight error slope by the radome,
- A change in antenna side lobe levels,
- An increased depolarisation of the folding of energy from one polarisation sense to another,
- An insertion loss due to the presence of the radome.

Adding a radome to an antenna will cause the angle of the incoming signal to bend away from its original angle of arrival, this is known as the boresight error. This stems primarily from distortions of the electromagnetic wave front as it propagates through a dielectric radome wall. The degree of BSE varies depending on antenna orientation, the observed frequency and polarisation of the incoming signal. The increase in antenna side-lobes occurs because due to distortion and wall transmission effects as a wave front propagates through a radome wall.

The radome can also cause depolarisation or a folding of energy from the primary antenna polarisation to the other sense. For instance, an incoming right-hand circularly polarised (RHCP) signal will be partially converted into a left-hand circularly polarised (LHCP) signal before incidence on the antenna. This is caused by the radome wall curvature, and the difference in complex transmission coefficient between orthogonal polarised vectors.

The radome wall also causes a reduction in signal strength, called insertion loss. As the electromagnetic wave propagates through the radome wall part of the loss occurs as a reflection at the air-radome wall interface. The remainder of the loss occurs from dissipation within the dielectric layers.

There have been many empirically studies on the impact of radomes on GPS time series. Schmidt *et al.* [2003] found that the SCIGN radome altered the vertical coordinates by 1.5cm when used with a Dorne-Margolin(DM)/JPL choke ring antenna. Schmidt *et al.* [2003] suggested that the coordinate change was induced by a misalignment of the radome centre of curvature with the mean L1/L2 electrical phase centre. In fact, that radome was designed to have a radius of curvature centred at the physical centre of the DM element, which was offset from the electrical phase centre by 3.5cm difference. Braun [2007] was unable to find any significant impact on either stations coordinate or troposphere parameter estimates when a local baseline test was conducted with, and without the SCIT radome installed.

The observation that both the apparent height and the tropospheric delay estimates are affected by the presence of the SCIGN dome can be reconciled by considering the effect of a hemispherical dome on an incident plane wave. Consider a

plane wave incident from zenith = 0°. The plane wave will develop a curved wave front inside the dome, where the delay is a function of the refraction index r_m, and the obliquity (or deviation) of the tangent to the dome with the incident plane wave. Inevitably unmodelled radomes will yield a lowering of the height estimates compared to antenna set up without a radome. The extra distance of travel through the radome material is given by:

$$h = \frac{h_0}{cos(Z)} \tag{1.1}$$

where h_0 is the thickness of the radome wall, and Z is the zenith angle. The delay introduced by the dome material compared to travel through free air can be estimated from:

$$\Delta t = \frac{h}{c_m} - \frac{h}{c} = \frac{h(c - c_m)}{cc_m} \tag{1.2}$$

Substituting $c_m = \frac{c}{r_m}$ gives:

$$\Delta t = \frac{h(r_m - 1)}{c} \tag{1.3}$$

Substituting for h from eq. 1.1gives the expression:

$$c.\Delta t = \frac{h_0(r_m - 1)}{cos(Z)} \tag{1.4}$$

Expression 1.4 gives the extra distance delay along the wavefront as one moves away from the axis of symmetry. This distance delay has a $1/cos(Z)$ dependence. If the phase centre of the antenna is not coincident with the centre of curvature of the dome, then the delay due to the dome will be mapped into the troposphere delay.
For the SCIGN dome, $h_0 = 3.175mm$ and r_m 3, thus giving the relation:

$$c.\Delta t \ \frac{6.35}{cos(Z)} mm \tag{1.5}$$

Expression 1.5 has the form $\Delta H = \frac{\Delta\rho}{cos(Z_{max})}$, which to a first order approximation, gives a station's height bias, ΔH as a function of relative troposphere zenith delay error, $\Delta\rho$, and the maximum zenith angle of observation, Z_{max}.Using a value of 4.2 [Santerre, 1991] of 4.2 for Z_{max} of 80° for a mid-latitude site, the bias in computed height is predicted to be approximately 2.5cm.

As long as the set up is not changed, the radome should not introduce a discontinuity into the time series, however the position estimate will not refer to the physical antenna reference point, and therefore the solution will be biased. The effects can be very large, especially in the height component up to several cm, the magnitude of the effect will depend not only on the radome type but also on the elevation cut-off

angle used in the processing [e.g. Kaniuth and Huber, 2003].

1.2.5 Satellite antennas

The L-band antenna onboard the GPS satellite is designed to radiate the composite L-band signals to the users on, and near Earth. It provides a nearly constant signal level to the user receivers over the whole Earth's surface with circular polarization at L_1, L_2, and L_3 frequencies (see Appendix B for a summary of GPS signals and the ionosphere-free linear combination).

The L-band antenna is broadband, fixed beam antenna, where the GPS satellites has a three axis attitude stabilisation system that keeps the L-band antenna pointed towards the centre of the earth. From the GPS satellite's altitude, the view angle from edge-to-edge of the earth is about 27.7°. The total pointing error of the satellite is specified to be less than $\pm 0.015°$, with 99% probability. So a fixed-beam antenna with adequate gain over 28° is used by GPS satellites.

The goal of the antenna is to illuminate the Earth's surface in view of the satellite with almost uniform signal strength. The path loss of the signal is a function of the distance from the antenna phase centre to the centre of the earth. The path loss is at a minimum when the satellite is directly overhead, and is at a maximum at the edge of Earth's coverage (Satellite is at the horizon). The difference in path length between these two extremes is approximately 500km, which results in a variation in signal strength of 2.1dB.

The ideal pattern required to illuminate the surface of the earth is shown in Fig 1.2. This is symmetric about the axis from the satellite to the centre of the Earth. Beyond the 28° view angle, the antenna will radiate near-zero radio frequency energy. Typically a practical antenna with a smooth antenna pattern is designed so that the variation in signal strength over the 28° view angle is minimised, and the total radiated energy over the 28° angle is maximised.

However there is now an increasing use of the GPS signal outside of the original designed envelope for the purposes of orbit determination of LEO satellites as well as in occultation studies. There is work carried out by this community to determine the satellite PCV beyond the designed GPS satellite main-beam, and into the side lobe.

As each GPS satellite block type has been manufactured with different specifications, satellite antenna characteristics have changed with time. Rockwell performed the initial concept and design of the antenna array for Block I, II, and IIA satellites. The Block I antenna has a circular peak antenna gain (in the plane perpendicular to the central axis), with a dip in antenna gain at the antenna boresight. The peak is

(a) Path Loss

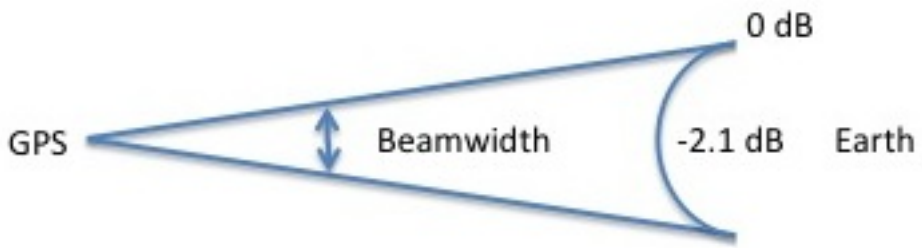

(b) Ideal beam width

Figure 1.2: Satellite Antenna beam width and path loss

located approximately 10° from the boresight. This antenna is a phased array design. It is comprised of 12 helical elements, arranged in two concentric circles on the Earth facing satellite panel. The inner circle is composed of four equally spaced elements, and the outer circle contains eight elements also equally spaced. Each element is a monofilar axial mode helix. The helix element design provides a wide bandwidth and circular polarization with minimal element-to-element interaction. The relative radi of the inner ring and outer ring control the angular location of the near-circular antenna peak. The elements in the inner ring are fed in-phase with 90% of total power, and the outer ring elements are fed 180° out of phase with 10% of total power. The depth of the dimple with respect to the peak is controlled by the ratio of power between the inner and outer ring elements.

In Block II/IIA satellites the cylindrical ground plane for each element was changed to a conical design. This significantly reduced the side and backlobes radiated by the antenna, which improved the antenna's efficiency and is less susceptible from adjacent and forward bulkhead obstructions. Several changes were made in the Block IIR design. The ratio of inner and outer radii and radio frequency power feed ratio were changed. In Block IIR, the 180° relative phase between the inner and outer elements is achieved with a 90° electrical phase shift from the strip-line beam-forming network, and a 90° mechanical rotation of the outer elements relative to the inner elements.

1.3 Multipath errors

A large component of GPS site-specific error is caused by unmodelled multipath effects [Elòsegui *et al.*, 1995; Hatanaka *et al.*, 2001; King and Watson, 2010]. Errors due to multipath have a sidereal periodicity [Choi *et al.*, 2004; Agnew and Larson, 2007] and can propagate into long term position time series with significant power at the GPS draconitic year (∼351.4 days), and its harmonics [Ray *et al.*, 2008]. Especially when correlated with other parameters of interest, unmodelled error sources can have a detrimental effect of introducing spurious artefacts into parameter time series.

Multipath is a major source of cm-level positioning error caused by interference of the original signal with diffused and specular reflected signals from the environment at the receiving antenna. Phase multipath error can be as high as a quarter of a wavelength, i.e. 4.8cm for the L1 carrier, and 6.1cm for the L2 carrier [e.g. Hofmann-Wellenhof *et al.*, 2012]. Furthermore, multipath phase error increases with the use of phase linear combinations, reaching for example a maximum multipath error of 21.7cm for the ionosphere free combination. The site-specific multipath errors are

mainly charcaterized by the distance the reflecting object is from the antenna. Objects which are further away from the antenna exhibit short periodic variations with the change in elevation angle, whereas objects near the antenna have a non-zero mean and exhibit long periodic characteristics [Wübbena *et al.*, 2000] The site-specific multipath effects can be subdivided into a near-field and a far-field component. Far-field effects show short periodic behaviour. In contrast, near-field effects have non-zero mean and exhibit long periodic characteristics (up to several hours [Wübbena *et al.*, 2006]).

1.3.1 Theory

To further understand multipath, it is necessary to understand the electromagnetic properties of the GPS signal, and the changes the signal undergoes during reflection and refraction. The electric and magnetic field of an electromagnetic wave are interdependent while propagating through space. A plane travelling wave wherein the electric field (E), and the magnetic field (H) are perpendicular to each other everywhere. Both fields propagate in a direction perpendicular to their field vectors; such a wave is called a Transverse Electromagnetic wave (TEM).

The polarisation of a propagating wave is decided by the time-varying nature of the electric field component. If the direction of the field remains unchanged with time, then it is said to be linearly polarised wave. If the electric fields rotate as a function of time, then the tip of the vector describes the polarisation to be either elliptical or circular depending on the shape of the curve traced by the tip. The elliptical polarization is the generalised form, which in the two extreme cases is either linear or circular. If the direction of rotation of the electric vector is clockwise, as viewed from the origin towards the propagation, then it is right-hand polarised.

GPS is a right-hand circular polarised TEM wave. Satellite signals are generally polarised, due to an effect known as Faraday rotation, which causes linearly polarised signals travelling through the ionosphere to change polarisation. The magnitude of the rotational change in polarisation will fluctuate, making it difficult for the ground based antenna to match the right polarisation of the propagating signal.

The reflection and scattering of the signal from a surface has two components (i) the specular, and (ii) the diffuse component. Specular reflection occurs when the electromagnetic wave is reflected by a smooth surface. The reflected wave is the summation of all points contained within the Fresnel zone. The resultant wave has very little fluctuation of phase and amplitude; if on the other hand if the surface is rough, then the reflected signals is diffuse.

Rayleigh quantifies the roughness of a surface through a simple expression, known

as the Rayleigh criterion. According to the criterion a surface is smooth if:

$$\delta h < \frac{\lambda}{8 \sin \theta} \tag{1.6}$$

1.3.2 Multipath model

The multipath model added as a site-specific error, in the simulations detailed later, was adapted from the model used by King and Watson [2010]. We have used derived values for the direct gain(g_d) for Right Hand Circular Polarised (RHCP) signals and the reflected gain rate (g_r) for Left Hand Circular Polarised (LHCP) signals. We adopted published values for the Leica AT504 choke ring antenna[Bedford *et al.*, 2009], commonly deployed in geodetic networks, and of a similar design to the most common geodetic antenna in the IGS network, the AOAD/M_T antenna. The direct gain measurements were $g_{dL1} = 1.1044$, $g_{dL2} = 1.0931$, and for the reflected gain values were linearly interpolated from a figure of Bedford *et al.* [2009].

The multipath effect $\delta\phi_L$ was modelled by:

$$\delta\phi_L = \frac{\lambda}{2\pi}\left(\tan^{-1}\frac{a\sin[4\pi\frac{H}{\lambda}\sin\varepsilon]}{g_d + a\cos[4\pi\frac{H}{\lambda}\sin\varepsilon]}\right) \tag{1.7}$$

where,

$$g_d = \cos(z/G_{RHCP}) \tag{1.8}$$

$$a = Sg_rR_a \tag{1.9}$$

$$g_r = \cos((pi/2)/G_{LHCP})(1 - sin(\varepsilon)) \tag{1.10}$$

$$R_a = \left[\frac{n_1\cos z - \sqrt{n_2^2 - (n_1\sin z)^2}}{n_1\cos z + \sqrt{n_2^2 - (n_1\sin z)^2}}\right] \tag{1.11}$$

Where λ is the carrier phase wavelength for the L1 or L2 carrier phase signal respectively. The antenna gain pattern consists of the direct (g_d) and reflected (g_r) gain, a is the amplitude of the reflected signal for a given surface roughness (S). R_a is the Fresnel equation for an electric field perpendicular to the plane of incidence and depends on refractive indices n_1 and n_2, with $n_1 = 1$ for air, and n_2 appropriate for the reflecting medium. We adopted the same values that were used by King and Watson [2010] for S = 0.3, and $n_2 = 2$, appropriate for a smooth concrete surface surrounding the antenna.

The main limitations of the multipath model described here is the assumption of azimuthal symmetry, the time-constant parameters, and the assumption of a homogeneous planar reflector. Later in this thesis we will apply this multipath model to simulate the impact multipath can have upon positioning results, and then upon GPS time series.

1.4 Summary

This thesis is primarily concerned with site-specific errors attributed to errors in antenna models, and those obtained from multipath. These errors are expected to be consistent throughout the time-series, that is if the instrumentation and monumentation are unchanged. The nature of how these errors propagate into position time series, and other estimates is complex, and will be investigated in a subsequent chapter.

In the remaining chapters we will introduce the methodology used to mitigate for these error sources, and assess how these errors sources can bias estimates. We then investigate the methodology's effectiveness in modelling these error sources with short baseline, as well as in global solutions. We have excluded GPS observation modelling from the introduction of this thesis and we refer the reader to the Appendices for further background information.

Chapter 2

Background, theoretical basis and methodology

A large component of GPS site-specific error is caused by unmodelled multipath effects [e.g. Elòsegui *et al.*, 1995; Hatanaka *et al.*, 2001; King and Watson, 2010]. A multitude of techniques have been developed to try to address the problem of modelling and mitigating multipath effects. Despite this, to date, there is no accepted technique routinely applied in the processing of long-term GPS time-series. In this chapter we give an overview of some of the techniques, which have been developed to mitigate the effects of multipath and site specific errors in GPS observations. We then introduce the techniques that we have developed to address site-specific effects at the GPS observational level. We then detail the different processing methodologies used to test the modelling, and assess the effectiveness of the techniques developed in this thesis.

2.1 Related work

A ray-tracing approach was developed by Lau and Cross [2007] to model and remove the errors from multipath reflections, taking into account complex ray paths and diffraction. This study used physical models based on the Geometric Theory of Diffraction (GTD), which is, in effect an extension of geometrical optics. Byun *et al.* [2002] pointed out that the use of a simulator based on GTD, is only valid for wavelengths which are small in comparison to the dimensions of the interacting objects, and will fail to account for the scattering from small objects. The presence of an object in the near-field of an antenna can induce currents which alter the antenna's characteristics and are not addressed by optical theory [e.g. Elòsegui *et al.*, 1995; Byun *et al.*, 2002]. Despite these limitations, the ray-tracing approach could account for a significant portion of multipath effects, if accurate information is available about

the location as well as the microwave reflecting characteristics of all nearby objects. Unfortunately this is rarely the case, and the local area is rarely invariant in time, making it difficult to accurately apply this technique over long time periods or to large networks.

One promising technique uses the underutilized Signal to Noise Ratio (SNR) observations to map and estimate the multipath environment [Axelrad *et al.*, 1994]. The technique has been demonstrated to isolate and remove multipath error sources [e.g. Prüllage, 2013; Bilich and Larson, 2007; Rost and Wanninger, 2010; Benton and Mitchell, 2011]. However this technique is not suitable for correcting long-term historic data sets due to inconsistent measures of SNR from different GPS receivers, which in some cases are too coarse to produce a sufficiently accurate correction.

An approach developed by Wübbena *et al.* [2006] and later refined by Dilßsner *et al.* [2008] involves calibrating as much of the monumentation with the antenna, during the estimation of the antenna phase variation. This may be a promising approach for dealing with the near-field effects, especially if the robotic calibration system utilised can handle heavier payloads, than the current limitation of 15-20kg. However this technique does not address site-specific errors obtained from reflections outside the immediate vicinity of the antenna.

Wübbena and Schmitz [2011] overcomes far-field multipath effects by applying an in-situ calibration technique that uses a local network of temporary stations. This requires the placement of temporary stations, each with their antenna and mounts calibrated, around an existing station in a low far-field and near-field multipath environment. This technique is very promising, but like the ray tracing approach, it is not applicable to historic data sets where the equipment or environment of sites has changed.

A number of multipath mitigation techniques attempt to take advantage of the sidereal periodicity of GPS satellite orbits [e.g. Bock *et al.*, 2000] to predict and correct the multipath error. Enhancements to this technique that factor in variation of the satellite orbit period [e.g. Choi *et al.*, 2004; Larson *et al.*, 2007; Ragheb *et al.*, 2007]. Choi [2007] found a modified sidereal filter to be effective for high frequency observations (1Hz) where multipath signals which have a period of 30-300s. However when observations with a sampling of 30s were used, the technique was highly sensitive to an incorrect repeat period, which increased the likelihood of the multipath error becoming out of phase with the filter, resulting in an amplification of the error. The concept behind this technique is somewhat analogous to the one we present, although there are significant differences in the way the correction is obtained and implemented in the re-processed solution.

Wanninger and May [2001] developed a carrier phase multipath calibration algo-

rithm by detecting multipath effects in double difference carrier phase residuals. A number of assumptions were made, the first that the multipath effects would have a period which ranged between 10 to 45 minutes (due to the distance between the reflector and the antenna), and that all the major multipath effects would occur below 50° elevation. By correlating different combinations of double difference residuals, observations, which were suspected, of having multipath effects were isolated, and then these effects were estimated. The results were then stored in a rectangular grid of resolution 2° (elevation) and 10° (azimuth). Wanninger and May [2001] found that the variability of carrier phase multipath over one year revealed that large variations could be observed on days with snow cover, but no variability could be attributed to rainfall. The technique required a density of reference station of approximately 50km to produce reliable results. Wu and Hsieh [2010] developed a technique based on the statistical analysis of carrier-phase residuals to obtain a correction model, which is correlated with preceding observations. They found that 6 days of data could be used to remove multipath error from current and future data. They applied the technique to a short-baseline of 13.5m and a longer baseline of 23.1km, reporting an improvement of 40% in height determination. However they have not applied the technique to a longer data set, and it remains unclear how reliable the technique is for long-term GPS analysis.

The approach we investigated used stacks of undifferenced carrier phase residuals to generate a site-specific correction map, referred to throughout this thesis as an Empirical Site Model (ESM). This technique was first presented by Hurst and Bar Server [1998], who reported 'an order of magnitude reduction in the sensitivity of the station's final position solution to the elevation cut off angle', a reduction in the number of phase observations rejected, and a reduction in the post-fit phase residual RMS. Iwabuchi *et al.* [2004] showed that ESMs derived from phase residuals processed in a double difference network produced a similar results to the undifferenced approach. This confirms that application of the transformation of double difference phase residuals to undifferenced phase residuals [Alber *et al.*, 2000]. Choi [2007] investigated the use of residual stacking, among other site-specific mitigation techniques to improve the analysis of post-seismic analysis after the 2003 Tokachi-Oki earthquake. Choi [2007] used only 3 days of data to obtain an ESM, applying different resolutions in azimuth and elevation of 1°, 3° and 5°. They found that even a 1° resolution was too coarse to recover multipath errors below 45° in elevation (for high monuments). In recent work, mention is made by Haines *et al.* [2013] of an empirical technique to enhance the IGS antenna models used to monitor the vertical sea floor motion at Platform Harvest. The authors speculated that the technique mitigates the effect of multipath, however they provide limited information about the ESM

methodology and its effectiveness. Desai *et al.* [2013] used the ESM model approach to verify the suitability of two new GNSS stations to be part of a core reference frame network. They also reported a reduction in the variance of position estimates when the ESM was applied to the solution. Fuhrmann *et al.* [2014] developed a technique for generating multipath correction maps from single difference residuals obtained from continuously operating GPS stations. They focus their technique on a screening of the phase residuals through a series of statistical tests, and then base the correction grid on an analogous approach as an equal area grid. The comparison of their approach compared to a high-resolution fixed grid approach (0.5° x 0.5°) only saw a minor improvement in single difference residuals.

As multipath effects are site-specific, the analytical modelling is difficult. In contrast, empirical methods such as stacking enable a flexible multipath characterisation that captures the site-specific properties. Using a stacking approach should enable the multipath model to be independent of satellite-based system (the approach is not orbit dependent), is capable of detecting both far-field and near-field multipath. An advantage of the ESM approach is that historical data can be used to produce a site model of a particular station, which can be made available in a common format (e.g. a modified ANTEX file) for use by others. Additionally, the ESM approach can also correct for antenna and radome mis-modelling errors which may not be possible from other conventional calibration techniques. This makes it an attractive technique for application to long-term time series analysis.

No attention in the literature has been given to the theoretical basis, optimum design and efficacy of the ESM technique. In this thesis we provide a theoretical basis to assess in which conditions an ESM should be used to model site-specific errors. We also present a series of simulations that show the conditions under which the ESM approach is most effective, and also those situations where the technique may fail.

2.2 Theoretical basis

The GPS processing used in this thesis utilises a least squares (LS) estimation technique. In this section we give an overview of the theoretical basis for utilising the undifferenced carrier phase residuals obtained from the least squares estimation process to create a model of unestimated site-specific errors.

The starting point of LS is an over-determined system of equations. Over-determined means that the number of observations (m) is greater than is unknown parameters (n). Furthermore, the LS approach assumes the measurement to be observations (b) of a phenomenon, describable by a linear function. Giving A as the design matrix (m

Table 2.1: Summary of multipath mitigation approaches

Technique	References
Ray tracing	Lau and Cross [2007]
SNR-based	Axelrad *et al.* [1994], Bilich and Larson [2007]
Near-field calibration	Wübbena *et al.* [2006], Dilßsner *et al.* [2008]
In-situ calibration	Wanninger and May [2001], Park *et al.* [2004] Wübbena and Schmitz [2011]
Sidereal -filtering	Agnew and Larson [2007], Ragheb *et al.* [2007]
Residual based	Hurst and Bar Server [1998], Iwabuchi *et al.* [2004], Alber *et al.* [2000], Satirapod and Rizos [2005], Choi [2007], Haines *et al.* [2013], Moore *et al.* [2014], Fuhrmann *et al.* [2014]

x n) and x the unknown parameter vector of type (n), the observation equation can be expressed as:

$$v = Ax - b \tag{2.1}$$

The vector v (m x 1) comprises the observation corrections (or residuals). With the matrix P (m x m) being the symmetric weighting matrix, this condition can be expressed as a function f (x):

$$f(x) = v^T P v = minimum \tag{2.2}$$

The function f (x) reaches its minimum for partial derivatives with respect to x being equal to and the second derivatives greater than zero. This condition leads to the equation:

$$A^T P^{-1} A x = A^T P^{-1} b \tag{2.3}$$

Rearranging this equation gives the estimated values for $\hat{x}$ as :

$$\hat{x} = (A^T P^{-1} A)^{-1} A^T P^{-1} b \tag{2.4}$$

In the case of a non-linear functional model, as in the case of the GNSS observation equation, the parameters can be determined numerically in an iterative process. For this purpose, approximate values (x_0) are used for the unknown parameters. Based on these values, the improvements $(\hat{x})$ can be computed by the following equation:

$$\delta\hat{x} = (A_0^T P^{-1} A_0)^{-1} A_0^T P^{-1} w \tag{2.5}$$

with $w = b - f(x_0)$ being the observed - computed vector, and $\delta\hat{x}$ improvements to the initial/previous values This procedure is repeated, making use of the updated

parameters until the prior defined convergence criterion is met. After the last iteration, the unknown parameters can be computed as:

$$\hat{x} = x_0 + \delta\hat{x} \tag{2.6}$$

The ESM technique relies on the hypothesis that in a least squares solution with sufficiently high degrees of freedom, the distribution of the undifferenced phase residuals across azimuth and elevation will approximate the systematic site specific errors caused predominantly by multipath effects. If we now introduce an unmodelled systematic error f into the observations, the equations now become:

$$\delta\hat{x} = (A^T WA)^{-1} A^T W(b + f) \tag{2.7}$$

which can be written as:

$$\delta\hat{x} = (A^T WA)^{-1} A^T Wb + (A^T WA)^{-1} A^T Wf \tag{2.8}$$

Thus, $\hat{x}$ is biased by $(A^T WA)^{-1} A^T Wf$. The least squares residuals with a bias become:

$$\hat{v} = A[(A^T WA)^{-1} A^T Wb + (A^T WA)^{-1} A^T Wf)] - (b + f) \tag{2.9}$$

which then leads to:

$$\hat{v} = A(A^T WA)^{-1} A^T Wb - b + A(A^T WA)^{-1} A^T Wf - f \tag{2.10}$$

That is, the least squares residuals are not only a function of the original error, f, but also its propagation term:

$$A(A^T WA)^{-1} A^T Wf - f \tag{2.11}$$

Therefore, it could be concluded that re-iterating the solution using an ESM is unlikely to improve the estimated parameters. However, it is important to first understand how the term $A(A^T WA)^{-1} A^T Wf$ behaves. It is conceivable that, under certain conditions, this term can be small i.e.

$$A(A^T WA)^{-1} A^T Wf << \|f\| \tag{2.12}$$

When the propagation term is very small compared to the size of the bias, then it follows that the residuals will give a very good approximation of the *real* site-specific biases and random errors, the latter which average towards zero through combining multiple days of data. The design matrix A and the weight matrix W, are the

main components controlling the magnitude of the propagation term. Where the design matrix A will be influenced by the geometry of the stations with respect to the satellite orbits and the parameterisation strategy. The weighting strategy for the observations will influence the matrix W.

We may then infer that in regions which have suboptimal geographical coverage for GPS satellite observation, such as the polar regions, should be more suitable to this technique, then equatorial stations. We may also infer that the ESM technique will be most effective for noisy stations, as well as at lower elevations where the weighting of observations will be reduced and therefore the influence of the propagation term will be less.

2.3 Reference solution

In this section we will give an overview of the processing methodology that has been used to obtain our standard global GPS solution. The results from the standard solution were computed at ANU and MIT and submitted to ITRF as part of the IGS 2nd reprocessing campaign. The ANU/MIT solution is recognised as being among the top performing solutions.

Since the official start of the International GNSS Service (IGS) in 1994 there have been considerable improvements in the processing strategies and modelling of global GPS solutions. When a change in the processing strategy, or in the realization of the reference frame occurs, this causes undesirable systematic effects in the parameter time series. Some of these effects (reference frame changes) can be corrected by a quick re-computation of solutions based on normal equations. However changes in the parameterisation or observation modelling require a reprocessing starting at the observation level. This is a large computational load, and is not often repeated, to date only two re-processing efforts have been carried out in the history of the IGS. The current trend is to carry out a reprocessing effort upon the change of IERS conventions, which define the fundamental geophysical models that should be applied, this usually coincides with a new realization of the ITRF solution.

The second reprocessing effort has recently been completed by several analysis centres, involving the reprocessing of 20 years of GPS observations from 1994 to the end of 2014. The base solution from which we will derive our ESM models from, and the solution which we will compare our results to, was submitted as a joint ANU/MIT solution as part of the 2nd IGS re-processing effort. This solution has applied the latest models and methodologies to date, as well as providing a consistent analysis. For this thesis we will focus our analysis on the period between 2010 through to the end of 2013.

2.3.1 GPS data modelling and processing scheme

GPS processing time increases exponentially with the number of stations. To overcome this limitation we split the global network into several sub-networks, to process each sub-network independently, and then to combine each of the sub-networks into a unique daily solution. The networks were selected using an algorithm which tries to ensure the best network geometry for each sub-network, based on the data available for that day ensuring at least two common stations in each sub network, while giving priority to IGS reference frame stations. This results in approximately 80 stations per sub-network, and a total of 300 to 350 stations being processed (see Fig 2.1). We then added in special interest secondary GPS sites, which were co-located with a GPS station and another geodetic techniques. We will utilise these short baseline solutions in a case study analysis in later chapters.

Most of the stations belong to the IGS network, however some stations come from regional networks belonging to EUREF, CORS, SOPAC, ARGN, amongst others. The number of continuous stations processed changes on a daily basis, but there is a clear trend as seen in (with ambiguity success rate) Fig 2.2.

2.3.2 Process strategy

We have chosen to adhere to a philosophy of applying modelling at the observation level whenever possible. This approach is particularly important in the estimation of site-specific model from the phase residuals, as we need to remove as many known model able effects from the solution, to prevent any leakage into the site-specific models obtained from the post-fit phase residuals. We have used double-differenced ionosphere-free carrier phase data, processed using GAMIT 10.5 [Herring *et al.*, 2010]. An elevation cut-off angle of 10° was applied to the raw observations, any observation files less than 5 hours in duration were rejected. The least squares solution is run in two iterations, for the first iteration, a pre-fit solution is run with 10 minute decimated data using an elevation weighting of observations, this solution is used to update the model parameters. Then a second iteration is run (a post-fit solution) with 2 minute sampled data, and the observations are weighted using the phase residuals from the first iteration (see eq. 2.13).

$$\sigma^2 = a^2 + \frac{b^2}{sin(e)^2} \tag{2.13}$$

Code bias corrections are applied for the whole period using monthly tables from the Astronomical Institute of the University of Bern (AIUB). Real-valued double differenced phase cycle ambiguities are estimated, except when they can be resolved

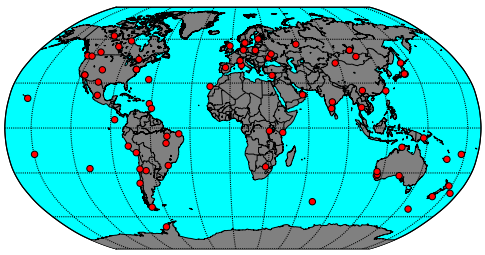

(a) Network 1

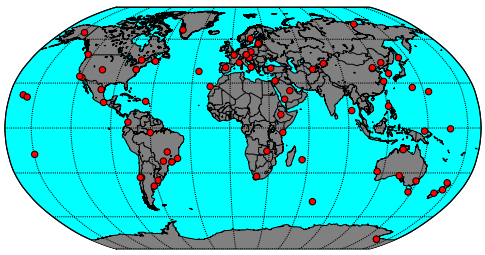

(b) Network 2

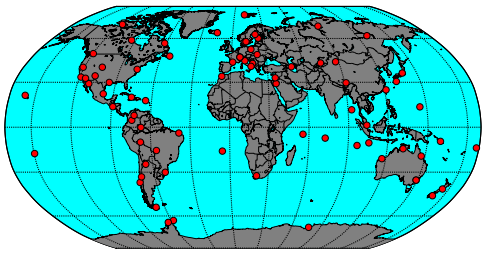

(c) Network 3

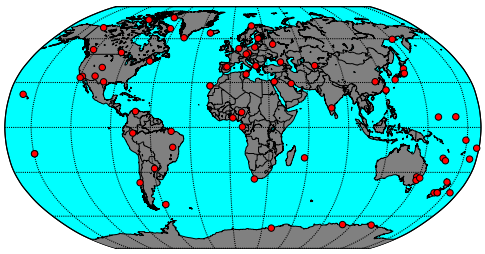

(d) Network 4

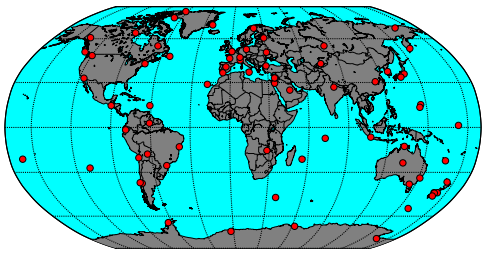

(e) Network 5

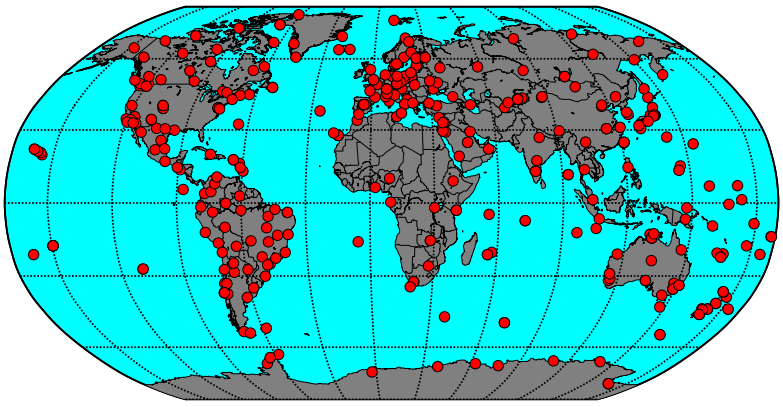

(f) Networks combined

Figure 2.1: Network Selected for 2012 DoY 100

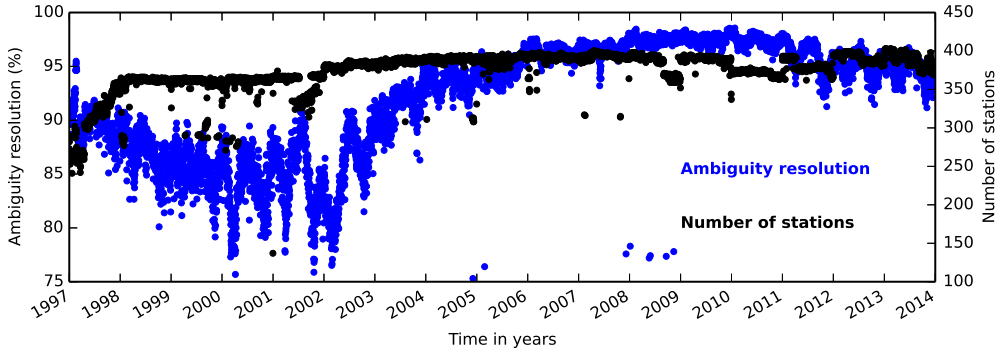

Figure 2.2: Number of GPS stations processed, and ambiguity resolution success rate

confidently. In this case they are fixed using the Melbourne-Wubbena wide-lane to resolve the L1-L2 cycles and then estimation to resolve L1 and L2 cycles. For satellite antennas, satellite-specific z-offsets, and block specific nadir angle-dependent absolute PCV [Schmid *et al.*, 2007] are applied. For receiver antennas L1/L2 offsets, and azimuth-dependent, when available and elevation dependent absolute PCV are applied.

A priori zenith hydrostatic (dry) delay values are extracted by station from the ECMWF meteorological model through VMF1 grids [Boehm *et al.*, 2006a]. Both dry and wet VMF1 mapping functions are used. Two gradients are estimated for each day, and each station. The first-order term of the ionosphere refraction is eliminated by forming the ionosphere-free linear combination (L_3) of the L_1 and L_2 measurements. Second and third order ionospheric corrections have also been applied [Petrie *et al.*, 2010].

The pole tide correction follows IERS 2010 and was applied at the observation level. Solid earth tides are corrected following the IERS 2010 conventions and ocean tide loading is corrected using the FES2004 model [Lyard *et al.*, 2006]. Atmospheric pressure loading for S1 and S2 terms was applied; the non-tidal loading corrections were applied at the observation level, and removed from the coordinate time series before submission of the final coordinate solution. Earth orientation parameters (EOP) are estimated daily and semi-diurnally as a piecewise linear model, with a priori values from the IERS Bulletin. UT1-UTC offsets are constrained to their a priori values.

The EGM2008 geo-potential field has updated values for time variations of low-degree coefficients as per IERS 2010. The satellite-radiation parameters take into account reflected and retransmitted radiation from Earth [Rodriguez-Solano *et al.*, 2012]. Block dependent transmitted thrust values for the GPS satellites as well as general relativity for the Schwartchild term and Lens-thinning and de Sitter effects

Table 2.2: Processing parameters applied to global solution

Model/Parameter	Model/Parameter Applied
Software	GAMIT 10.5 [Herring *et al.*, 2010]
Data Rates	120 (s)
Elevation Cut-off Angle	10°
Observation Weighting	Elevation Weighting: $a^2 + (b^2/sin^2(e))$ with a, b derived from post-fit phase residuals
A priori zenith	VMF1 [Boehm *et al.*, 2006a]
Antenna phase variation	IGS08.atx [Schmid *et al.*, 2007]
Orbits	IGS Final (apriori)
Solid Earth (tide & pole tide)	IERS2010
Ocean loading	FES2004 [Lyard *et al.*, 2006]
Atmospheric Tides	Tidal and Non-tidal applied at observational level level
Ionospheric Correction	2nd and 3rd order IGRF11 [Petrie *et al.*, 2010]
Satellite Yaw	kouba [Kouba, 2009]
Geo-potential	EGM2008 [Pavlis *et al.*, 2012]

(not J2). Changes in GPS satellite orientation during eclipse period follow the model of [Kouba, 2009]. Satellite positions and velocities are adjusted in 24 hour arcs taking IGS final orbits as a priori. Loose constraints have been applied on all parameters, with the solution vector and VCV matrix saved for each network. The loose network solutions are then combined into daily network solutions in GLOBK[Herring *et al.*, 2010], and rotated into the ITRF08 reference frame.

2.3.3 Orbit estimation

Initially the Berne orbit model [Beutler *et al.*, 1994] is used with the full 15 parameters (6 initial conditions, 3 solar radiation pressure (SRP) constant terms in the direct, Y-axis and orthogonal B axis direction, and 3 pairs of the sine and cosine once-per revolution (OPR) terms directed along the same axes. The parameters are expressed as scale factors on the direct radiation force. Generally this model is poorly constrained for 24-hour orbit arcs and when all 6 OPR terms are estimated the Earth centre of mass location and the rates of change of the Earth orientation parameters, and particularly UT1 are poorly determined. To address this over parameterisation

problem a method to eliminate unnecessary parameters is used. From the weekly solution where all of the GPS satellite orbit terms are estimated, a decision based on the statistical significance of each SRP, OPR parameter is used to determine the parameters to be retained in the final analysis. The B-axis OPR term is always estimated, however the direct and Y-axis OPR terms are selected for estimation based on the significance of the estimates with respect to their nominal a priori values for that week. For the majority of weeks only a few satellites require estimation of more than the B-axis OPR term. Once the specific OPR parameter set has been decided, daily estimates of the OPR terms are used to determine the level of random walk process noise. The random walk noise is adjusted so that the chi-squared values are close to 1, this ensures that that we obtain a standard deviation which matches the observed scatter for the week. The weekly solution stack is compiled allowing for daily estimates of SV IC's (position, velocity and SRP's). A similar procedure was applied to the estimation of SRP parameters to determine at what level stochastic process noise should be applied to these parameters. Once a suitable set of OPR parameters, and random walk process noise characteristics have been determined, a final weekly forward and backward kalman filter combination run was carried out from which the final orbits are recovered. A loose combination of the daily solutions is then rerun fixing the estimated orbit parameters, from which the fiducial free estimates of the station coordinates, and EOPS are recovered.

2.3.4 Clock estimation

To generate the clock solutions a separate analysis is performed to determine the clocks, after a weekly position and orbit solution had been completed. The analysis takes advantage of the fact that if a weighted least squares solution is repeated, with some of the parameters held fixed to their WLS estimates, then the other parameter estimates will retain their values from the original solution (note however that the standard deviation will be affected). The clocks are estimated by running an analysis with the orbits, EOPs, and station positions tightly constrained to their estimates from the weekly combination, and use a direct one-way clock estimates to generate the clock values. The apriori clock model, offsets and linear trends is based on fitting the broadcast ephemeris clocks. The clock solution uses a smaller network than the original analysis (approximately 3-networks of 40 stations) based on the quality of the clock estimates in the original final run. The results from the three sub-networks are aligned and averaged. The clock estimates are generated at a 30-second rate and decimated to a 15-minute rate for all ground sites except the reference site. The reference site and satellites are all reported at a 30-second rate. The alignment of the

clocks is an ensemble average over the sites with smallest RMS scatters about linear trends, and the lowest RMS scatter site is chosen as the reference site. The RMS fit of these clocks is usually less than 30ps (equivalent to 10mm in distance).

Position time-series

Initially apriori discontinuities were added to the time series from the ITRF2008 list, then additional discontinuities were added to stations, which were close to the epicentre of earthquakes larger than magnitude 7. The metadata of each station was screened and a discontinuity was added to the time-series if a change of antenna type occurred. Each discontinuity was checked for statistical significance. Then the residual position time series of each station are visually examined to look for any missing discontinuities. All outliers were removed in an iterative process, progressing from the largest to the smallest, to be within an absolute limit of 20mm and within 4 normalised standard deviations of the mean. In our comparison of GPS time series from different solutions we have applied the same offset file determined from our base solution. We choose to do this as the selection of what is considered to be a significant offset is still not well defined.

2.4 Time-series analysis techniques

2.4.1 Wavelets

We utilise the wavelet transforms to analyse simulated and real GPS time series, as this technique can be used on time series which contain non stationary power at many different frequencies [Daubechies, 1990]. The term wavelet function is used to generically to refer to the orthogonal or non-orthogonal wavelets. The term wavelet basis refers only to an orthogonal set of functions. The use of an orthogonal basis implies the use of the discrete wavelet transform, while a non-orthogonal wavelet function can be used with either the discrete or the continuous wavelet transform (CWT). We will use the CWT. To ensure that the wavelet transforms at each scale s is directly comparable to each other, and to the transforms of other time series, the wavelet function at each scale s is normalised to have unit energy. In choosing the wavelet function, there are several factors which need to be considered (for more discussion see Farge [1992]), see Table: 2.3 for a summary. The non-orthogonal transform is used for time series analysis, where smooth, continuous variations in wavelet amplitude are expected. A complex wavelet function will return information about both amplitude and phase and is better adapted for capturing oscillatory behaviour.

The width of a wavelet function is defined as the *e*-folding time of the wavelet

Table 2.3: Factors influencing the choice of wavelet are often dependent upon the type of analysis being carried out

basis	orthogonal signal-processing compact representation of the signal, however does have aperiodic shifts	non-orthogonal time-series highly redundant at large scale no shifts of signal in time
type	real good at isolating peaks and discontinuities	complex information in amplitude and phase - captures oscillating behaviours
width	narrow high resolution in time, poor resolution in frequency	broad poor resolution in time high resolution in frequency

amplitude. The balance between the width in real space and the width in Fourier space determines the resolution of a wavelet function. A narrow (in time) function will have good time resolution, but poor frequency resolution, while a broad function will have poor time resolution, yet good frequency resolution.

In our subsequent time series analysis we use a commonly know Morlet wavelet which is both non-orthogonal and complex. We have chosen to use the Morlet wavelet, which is constructed from a plane wave modulate by a Gaussian:

$$\psi_0(\eta) = \pi^{-1/4} e^{i\psi_0\eta} e^{-\eta^2/2} \tag{2.14}$$

where ψ_0 is the non dimensional frequency, here taken to be 6 to satisfy the admissibility condition [Farge, 1992].

Once a wavelet function has been chosen, it is necessary to choose a set of scales s, to use in the wavelet transform. For non-orthogonal wavelet analysis, one can use an arbitrary set of scales to build up a more complex picture. It is convenient to write the scales as fractional powers of two:

$$s_j = s_0 2^{j\delta j} j = 0, 1, ..., JJ = \delta_{j^-1} log_2(N\delta t/s_0) \tag{2.15}$$

where s_0 is the smallest resolvable scale and J determines the largest scale. The s_0 should be chosen so that the equivalent Fourier period is approximately $2\delta t$. The choice of a sufficiently small δj depends on the width of the spectral space of the wavelet function. For the Morlet wavelet, a δj of about 0.5 is the largest value that still gives adequate sampling in scale.

As we are dealing with finite length time series, errors will occur at the beginning and end of the wavelet power spectrum. In our implementation the time series

is padded with sufficient zeros to bring the total length N up to the next higher power of two, thus limiting the edge effects and speeding up the Fourier transform. Padding with zeros introduces discontinuities at the endpoints and, as one goes to larger scales, decreases the amplitude near the edges as more zeros enter the analysis. The *cone of influence* (COI) is the region of the wavelet spectrum in which the edge effects become important and is defined here as the *e*-folding time for the autocorrelation of wavelet power at each scale. This *e*-folding time is chosen so that the wavelet power for a discontinuity at the edge drops by a factor of e^{-2} and ensures that the edge effects are negligible beyond this point.

The size of the COI at each scale also gives a measure of the decorrelation time for a single spike in the time series. By comparing the width of a peak in the wavelet power spectrum with this de-correlation time, one can distinguish between a spike in the data (i.e. random noise) and a harmonic component at the equivalent frequency. The COI is indicated in the subsequent figures by a thick grey line. Anything below this grey line should be interpreted with caution, as edge effects can be significant.

The peak of a wavelet does not necessarily occur at the frequency $s^{-}1$. The relationship between the equivalent Fourier period and the wavelet scale can be derived analytically for a particular wavelet function by substituting a cosine wave of a known frequency and computing the scale s at which the wavelet power spectrum reaches it maximum [Meyers *et al.*, 1993]. For the Morlet wavelet with $\omega_0 = 6$, this gives a value of $\lambda = 1.03s$, where λ is the Fourier period, indicating that for the Morlet wavelet the wavelet scale is almost equal to the Fourier period.

Since the wavelet transform is a bandpass filter with a known response function, it is possible to reconstruct the original time series using either deconvolution or the inverse filter. This is straightforward for the orthogonal wavelet transform, but for the CWT it is complicated by the redundancy in time and scale. However this redundancy also makes it possible to reconstruct the time series using a completely different wavelet function, the easiest of which is the delta (δ) function [Farge, 1992]. The reconstruction process is good for accessing the accuracy to ensure that sufficiently small values of s_0 and δj have been chosen, see [Torrence and Compo, 1998] for more information.

To determine the significance levels for either Fourier or wavelet spectra, one first needs to choose an appropriate background spectrum. It is then assumed that different realisations of the geophysical process will be randomly distributed about this mean or expected background, and the actual spectrum can be compared against this random distribution. For many geophysical phenomena, an appropriate background spectrum is either white noise (with a flat spectrum) or red noise (increasing power with decreasing frequency).

Many geophysical time series can be modelled as either white noise or red noise. A simple model for red noise is the univariate lag-1 autoregressive (AR(1), or Markov) process:

$$x_n = \alpha x_{n-1} + z_n \tag{2.16}$$

where α is the assumed lag-1 autocorrelation, $x_0 = 0$, and z_n is taken from Gaussian white noise. The discrete Fourier power spectrum of eq. 2.16, after normalising is:

$$P_k = 1 - \alpha^2 / 1 + \alpha^2 - 2\alpha cos(2\pi k/N) \tag{2.17}$$

where $k = 0..N/2$ is the frequency index. Thus by choosing an appropriate lag-1 autocorrelation, one can use eq 2.17 to model a red-noise spectrum. Note that $\alpha = 0$ gives a white noise spectrum.

The null hypothesis is defined for the wavelet power spectrum as follows: It is assumed that the time series has a mean power spectrum, possibly given by eq 2.17 . If a peak in the wavelet spectrum is significantly above this background spectrum, then it can be assumed to be a true feature, with a certain percent confidence.

The normalised Fourier power spectrum is given by $N|x_k|^2/2\sigma^2$, where N is the number of points, x_k is a normally distributed random variable, then both the real and imaginary parts of x_k are normally distributed. Since the square of a normally distributed variable is chi-square distributed with one degree of freedom (DOF), then $|x_k|^2$ is chi-square distributed with two DOFs. Denoted by χ^2. To determine the 95th percentile value for χ^2 one multiplies the background spectrum by the 95th percentile value for χ^2.

The same will apply to the wavelet spectrum [Torrence and Compo, 1998] such that at each point (n,s) the wavelet power spectrum will have a χ^2 distribution for a red-noise process:

$$N|x_k|^2/\sigma^2 => 1/2P_k\chi_2^2 \tag{2.18}$$

at each frequency index k, and "=>" indicates 'is distributed as'. The corresponding distribution for the local wavelet power spectrum is:

$$|W_n(s)|^2/\sigma^2 => 1/2P_k\chi_2^2 \tag{2.19}$$

at each time n and scale s. The $1/2$ removes the DOF factor from the χ^2 distribution. The value of P_k is the mean spectrum at the Fourier frequency k that corresponds to the wavelet scale s. The relation between k and s, is independent of the wavelet function. After finding an appropriate background spectrum and choosing a particular confidence for χ^2 such as 95%, one can then calculate at each scale, and draw 95%

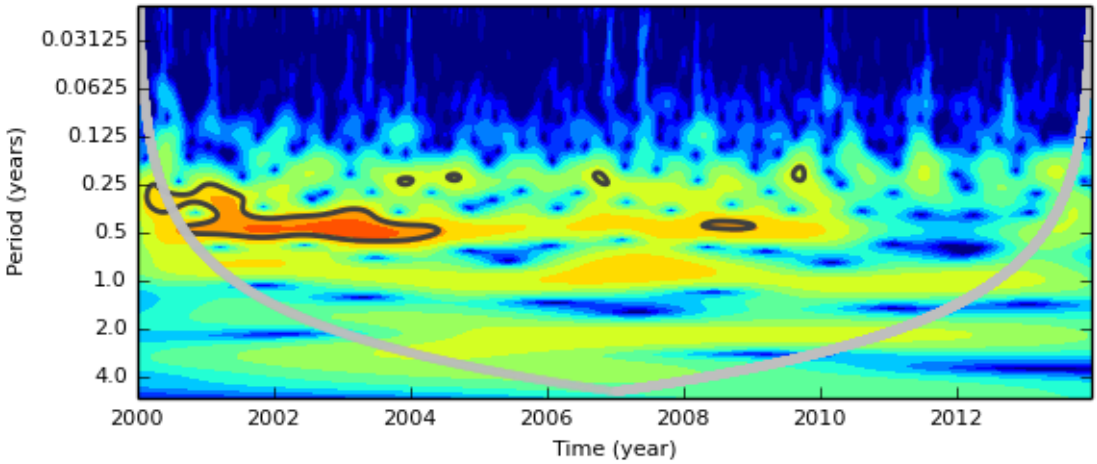

(a) Morlet CWT, for h = 0.17 m

Figure 2.3: An example of a Morlet CWT transform. The left axis is the Fourier period in years, the black contour lines enclose regions of great than 95% confidence for an estimated background noise level and the thick grey line demarcates the region of 'cone of influence' where edge effects become important.

confidence contour lines.

2.4.2 Nature of noise in GPS time series

It is important to know the noise model of the data since the noise, both its amplitude and its distribution in the frequency domain, affects the estimate of displacement rate and its standard error; these are the principal values obtained from geodetic measurements. The residual time-series obtained from continuous GPS stations has a 'coloured' power spectrum, with greater power at lower frequencies. As with other geodetic time-series the time-correlated noise in GPS time series appears to represent a power-law process [Williams *et al.*, 2004]. Power-law noise is distinguished in the frequency domain by the relationship between power (P) and frequency (f),

$$P(f) = P_0(f/f_0)^k, \tag{2.20}$$

where P_0 and f_0 are normalising constants, and k is the spectral index [Mandelbrot and Van Ness, 1968]. Special cases of spectral indices of 0, -1 and -2 correspond to white, flicker, and random walk noise, respectively. While noise generated by some geophysical process seems to produce power-law noise with a particular integer spectral index, fractional values of k have been inferred for other process [Williams, 2003]. More negative values of the spectral index correspond to greater degrees of time

correlation in the time series, with greater noise power at periods approaching the time-series length. Greater power in the lowest frequency noise consequently creates greater levels of uncertainty in estimating the trend over the length of a full record.

Ordinary least-squares regression assumes that the residual noise is white, with no temporal correlation between the residuals. Consequently, determination of linear trends from time series with time-correlated noise can underestimate the uncertainty on the rate parameter significantly [Zhang *et al.*, 1997]. We have used a maximum likelihood estimation (MLE) technique [Williams, 2008] to determine linear model parameters with realistic uncertainties while simultaneously solving for the magnitude of white and coloured noise in time series.

If a time series is assumed to contain two noise sources, then the overall length of the series must be at least longer than the crossover period. Typically the length of the series must be sufficient for the power law noise to be visible over the white noise. [Bos *et al.*, 2013] pointed out that it is still not clear what causes the noise in GPS time series, nor is it know when the noise processes start. For instance this could be the moment the receiver is turned on, from the launch of the first satellite, or from the beginning of a geophysical signal. They used this uncertainty to let the noise start at some arbitrary time in the past, with a recommended value of 1000 days.

2.5 Summary

In this chapter we have established that it is theoretically possible to use least squares residuals to account for unmodelled effects. We discussed in detail the methodology used to compute the reference solution, from which the post-fit residuals were obtained for the site-specific models. This reference solution will be the basis from which we compare the models performance against. We will also look at the effectiveness of applying the modelling techniques to a short baseline kinematic processing scenario.

Before we detail the different modelling techniques, we will first assessing the impact of site-specific estimates can have upon the GPS estimates. We will also use the simulation to testing the theoretical finding that least squares residuals can be used to recover unmodelled effects through a number of different simulation scenarios.

Chapter 3

Impact of site-specific errors

Using simulations we can isolate site-specific errors and investigate in detail how they can propagate through least squares solutions. The purpose here is not to develop a state-of-the-art forward model of multipath, but to utilize the simulator as a tool to generalise how site-specific biases affect GPS positioning. In addition, the simulations can help to determine if the least squares residuals can be used to effectively model the site-specific bias under different scenarios. In this chapter we will look at both the short-term impact of site-specific errors, as well as the long-term impact on GPS time series.

3.1 Simulator

The GPS simulator is based on the undifferenced GPS observable, and is conceptually similar to the simulator used by Santerre [1991]. The simulator has been tested in a similar way to that undertaken by King *et al.* [2003], and subsequently further verified by Penna *et al.* [2007] and King and Watson [2010].

Unless otherwise stated coordinates were estimated once per 24h session, tropospheric zenith delays once every two hours, and the receiver clock is estimated every epoch. The satellite orbits, clocks and earth orientation parameters have been held fixed. Ambiguities were held fixed and the simulated observations were weighted by elevation angle with a 10° elevation cut-off angle applied. The station location was set to an arbitrary position of 45°S, 140°E, before being allowed to vary in later analysis. All simulations were run for one 24 hour period using the adopted date of January 1, 2012, with a sampling rate of 120s. Random white noise with a magnitude of 1 mm was added to the b term in Eq. 2.7 in addition to the systematic error, which is discussed in detail in section 2.2.

3.2 Short-term impact of site-specific errors

Multipath can have a significant impact on the position estimates obtained from a GPS solution. The investigation in this section was conducted to determine the conditions which produce these large biases into the position estimates, and then to identify those conditions under, which least square residuals will effectively model the site-specific bias. To determine the magnitude of the multipath error in the following simulations we used eq. 1.7.

3.2.1 Observed satellite elevation angle and antenna height

The amplitude and frequency of multipath error varies considerably as a function of the observed satellite angle and the antenna height above the reflecting surface (Fig 3.1). In general, an antenna with reflectors nearby produces a long wavelength periodic signal that varies with the observed signal elevation angle. Whereas, an antenna mounted higher above the reflecting ground surface will experience higher frequency multipath bias at low elevation angles, and lower bias at high elevation angles. The amplitude and frequency of the multipath bias is also dependent upon the observed frequency. Comparison of the simulated multipath bias with the theoretical multipath bias for L1 and L2 reveals that a significantly lower bias for L1, and a differing frequency of variation of range bias with elevation angle.

An amplification of the multipath bias occurs when applying the commonly used ionosphere-free linear combination (L3). This linear combination resulted in a constructive and destructive interference of the multipath bias from the L1 and L2 observations (see Fig. 3.1(c)). The net effect is an amplification of the multipath bias, and an increased variation of range bias with elevation angle.

3.2.2 Multipath estimation error

To what extent can the least-squares residuals be used to model systematic biases, such as multipath? To assess this we developed a metric, which computed the difference between the simulated multipath bias, and the multipath bias modelled from the least squares residuals. This was calculated using the RMS of the difference between the simulated multipath bias and the empirical model derived from the least squares solution, at 0.5° elevation bins with similarly sampled simulated biases (Fig. 3.2). We refer to this metric as the multipath estimation error (*MPE error*). Given the random noise in the simulation has amplitude of 1mm, an MPE error near to this value indi-

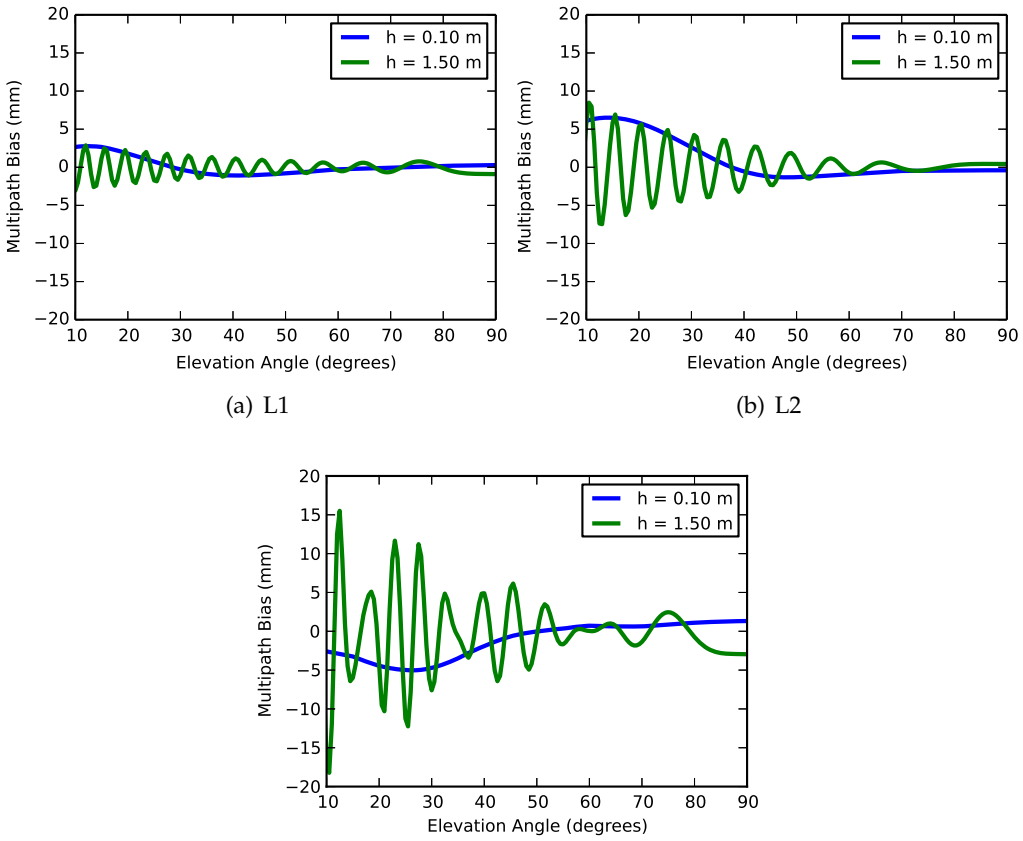

(a) L1

(b) L2

(c) Linear combination L3

Figure 3.1: Simulations showing the variation of the magnitude of multipath biases as a function of elevation angle, for monument heights of 0.10 and 1.50m, and for the GPS frequencies L1 (a), L2 (b) and the linear combination L3 (c), based on eq 1.7

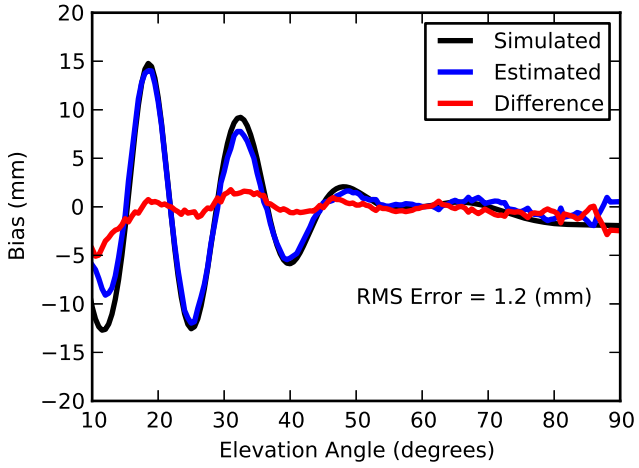

Figure 3.2: Simulated L3 multipath bias and the modelled multipath bias obtained from the simulated least squares residuals for a monument height of 0.5m. The MPE error is calculated from the difference between the two (shown in red)

cates close to perfect recovery of the simulated multipath.

Our simulations show there is a dependency between the MPE error and the monument height (Fig. 3.3). In general the MPE error decreased with increasing monument height. There was a significant peak in the MPE close to 0.17m (see Fig 3.3), and the MPE was higher for low monuments (less than 0.5m). As a result, modelling of multipath from the least square residuals may not be effective for monument heights near 0.17m. Significantly, the least squares residuals could be effectively used to model the multipath bias for the majority of monument heights simulated.

We also investigated the effect of introducing a higher surface roughness value (S) for the simulated multipath bias. Increasing the surface roughness value (S), has the counter-intuitive implication of increasing the signal power returned from the reflected surface. A larger power returned by the reflecting surface has the effect of increase the magnitude of multipath bias across all elevation angles. Figure 3.3 shows there was a linear increase in the MPE error with increasing values of S for all monument heights. This indicated that the ESM performance was degraded for low monuments close to surfaces that reflected a significant proportion of the incoming signal power, such as metal plates. While the larger values of S increased the MPE for all monument heights; the least squares residuals could still be effectively used to model the multipath error for monument heights not located near the peak MPE (h = 0.17m).

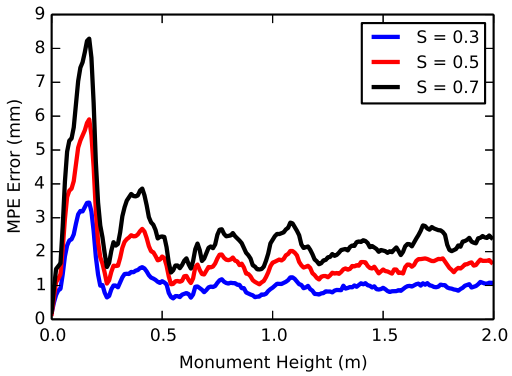

Figure 3.3: Multipath estimation error as a function of monument heights for surface roughness (S) values of 0.3, 0.5 and 0.7. This shows that materials with a higher S value reflect more of the input signal power, which will increase the MPE error. The MPE error peaks for a monument height of 0.17m

3.2.3 Interaction of multipath with weighting and mapping functions

The localized peak in MPE for a monument height of 0.17 m was intriguing. To further investigate why this may be occurring we looked at the interaction of the simulated multipath bias with elevation weighting functions and troposphere mapping functions and how this varied with monument height.

Figure 3.4 shows the correlation-coefficient of a simplified elevation weighting function ($1/sin(e)^2$), and a simplified troposphere mapping function $1/sin(e)$ with the simulated multipath bias for a range of monument heights. While these are simplified weighting and mapping functions, they will serve as a good approximation of more sophisticated techniques used. The correlation coefficient, for both cases, was higher for multipath signals simulated at lower monument heights, with the peak again occurring near a monument height of 0.17m. Therefore for monument heights, close to h = 0.17m.

This suggests that for low monument heights it will be difficult to separate the multipath bias from the errors in the troposphere zenith delay estimation. Given troposphere mapping functions are integral to geodetic positioning our results suggest it is unlikely that an ESM will yield improved parameter estimates in such cases.

3.2.4 Processing parameters

Having identified an interaction of simulated multipath bias with elevation dependent weighting and a troposphere mapping function. We were then faced with a number of questions, which needed to be investigated further. What effect were the choices in our processing parameters having upon the propagation of multipath

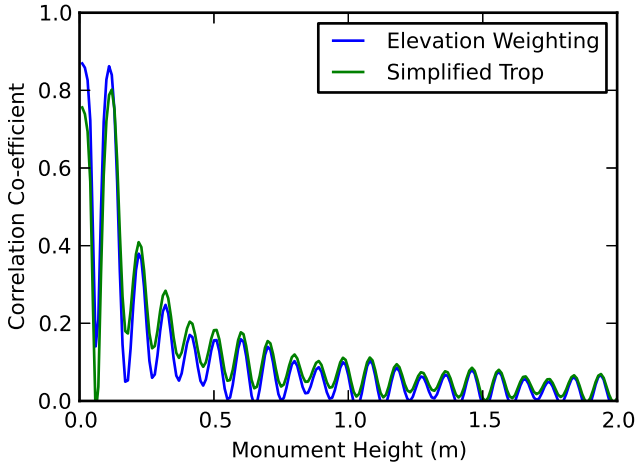

Figure 3.4: Correlation coefficient of the simulated multipath with a simplified troposphere zenith delay mapping function ($1/sin(e)$) and a simplified data weighting function ($1/sin(e)^2$), calculated for a range of monument heights

biases into the GPS time series, and to what extent will the choices have upon the recovery of the multipath bias from the least squares residuals?

Variations of the processing methodology to include or exclude clock and troposphere estimation are usually determined by the processing methodology (PPP vs baseline double-difference) and the type of network being processed (local network vs regional/global network). We found that these different processing methodologies can have a significant impact on how the multipath bias propagates through the solution.

Firstly we simulated the standard PPP method, where the receiver clock is estimated at every epoch and the troposphere zenith delay (TZD) is estimated every two hours. For this scenario there were significant clock and height bias of up to 25mm for low monument heights $< 0.25m$ (blue line of Fig. 3.5(a)), with a peak in the magnitude of the biases at a monument height of h = 0.17m. Note that the effect of multipath on troposphere estimates is following the negative correlation between the height and troposphere bias of approximately 3:-1 [Beutler *et al.*, 1987]. For monument heights below 1.5m there was a significant oscillating in height bias ranging between $\pm 5mm$. The MPE was small for all monument heights, with the exception for those near h = 0.17m, indicating that the use of LS residuals would be effective for this processing scenario.

Removing the requirement for troposphere zenith delay estimation resulted in a significant reduction on the effect multipath bias had upon the estimated parameters. For instance the peak bias in height and clock estimates decreased from 3cm to 1cm

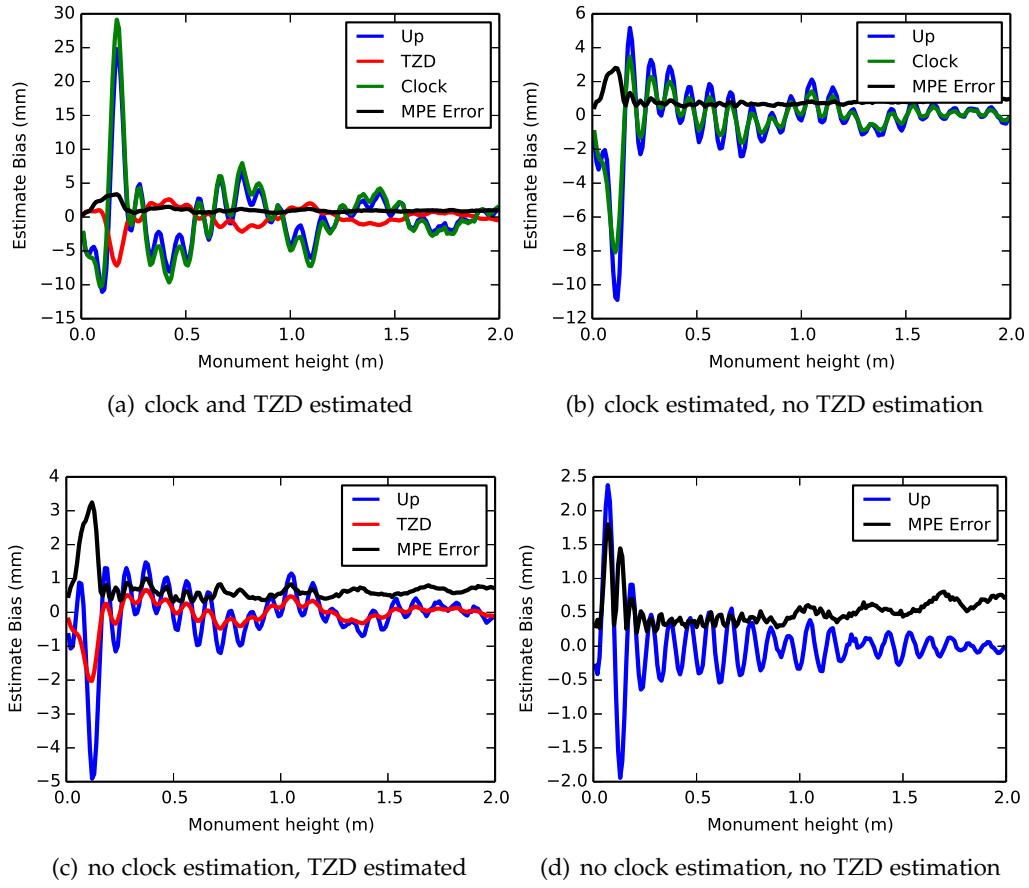

(a) clock and TZD estimated

(b) clock estimated, no TZD estimation

(c) no clock estimation, TZD estimated

(d) no clock estimation, no TZD estimation

Figure 3.5: The impact of processing parameters on the propagation of multipath bias and resulting effect on the estimated parameters for different monument height

(see Fig. 3.5(b)). Also of note, the peak biases was no longer centred on h = 0.17, and had shifted to a lower monument height of h = 0.1m with a magnitude of -10mm. However there still remained a significant peak for h = 0.17m resulting in 5mm bias in height estimation.

Without clock estimation the magnitude of the height and TZD bias also decreased for all monument heights (see Fig. 3.5(c)). The peak bias was at the same location as the previous simulation without TZD estimation, but had halved in magnitude to -5 mm. Removing both troposphere and clock estimation resulted in the multipath bias having a much smaller impact upon the height estimates which ranged between 2.5 mm to -2 mm.

For all of the processing scenarios investigated here the MPE was small in magnitude for all monument heights, with the exception for h = 0.17 m.

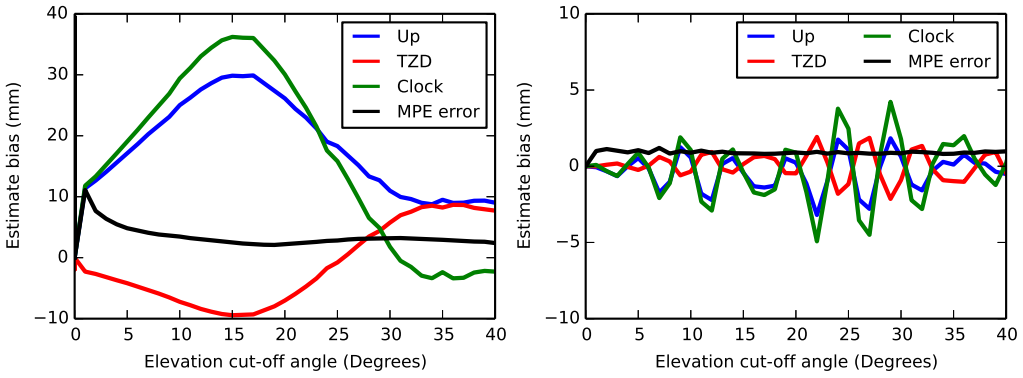

(a) h = 0.17 m (b) h = 1.5 m

Figure 3.6: Impact of changing the elevation cut-off angle upon the propagation of a multipath bias into the estimated parameters of height, TZD, clock, and the effects upon MPE for monument heights of (a) h = 0.17 m and (b) h = 1.50 m.

3.2.5 Elevation cut-off angle

To investigate the effects of applying a different elevation angle on the propagation of multipath we ran a series of simulations which varied the elevation cut-off angle from 0° to 40 °. The simulations were run for two antenna heights, firstly with h = 0.17 m, where we expect the peak in multipath bias propagation, and then for a monument height of h = 1.5, where we expected to see little impact of multipath upon the estimated parameters.

We found that the minimum cut-off elevation angle had a significant impact on the estimated parameters, but it had negligible impact on the recovery of the multipath bias from the simulated least squares residuals provided an elevation mask greater than 5° is used (see Fig. 3.6).

Notably the presence of a large reflective object close to the antenna resulted in the magnitude and variation of the error in the estimated parameters to become dramatically large, with just a small change in elevation cut-off angle. This high sensitivity of the estimated parameters to elevation cut-off angle implies that it will be difficult to obtain accurate and consistent estimates of height, clock or TZD parameters for low monument heights. For instance, a small change in the minimum elevation angle from 10° to 15° can change the propagation of the multipath bias into the vertical position estimate by 10 mm. However the change in elevation cut-off angle has little impact upon the MPE. As the MPE values are small we can therefore expect to see significant improvements for low monuments.

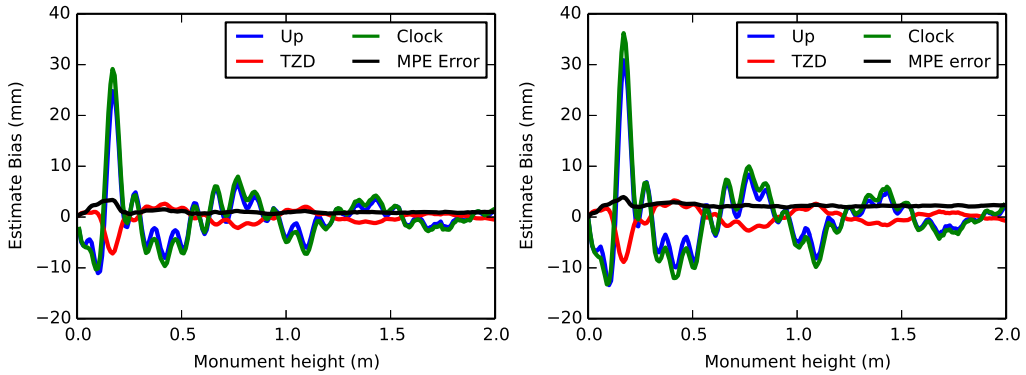

(a) Position estimated once per day (b) Position estimated once every 120 s

Figure 3.7: The impact of the multipath bias upon estimated parameters when the frequency of positioning estimates is increased from once a day, to every epoch.

3.2.6 Frequency of position estimates

The propagation of the multipath bias into height estimates was amplified when the frequency of position estimation was increased from an estimate of once a day to every epoch. For the monument height of h = 0.17 m, there was an increase of 10 mm in the height bias. Over the range of monument heights there was an amplification of approximately 1/3 of the original bias. The effect may even be larger than shown here for kinematic positioning. As the results have been averaged over a complete day, typically kinematic positioning is only carried out for short durations, and consequently will be more dependent upon the satellite geometry at the time of observation.

3.2.7 Influence of station location

To test the influence of a stations location on the propagation of multipath into the estimates, the latitude of the station was changed in 1° increments. The position was estimated once every day, troposphere was estimated every two hours, and the receiver clock was estimated every epoch. The simulations were run for the low monument scenario, h = 0.17, and the high monument scenario h = 1.5 m.

For the high monument, little latitudes dependence was found (see Fig. 3.8). However, for the low monument height, h = 0.17 m, there was a significant dependence on latitude. At latitudes higher than ±60°, close to the inclination of the orbit plane, the performance of the ESM starts to rapidly degrade.

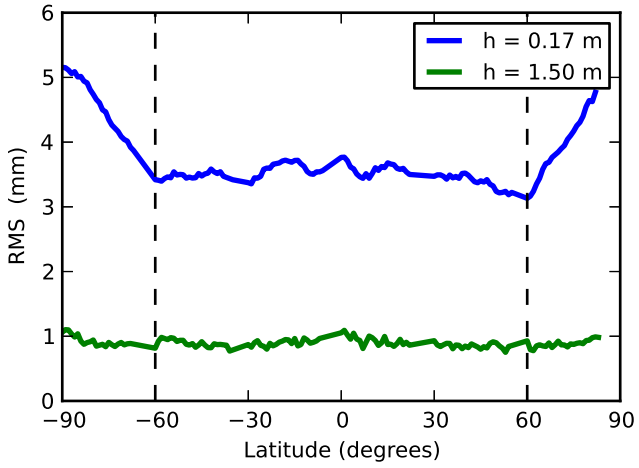

Figure 3.8: The influence of a stations latitude upon the MPE for two different monument height scenarios of 0.17 m and 1.5 m. At latitudes above $\pm 60^{\circ}$ (denoted by dashed vertical lines) there was a poleward increase in the MPE RMS for the low monument scenario.

3.2.8 Antenna

Different types of antennas can exhibit substantial variations in electrical properties, which affect how a reflected signal is attenuated by the antenna. The magnitude of the multipath bias will therefore be dependent upon the antenna type used. Figure: 3.9 demonstrates the effects of two different antennas types when there respective antenna Left hand circular polarized (LHCP) gain measurements are taken into account. The LHCP gain measurements were obtained from anechoic chamber calibrations, which given an indication of how much reflected signal will be rejected by the antenna. The LEIAT504 is a traditional choke ring antenna commonly deployed in the IGS network. Whereas the LEIAR25 is a newer design using a pyramid structure of concentric choke rings designed to provide for multipath rejection at a much broader range of frequencies (as will likely be used by future GNSS constellations).

The theoretical response of the antennas to the simulated multipath exhibit the same frequency with change to monument height, however the amplitude is significantly different (see Fig: 3.9). This was particularly apparent for low monuments heights. The bias in the estimated parameters from the LEIAT504 antenna exhibits a single prominent peak. Whereas using the LEIAR25 antenna there were two significant peaks of opposite sign within a small change in monument height (approx. < 0.2 m). These simulations showed that some care needs to be taken in the interpretation of results obtained from previous and subsequent simulations. That is the magnitude, and the location of the peak biases can change significantly depending upon the antenna's characteristics. Nonetheless, simulations can still provide us with

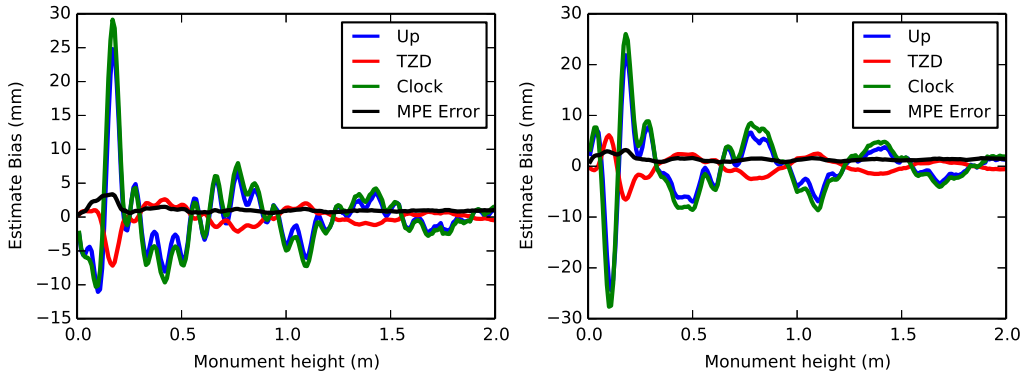

(a) LEIAT504 Antenna (b) LEIAR25 Antenna

Figure 3.9: The impact of antenna type on the propagation of multipath biases, shown over varying monument heights.

a basis to generalise the possible effects of site-specific errors upon GPS time series.

3.2.9 Radomes

There have been many reports on the impact of unmodelled radomes, and there effect on positioning results [e.g. Baire *et al.*, 2013]. For instance, offsets in time series are frequently reported to be caused by the addition or removal of an uncalibrated radome.

Uncalibrated radome

We have approximated the effects an uncalibrated radome on the positioning results by taking the difference in published type mean calibrations of antennas with and without an installed radome, obtained from the IGS (igs.atx). The differences in the absolute PCV values were then used as the input bias to be propagated through the PPP simulator.

The radome effect on the positioning solution will depend on the design of the radome, it's construction material, and how it was installed on the antenna. The effect of differing radome geometry was demonstrated by the significantly different positioning results obtained from the SCIT and SCIS radomes, two radomes which are constructed from the same material and installed similarly, but have different geometry resulting in significant differences in height (see Table 3.1). Each radome type had a unique impact upon the positioning results, highlighting the importance of calibrating the radome with each antenna type. The MPE error is of similar magnitude for all of the radomes.

Table 3.1: Simulation of uncalibrated radomes.

Radome	MPE error (mm)	Height bias (mm)	TZD (mm)	Clock (mm)
TRM59800.00 SCIT	1.6	2.1	-1.2	-0.1
TRM59800.00 SCIS	1.4	-6.1	0.5	-8.8
ASH701945C_M PFAN	1.5	-3.5	0.1	-4.5
ASH701945C_M SNOW	1.6	-3.2	1.8	-7.1
ASH701945C_M OLGA	1.3	5.8	-2.8	7.6

The majority of uncalibrated radomes in the current IGS network have a physical design which make it difficult to calibrate the radome using the robot. The difficulty of correctly calibrating these types of radome is probably causing a significant impact on the positioning results. Therefore the ESM approach may be the only practical method available to account for the potential biases resulting from uncalibrated radomes.

Material change

The SCIGN radome refers to two types of radome types, the SCIT(tall) and SCIS (short) radomes. The SCIS radome was constructed to be coincident with the physical centre of the AOAD/M_T antenna, whereas the SCIT was designed to be concentric to the phase centre of the AOAD/M_T antenna. Both radomes were manufactured using the same mould and construction materials. Recently, it has been reported that the material (email [IGS-AWG-405]) used as the plastic mould for the SCIGN radome has been changed between 2010 and 2012 from a polycarbonate resin GE Xenoy ®2730 (a UV-stabilised polycarbonate and polyethylene terephthalate (PC-PET) combination) to the polycarbonate resin GE Xenoy ®5220U.

A change of material implies a change in refractive index. Consequently, a change in the radome's characteristics could be possible. To date there has not been any attempt to compare the effect of radome construction material using antenna calibrations of the different radomes. A report was provided by UNAVCO used a series of short baseline tests to demonstrate that the change of radome material does not have any impact on the positioning results [Braun, 2007].

Simulating the effect of radome material on positioning results is difficult, as limited information is available on the physical properties of the radome materials. A similar style material Makroblend ®UT403 (http://www.matweb.com) polycarbonate resin is reported to have a dielectric constant of 3.1 for a frequency range between 100 Hz and 1 MHz, however other sources give a dielectric constant of between 2.8

Table 3.2: Serial numbers of SCIGN radome before and after the change of material

Material	SCIT	SCIS Vertical Screws	SCIS Horizontal Screws
Xenoy 2730U	1 - 2932	1 - 1125	1 - 1560
Xenoy 5220U	2933 - 3578	1126 - 1975	1561 - 1875

Table 3.3: Results from simulations of the effect of concentric radome made from materials with a different refractive index. An the influence processing parameters have upon the results.

Refractive Index	Trop	Clock	RMS (mm)	Height (mm)	TZD (mm)	Clock Delay (mm)
2.1	Y	Y	3.5	-0.7	0.2	2.7
1.7	Y	Y	2.2	-0.6	0.2	1.4
1.3	Y	Y	0.9	0.1	0.0	1.0
2.1	Y	N	3.6	-2.9	0.8	N/A
1.7	Y	N	2.3	1.9	0.5	N/A
1.3	Y	N	1.0	0.7	0.3	N/A
2.1	N	N	3.3	-4.3	N/A	N/A
1.7	N	N	2.1	-2.7	N/A	N/A
1.3	N	N	0.9	-1.1	N/A	N/A
2.1	N	Y	3.5	0.1	N/A	3.5
1.7	N	Y	2.2	0.1	N/A	2.1
1.3	N	Y	0.9	0.0	N/A	0.9

to 4.5 (http://engineeringtoolbox.com).

The refractive index n of a material can be obtained from it's dielectric properties ε, where $n = \sqrt{\varepsilon}$. The effect of radome material changes was simulated assuming the same manufacturing process, plastic mould, and radome wall thickness. The dielectric constant range of polycarbonate resins, ranging from 1.7 to 4.4, was simulated using the corresponding refractive index of 1.3 to 2.1. A radome wall thickness of 3.175 mm was adopted (as used by [Schmidt *et al.*, 2003]).

A concentric radome, with the centre of curvature in line with the average L1+L2 phase centre, will have an isotropic delay, assuming phase centre variations are ignored. Simulations using a concentric radome found that increasing the refractive index caused an increased delay in the arrival of the signal, which produces increased phase residuals and bias estimates (see Table: 3.3). However, the magnitude of the delay does not directly map to the height component. Some of the bias will map into the TZD, with the majority propagating onto the clock delay.

The way the radome bias propagates into the time series is strongly influenced by the estimation of the clock term, whereas the estimation of troposphere parame-

ters has little impact upon the height bias.

The simulations indicate that the changing the radome material to a different polycarbonate resin has a small impact on the positioning results (see Table 3.3). However, this should be confirmed with simulations using calibrated antennas with radomes mad from different materials. As GPS processing parameters could be absorbing the effect of radome material variation into the troposphere zenith delay and/or clock estimates.

3.2.10 Pillar width

The dimensions of a pillar mount have a significant impact on the multipath effect experienced at a station. We looked at the effect of pillar width has upon the biases of a normally benign environment when the planar reflector is 1.5 m away from the antenna. We simulated a range of pillar width from 0.05 m to 0.6 m (similar width to early IGS stations e.g. HOB2, TIDB) and used two different surface roughness values of S=0.3 and S=0.5(see Fig. 3.10). A surface roughness of S=0.3 is characteristic of a concrete pillar, whereas a surface of S=0.5 might give a better representation of a pillar with a large steel plate used to mount the antenna to the concrete pillar. We assumed that the antenna was directly mounted to the base of the pillar with a PCO offset of 0.091 m for L1 and 0.117 m for L2, typical values for the commonly used AOAD/M_T antenna.

As the width of the pillar increases, the MPE error increases; therefore the least squares residuals obtained from a station mounted on a wide pillar are less likely to represent the multipath being experienced at that station. The effect on the height, TZD, and clock estimates is complex. There is a general increase in the estimate biases with pillar width. There is however a local maximum centred on a pillar width of 0.35 m for the height and clock estimates, but this is not apparent in the TZD estimates.

3.3 Long term effects of multipath

The previous simulations investigated the impact of the multipath bias on the estimated parameters using a single day of observation. In this section, we explore the effect of multipath on continuous GPS station position time series over several years. The same default parameters were used as described in the section 3.1, unless otherwise stated. Continuous GPS times series observations were simulated over the period January 1st 2000 to December 31st 2013.

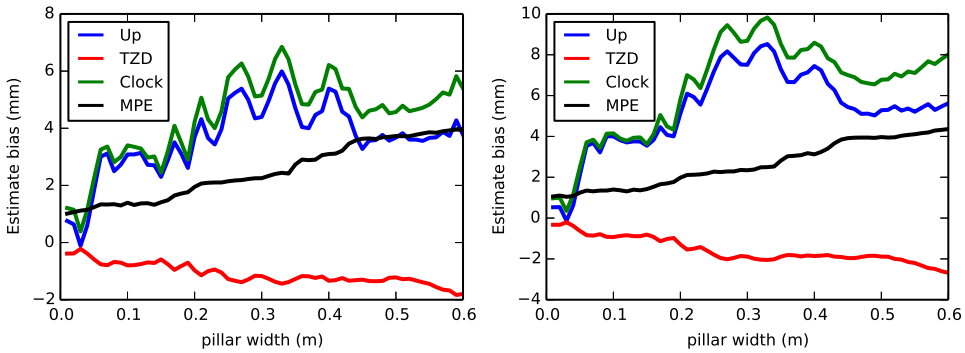

(a) Pillar Width, for h = 1.5 m, and S = 0.3 (b) Pillar Width, for h = 1.5 m, and S = 0.5

Figure 3.10: The effect of pillar width for a monument 1.5 m high, for two different values of surface roughness, (a) S = 0.3 and (b) S = 0.5.

3.3.1 Noise models

We investigated a variety of different noise models using the program 'Hector' [Bos *et al.*, 2013] to determine which best characterised the simulated time series. The best model of the time series was achieved using a power law + white noise model to fit to the first difference of the time series. Although the ARFIMA(1) and Flicker + white noise model also performed well for our simulations (see Fig: 3.11). This agreed with the findings from [Williams *et al.*, 2004] who found the noise of GPS times series data are best characterised by a combination of power law + white noise model with a spectral index ranging from 0 to 2, and clustered around 1 (flicker noise).

The following time-series simulations used the power law + white noise model to characterise the background noise of the time series to conduct statistically tests to detect other unique signals in the time series. The parameters of the power law + white noise model fits for each simulation are tabulated in Table 3.4. The key parameters are: the spectral index (k) which is equal to 2*d, the fraction f percentage of the power law component which indicates the frequency cross-over point, the standard deviation of the innovation noise σ_{innov}, and the estimated trend with it's associated uncertainty. The simulations we used had no trend added to the time series.

3.3.2 Monument height

We were interested the impact of the propagation of multipath upon continuous time series for two representative monument heights. The worst-case scenario, referred to as a low monument, used a height of h = 0.17 m. The favourable multipath environment, referred to as a high monument, used a height of h = 1.50 m. The

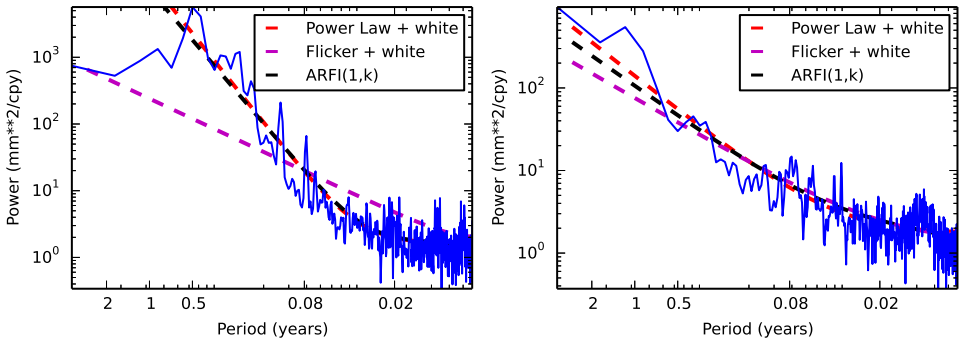

(a) Height time series, for h = 0.17 m, with the 3 best fitting noise models

(b) Height time series, for h = 1.50 m, with the 3 best fitting noise models

Figure 3.11: The height time series obtained from a multipath simulation for monument heights of h = 0.17 m and h = 1.50 m over the period January 1st 2000 to December 31st 2013. The three best fitting noise models obtained from Hector program [Bos *et al.*, 2013] are overlaid.

simulated height bias time series plots (Fig: 3.12(a) and 3.14(a)) show an irregular pattern commonly seen in GPS time series, but the two monument heights produces a distinct pattern.

Low monument time series (h = 0.17 m)

For the propagation of multipath for a low monument (h = 0.17 m), the resulting height time series has a spectral index of k = 2.6, essentially a random walk with a large amplitude in the range of 22 to 29 mm. The power spectrum of the FFT (see Fig: 3.12(b)) mainly follows the expected value for the background noise level. However there are distinct peaks in frequency, which cross the 95% significance level. The most significant peak is at the semi-annual (or 2nd draconitic), with less significant peaks at the 3rd, 4th and 8th harmonic of the draconitic.

The continuous wavelet transform (CWT) of the time series shows the same significant peak, semi-annually. Interestingly, it shows that this peak is only statistically significant from 2000 to the end of 2004. The semi-annual amplitude variation corresponds to a change in the amplitude of the height bias time series characteristics (compare Fig. 3.12(a) and Fig: 3.12(c)). There are also some transient peaks every 3 months dispersed throughout the time series. While there appears to be variation in the annual period, these are not statistically significant at the 95% level. Computing a trend, that takes into account the estimated background noise results in a large uncertainty of approximately 0.5 ± 9.8 mm/yr. This indicates that in these conditions, a bias of this size would limit the ability to estimate an accurate trend.

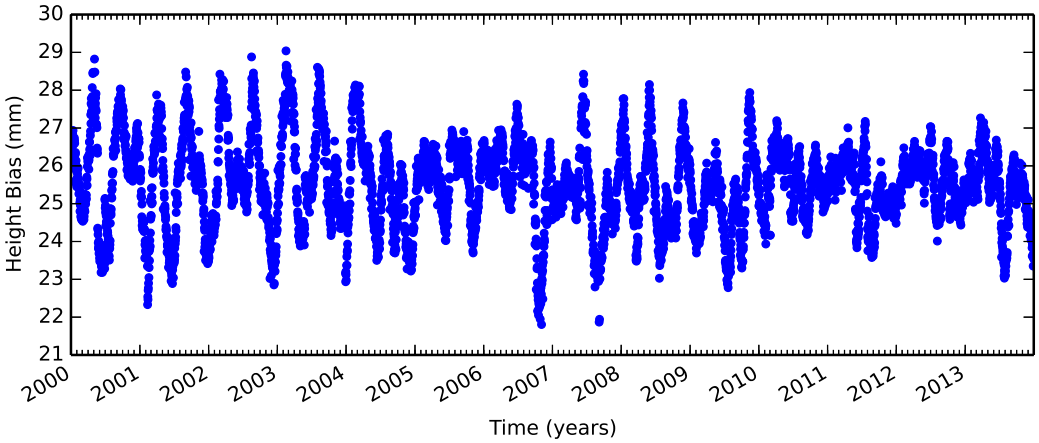

(a) Height time series, for h = 0.17 m

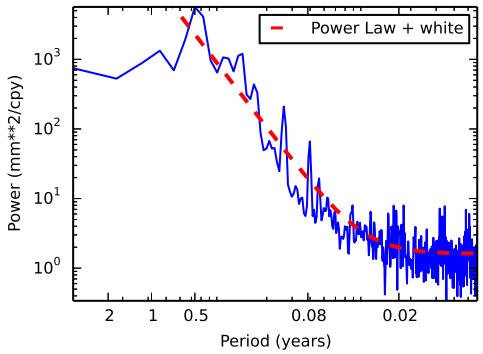

(b) FFT (left), for h = 0.17 m, where the red line shows the 95% significance level of the estimated noise model

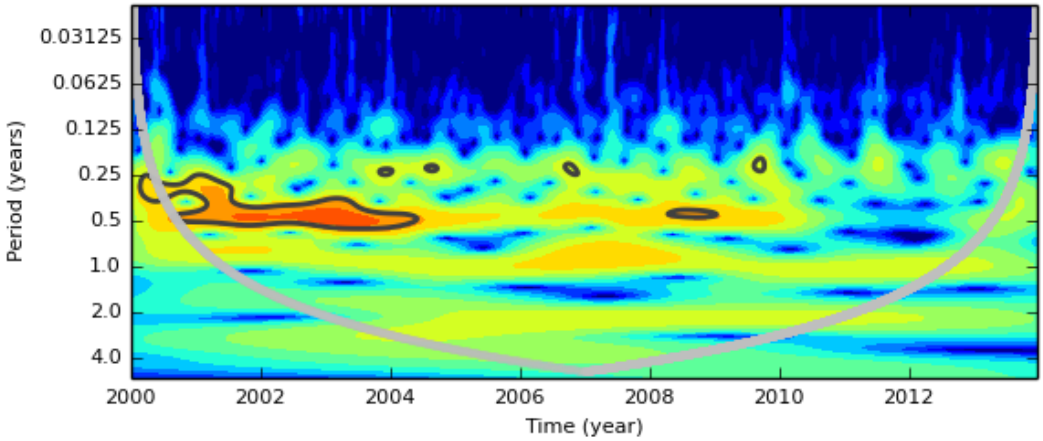

(c) Morlet CWT, for h = 0.17 m

Figure 3.12: The height time series obtained from the simulation of multipath for a monument height of h = 0.17 m, starting from January 1st 2000, to December 31st 2013.

No clock estimation (h = 0.17 m)

The same simulation was again repeated for the low monument, except that no clock estimation was included. The bias was substantially reduced to the 1 to 2 mm level, and the peaks at the semi-annual periodogram were no longer present. However, it did find a significant peak at 0.08 cpy (or approximately 30 days). The trend of the time series is no longer significantly biased, as the uncertainty is much lower at -0.05$\pm$0.03 mm/yr.

High monument time series (h= 1.50)

A visual inspection of the height time series for a multipath propagated from a higher monument (h=1.50 m, see Fig: 3.14) shows an obvious time correlation. Fitting a power law + white noise to the time series gives with a spectral index of k = 1.3. The magnitude of the bias is significantly less, compared to the low monument, ranging between -1 to 2 mm. However, the expected periodogram calculated from the estimated background noise does not give a good approximation of the observed periodogram, for the high frequency component. Nevertheless, we can still compare the characteristics of the spectral analysis with the low monument case.

Comparison with the low monument periodogram (Fig: 3.12) reveals that the higher monument has a wider band of periods which exhibit a white noise characteristic, however the higher monument has a broad 'hump' of high frequency noise, not seen in the low monument simulation. There is also a broad peak centred at approximately the 1.5 year period.

The CWT also has a continuous significant peak which starts near bi-annual period and transitions to an annual periods (see Fig. 3.14(c)). There are also significant peaks in high frequency periods corresponding to the broad hump seen in the periodogram.

3.3.3 Antenna calibration uncertainty

Antenna calibrations are not perfect and have a level of uncertainty associated with the results. Currently the IGS Antenna Working Group (AWG) requires the antenna calibrations of another institution to be repeatable at the 1 mm level on L1 over the elevation angle range 90° to 10°, and to within 2 mm at elevation angles below 10°. To simulate the effect of antenna calibration errors on the positioning results we calculated the absolute difference in results from from a calibrated GEOPP robotic antenna with results from a calibrated antenna at Geoscience Australia for the same antenna, a TRM59800.00 NONE. The results from the two different calibration facilities fall

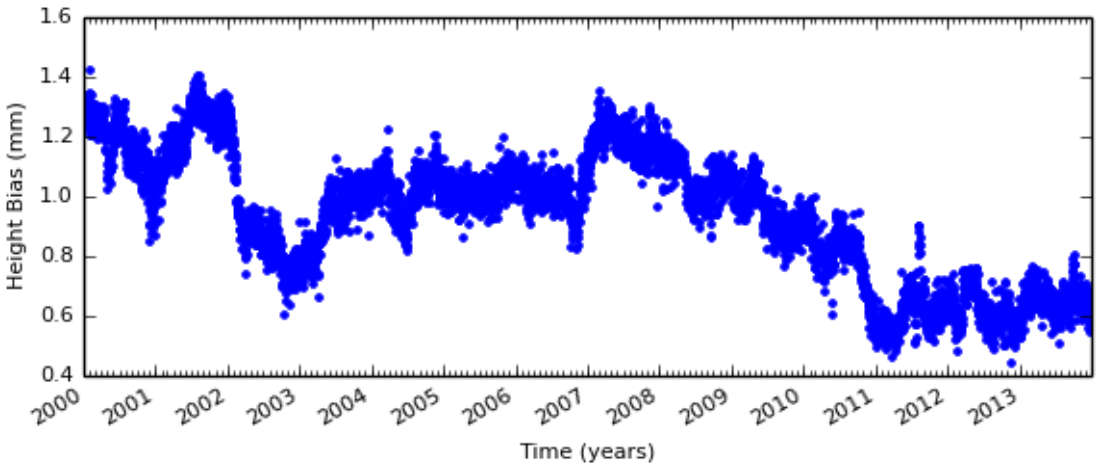

(a) Height time series, for h = 0.17 m,

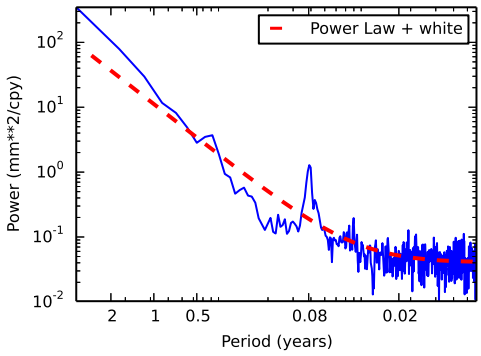

(b) FFT, for h = 0.17 m

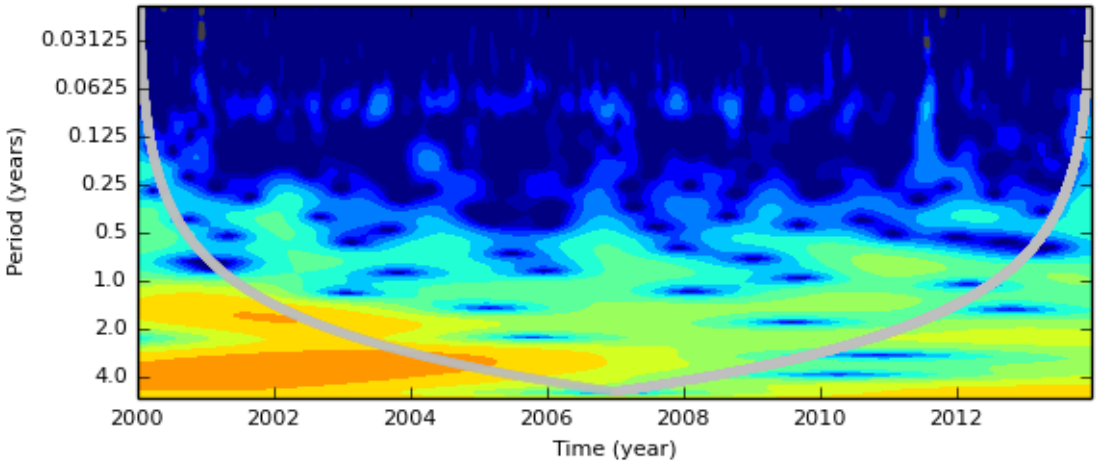

(c) Morlet CWT, for h = 0.17 m

Figure 3.13: The height time series obtained from a multipath simulation for a monument height of h = 0.17 m, with no clock estimation.

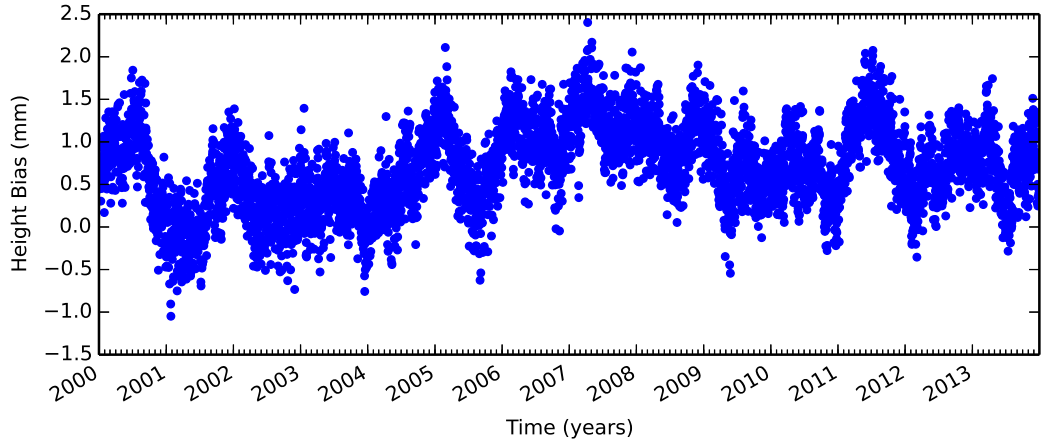

(a) Height time series. h = 1.50 m

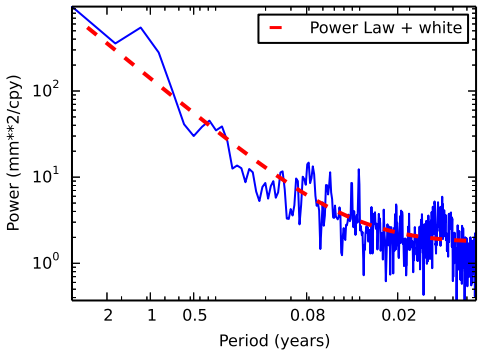

(b) FFT of height time series for h = 1.50 m

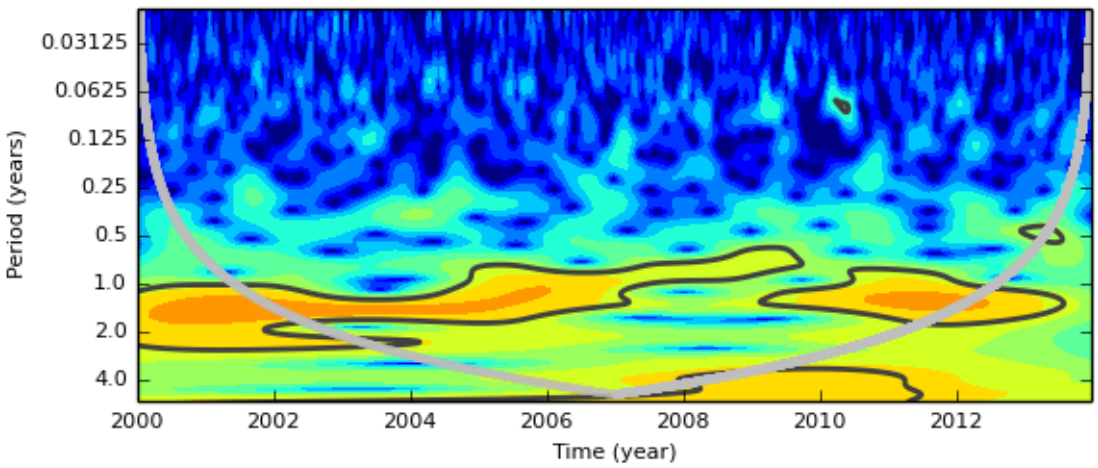

(c) Morlet CWT of height time series, h = 1.50 m

Figure 3.14: The height time series obtained from a multipath simulation for a monument height of h = 1.50 m

within the IGS AWG guidelines (see Fig. 3.15) . When the differences of the calibrations were converted to a L3 there was an amplification of the differences. However despite this amplification effect, the magnitude of the differences is still small.

The difference in the L3 calibration was used as an input bias into the ppp simulator. This produced a small impact on the time series, for example the small uncertainties of 0.06 mm/yr of the estimated trend (see the row *antenna calibration error* of Table 3.4). These tests show that the guidelines set by the IGS AWG should be sufficient to ensure that the antenna calibration differences at different facilities should have a minimal impact on the geodetic time series.

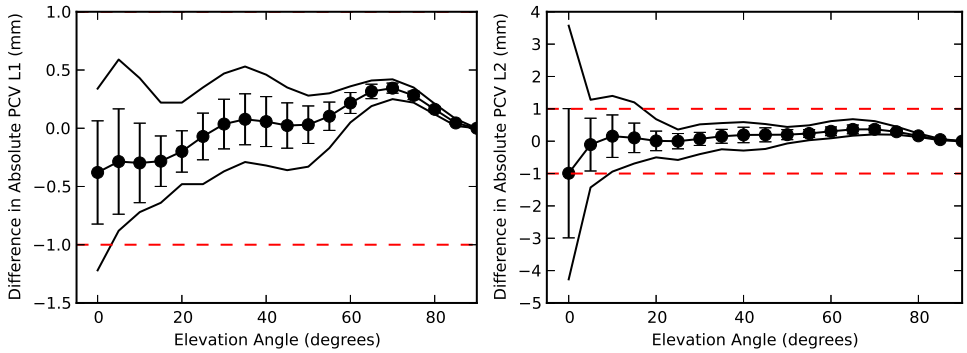

(a) Comparison on L1

(b) Comparison on L2

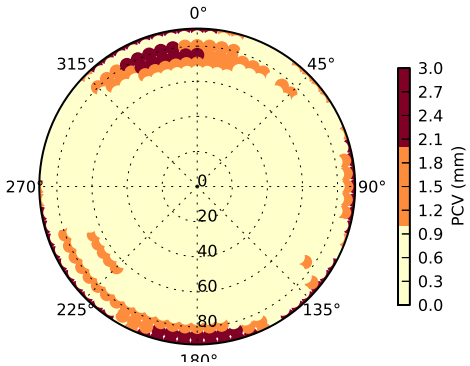

(c) Comparison on LC

Figure 3.15: Antenna calibration comparison between GEO++ results and Geoscience Australia Results on L1, L2 and the Ionosphere free linear combination LC

3.3.4 Uncalibrated radome

We also explored the impact of an uncalibrated radome on longer GPS time series, using the same methodology applied to the short GPS time series simulations in

Table 3.4: Time correlation parameters for different simulated time series. Where d is the slope of the spectra, multiply by 2 to get the equivalent spectral index k.

Simulation	d	PL%	σ_{innov}	trend mm/yr
h=0.17 m	1.34	14	0.23	-0.47 ±9.81
h=0.17 m, no clock	0.86	21	0.04	-0.05±0.03
h=1.50 m	0.50	56	0.26	0.02 ±0.02
antenna calibration error	0.66	30	0.25	0.01±0.06
radome - uncalibrated SCIT	0.77	25	0.17	0.07±0.07
radome - uncalibrated SCIS	0.88	24	0.26	0.07±0.24
radome - uncalibrated OLGA	0.82	21	0.25	0.02±0.14
radome - uncalibrated SNOW	1.11	11	0.17	0.17±0.71
radome - uncalibrated PFAN	0.97	13	0.17	0.05±0.23
h=0.17 m, lat = 0°	1.42	11	0.23	0.87±20.58
h=0.17 m, lat = -15°	1.34	16	0.24	0.04±10.08
h=0.17 m, lat = -30°	1.36	15	0.24	-0.11±13.01
h=0.17 m, lat = -45°				±
h=0.17 m, lat = -60°	1.36	12	0.22	-0.53±9.39
h=0.17 m, lat = -70°	1.42	11	0.27	-0.98±24.4
pillar width = 0.3 m, h = 1.5 m	1.07	8	0.20	-0.03±0.52
pillar width = 0.6 m, h = 1.5 m	0.99	20	0.18	-0.09±0.39
tidal, h=1.50	0.05	100	2.16	-0.03±0.03
h=0.17 m, rainfall	0.19	100	15.2	0.07±0.44
h=0.17 m, no clock, rainfall	0.23	92	0.49	-0.05±0.02

Sect. 3.2.9. In particular we looked at the impact of the SCIS, SCIT, OLGA, SNOW, and PFAN radomes, by applying the difference in the antenna calibration with and without the radome installed as the input bias into the ppp simulator. We found that an uncalibrated radomes could cause significant biases to the time series and degrade the certainty of the trend estimation. Generally the magnitude of the effect was dependent upon the radome's geometry (see Table 3.4). The radomes designed to be concentric to an antenna's mean phase centre produced the smallest effects (SCIS, SCIT and OLGA). Whereas radomes which were non-concentric radome (PFAN and SNOW) introduced a large uncertainty in to the trend estimation.

3.3.5 Variation with latitude

The main causes of site-specific errors are changes in the geometry of the satellites with respect to the antennas, where the latitude of the observing is the controlling factor. Simulations of stations at varying latitude found an increasing size of the height bias for stations approaching the poles. However, the overall noise level of the time series is fairly similar. Similar results were found when the time series data was fitted separately at each station latitude using a power law + white noise model with the spectral index ranging from 2.6 to 2.8. Although there is a significant variation with station latitude in how the power of the noise is concentrated at different frequencies. Additionally, there is also a significant variation of the power over time as shown in the CWT plots (Fig 3.16).

The variation of the noise power concentration at different frequencies is displayed for stations over the latitude range from equator to -70°S in Fig 3.16. At the equator, there are only minor significant peaks seen, located at the quarter-annual throughout the time series. Simulations at increasing southern latitudes show increasing power of the semi-annual peak over the period 2000 to 2004, and larger quarter-annual peaks from 2000 to 2008.

The estimated trend at each latitude had a large uncertainty ranging between 9 to 20 mm/yr (see Table 3.4), although there is no clear pattern in the bias of the estimated trend with latitude. Nor is there a clear relationship in the uncertainty of the trend estimate with latitude. These results demonstrate that the effect of site-specific errors on the spectral characteristics of a time series will be significantly dependent upon the station latitude and the magnitude of the bias.

3.3.6 Pillar width

We looked at the effect of two pillar widths of 0.3 m and 0.6 m upon the GPS height time series for a monument that is 1.5 m high. The surface roughness for the pillar

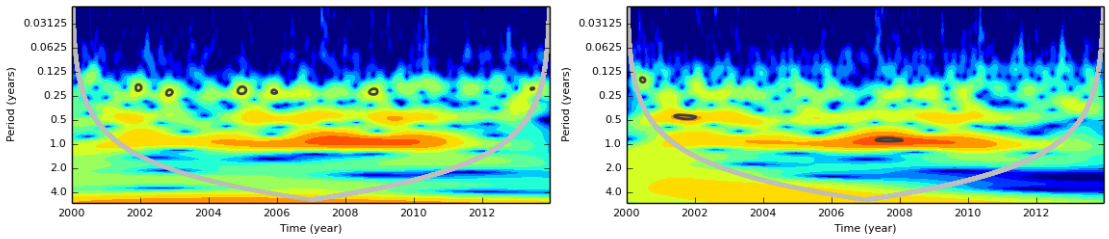

(a) latitude = 0°, latitude = -15°

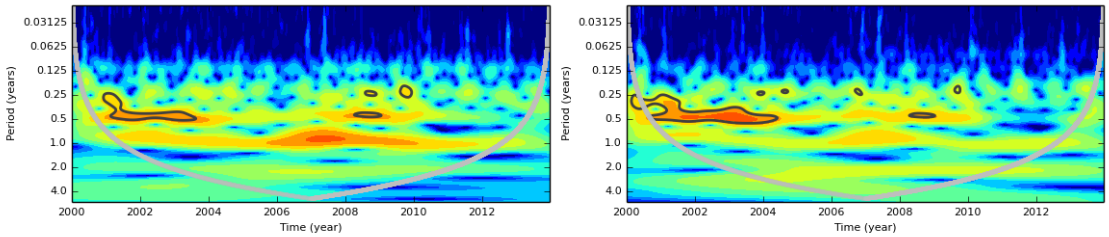

(b) latitude = -30° (left), -45° (right)

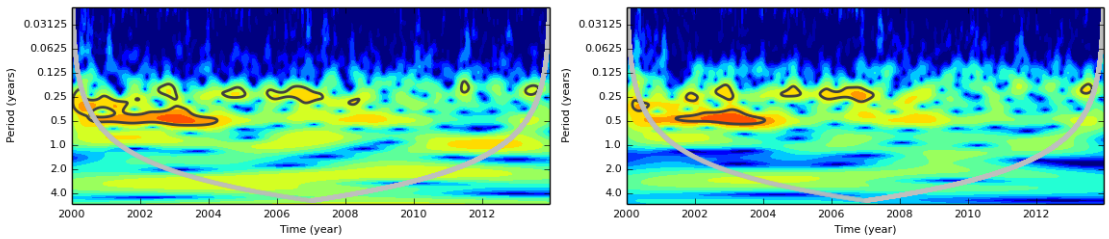

(c) latitude = -60° (left), -70° (right)

Figure 3.16: Morlet CWT of the height bias time series from 2000 to 2014 from simulations of antennas at a range of latitudes varying from 0° to -70°, at a height of 0.17m

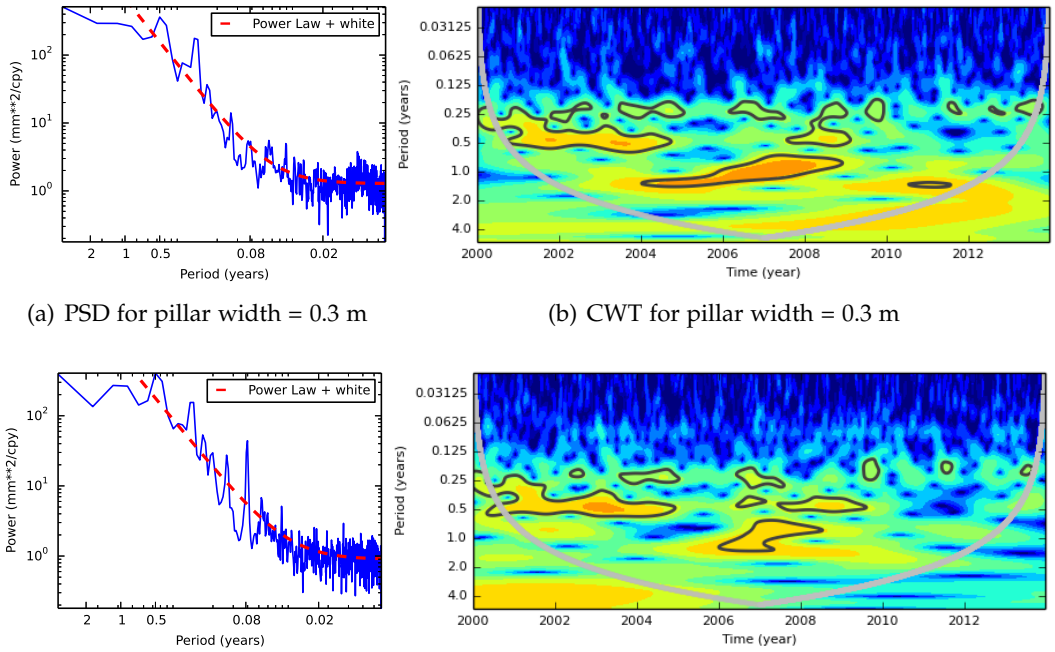

(a) PSD for pillar width = 0.3 m

(b) CWT for pillar width = 0.3 m

(c) PSD for pillar width = 0.6 m

(d) CWT for pillar width = 0.6 m

Figure 3.17: PSD and Morlet CWT of height time series using two different pillar widths of 0.3 and 0.6 m at the same monument height, h = 1.5 m, surface roughness S= 0.5.

was set to 0.5, and 0.3 for the surrounding ground. For both scenarios there are similar significant peaks at the semi-annual, occurring at the same time periods for our simulations of multipath for a low monument. The wider pillar has a large peak at 0.08 years (approximately 30 days), not present in the narrow pillar time series. The wider pillar has a higher level of time correlation present in the time series with the percentage of power law being 20% (see Table 3.4). The level of uncertainty in the height time series is similar.

3.3.7 Time variable multipath

In this section we look at the effect of time variable multipath conditions and their impact on the GPS time series.

Tide gauge

We investigated the effect of multipath effects that may occur at a GPS station mounted on a tide gauge, surrounded by water. The surrounding water surface was modelled using a smoothness (S) value of 0.8, substantially higher than that used for our simulations of antennas surrounded by ground to account for a higher proportion of the

multipath signal reflected back at the antenna. The antenna height was initially set to 1.5 m, and the height of the multipath reflector height was adjusted every 15 minutes according to the ocean tidal height, as calculated from the FES 2012 model [Carrère *et al.*, 2012]. The location of the antenna was set to that of the GPS and tide gauge station at Burnie in Tasmania (BUR2).

The height time series was fitted with a noise model of spectral index k = 0.1, which is very close to white noise. The height results were found to have close to zero estimated trend over time, with a low level of uncertainty (-0.03$\pm$0.03mm/yr). However, overall noise level for the site was much higher with a $\sigma_{innov} = 2.16$. No significant pattern was seen in the low frequency components of the CWT. There were significant variations at the high frequency scales, but these appeared to be randomly distributed and appeared frequently throughout the time series. It is likely that the high multipath reflection environment and shifting reflector geometry of a GPS stations mounted on tidal gauges causes a higher overall noise, but the time-correlated noise is significantly less.

Rainfall - low monument, h = 0.17 m

The impact of rainfall upon the multipath characteristics at the GPS station at Yarragadee (YAR2) was simulated, by correlating rain guage observations obtained from Mingenew, a township nearby. The data was obtained from Bureau of Meteorology weather station 'IDCJAC0009' (http://www.bom.gov.au/climate/data/). The rainfall records from the station were used to approximate the rainfall at YAR2. The effect of rainfall was simulated by increasing the surface roughness to 0.8 on days which rainfall was observed. When no rain was observed at the station, the surface roughness was changed back to the default value of 0.3. The monument height was set to be a similar height to that at YAR2, h= 0.17m.

Similarly to the tide gauge simulation, the results show a significant decrease in the time correlation of the height bias (see Table 3.4), compared to a simulation without the rainfall effect applied. There was a significant increase in the noise and degradation in the uncertainty of the trend.

3.4 Summary

The multipath bias is significant for geodetic observations, which use the ionosphere-free linear combination. The choice of monument height, station latitude or other processing parameters will change the multipath effects on estimated results. Antenna mounted close to a planar reflecting surface experience a multipath bias, which

changes slowly with elevation angle, which can be highly correlated with troposphere mapping function. This makes it difficult to remove (using least squares residuals) the site-specific error component of the bias caused by the local multipath environment from the bias caused by the troposphere. Simulations using higher monument heights and a low smoothness of the surrounding reflection surface show a lower net multipath bias. Therefore, it is better to mount the antenna away from potential planar reflecting surfaces as this increases the likelihood that multipath errors will average to zero. It is also important that the antenna pillar is not too wide, as widths of greater than 0.3m will negate the favourable benefits of mounting the antenna higher.

The GPS parameters applied during processing can have an impact on how well the ESM will perform. Use of a low elevation cut-off angle and estimation of clock and troposphere parameters will decrease the ability of the ESM to recover the bias due to site-specific errors. However, this can be avoided if the antenna monument heights are above 0.25m, for which the results are largely insensitive to the processing parameter set. Monuments mounted close to the ground ($<$0.25m) are sensitive to the processing parameter selected, and can have a significant impact upon the error in the derived ESM. The use of least squares residuals to model multipath effects for low monuments and high latitude ($>60^\circ$ or $< -60^\circ$) are unlikely to be successful. Furthermore, every time the site antenna is modified, a new empirical model is required to properly simulate the way multipath propagates through to the solution.

Using our short time series simulations, we were able to generalise when an ESM might perform well by using the MPE metric. However, these simulations are limited because they do no account for the influence of atmospheric biases, geophysical signals and other additional effects that may be present in addition to the site-specific multipath effect. The magnitude and the nature of these other unaccounted for effects are expected to influence how well an ESM may perform. In particular, it is likely to affect the number of observations required to obtain a reliable model. Despite these limitations, the MPE metric serves as a good indication of how the ESM might perform under different multipath conditions.

The long time series simulations highlight the importance of using a variety of time series analysis tools to properly understand the way errors are propagating into the GPS time series. Analysing the FFT and fitting a power law noise model to the time series can find a good approximation of the local multipath effects on a GPS station. However, it does not give a complete picture. The CWT is useful tool to identify any significant non-stationary behaviour in the time series that can not be detected using the FFT technique. Applying statistical significant tests, using the fitted background noise (power law + white noise), to the CWT results revealed that

they're where other significant periodic effects, which were not characterised by this noise modelling technique. The effects were found to be non-stationary for antennas mounted at low monument heights or at high latitudes.

The low monument simulation produced the spectral index of $k = 2.6$, when more white noise was added to the same scenario, the spectral index came down to $k = 2.2$. Changes in the local multipath environment over time (such as rainfall) caused a change in the spectral properties of the time series, breaking the time correlation. In the case of rainfall, we found a lower spectral index of $k=0.4$, mid way between flicker noise and white noise.

Chapter 4

Empirical modelling of site-specific errors

In the previous chapter, we found from simulations that under certain conditions the least square residuals can be used as observations to model site-specific errors. In this chapter we investigate two different techniques, which utilise the one-way post-fit ambiguity-fixed phase residuals to create an empirical model of site-specific errors. The first technique uses a stacking approach, which accumulates and then filters the phase residuals in discrete azimuth and elevation bins for each station over time. A block median is then applied to each accumulated bin to produce a model of the site-specific effects upon L3 observations. The second approach uses least squares to estimate a piece-wise linear (PWL) function for corrections to the satellite nadir dependent Phase Centre Variation (PCV) model, and then to estimate a PWL fit of the site-specific errors for each station (as it varies in azimuth and elevation).

4.1 Undifferenced phase residuals

In GAMIT, as a matter of routine, the double differenced, L3 phase residuals are converted into undifferenced residuals during the data editing stage. This approach simplifies the detection of outliers and cycle slips. To obtain residuals for site-specific modelling, we have re-run this process after the ambiguities have been fixed so that we obtained undifferenced ambiguity-fixed post-fit residuals. We obtained the undifferenced phase residuals from the MIT/ANU IGS reprocessing solution as part of the second IGS reprocessing campaign (see Chapter 2). In this chapter we have focused on the results for period starting from 2010 through to the end of 2013.

Note that there are other alternative techniques to transform double differenced residuals into undifferenced residuals e.g. [Alber *et al.*, 2000] that could be applied in other processing packages.

4.2 ESM method

A stacked model was formed by accumulating the undifferenced post-fit phase residuals over a long time periods (months to years), binning them by azimuth and elevation. This data stacking process effectively averages short-term noise effects like high order unmodelled atmospheric errors. Whenever there was a change in the antenna or radome a new model was created and the stacking was re-started.

An example of the results at each stage of the technique is shown in Fig: 4.1. Firstly, we converted the antenna model from L1 and L2 to be in terms of the ionosphere-free linear combination (see Eq. 4.1 and Fig: 4.1(a)).

$$\delta\phi_L^{L3} \approx 2.5457 * \delta\phi_L(\lambda_{L1}) - 1.545 * \delta\phi_L(\lambda_{L2}) \tag{4.1}$$

where the subscript L denotes a unit of length, λ_{L1} and λ_{L2} are the wavelength for L1 and L2 respectively. Then the L3 phase residuals of the complete time-series of processed observations were stacked into individual models for periods that contained continuous operation of the same antenna. They were placed onto a 0.5° grid and a block median was applied (see Fig: 4.1(b)). Our implementation of the model takes the L1 and L2 antenna PCV model and bi-linearly interpolates this onto a grid of the same resolution as the block median (0.5°). The block median values from the stacked phase residuals are then added to the interpolated antenna model (see Eq. 4.2 and Eq. 4.3).

$$L1\_ESM_{az,el} = L1PCV_{az,el} + e_{az,el} \tag{4.2}$$

$$L2\_ESM_{az,el} = L2PCV_{az,el} + e_{az,el} \tag{4.3}$$

where e was the block median L3 phase residual (mm) at each azimuth az, and elevationel, L1PCV and L2PCV is the antenna PCV model for the L1 and L2 GPS frequencies respectively, interpolated onto the finer grid point for the each azimuth and elevation grid used in the ESM.
Adding an L3 residual to the L1 and L2 PCV model is equivalent to converting the antenna model to L3, and then adding the residuals. For instance if we take the L3 phase residual and substituted Eq. 4.2 and 4.3 into Eq. 4.1 :

$$L3\_ESM_{az,el} = 2.5457 * L1\_ESM_{az,el} - 1.5457 * L2\_ESM_{az,el} \tag{4.4}$$

This was then published into a modified ANTEX file at 0.5° intervals for azimuth and elevation. Subsequent processing can then be undertaken using the ESM by specifying the correct antenna type and serial number installed on the station at the

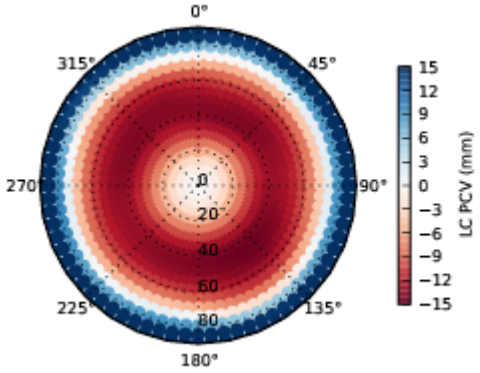

(a) L3 antenna phase variation model for the IGS station MOBS (ASH701945C_M NONE)

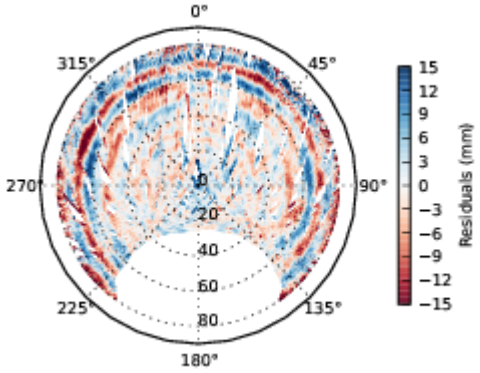

(b) L3 phase residuals accumulated during 2012 from the IGS station MOBS

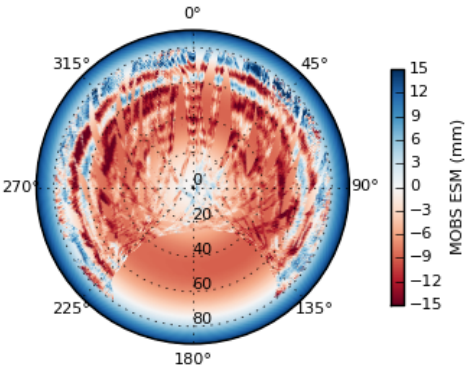

(c) L3 Empirical site model ((a) + (b)) ready to be published in ANTEX format for re-processing

Figure 4.1: Illustrative example showing the process to create an ESM (b) and publishing for re-processing (c).

time. In the example shown here, when the grids do not contain any phase residuals, no interpolation was applied, and nothing was added to the original antenna model. This approach should be appropriate for historic data sets, where if an observation is missing at a particular location in the sky, it is unlikely to need to have a correction applied. However the technique can be easily extended to include an interpolation to account for future data sets where satellites may appear in different parts of the sky, than have been previously been observed.

4.2.1 Optimising model resolution

The number of parameters used to form an empirical model is an important consideration. Too few parameters will result in a model that will fail to characterise the site-specific errors experienced at a station, leading to model with little use. Whereas too many parameters will result in a model which may fit a particular data set very well, but will not generalise well to other data sets (for instance future observations). Finding the right resolution and ensuring enough data has been accumulated to create a robust empirical site model are key factors that need to be taken into consideration.

We tested for over-fitting or under-fitting of the ESM by randomly selecting 70% of the residuals available for each station to calculate a model from. This data set is referred to as the *training* data set. The remaining 30% of the available data was used to test how well the model performed when applied to data sets not used to create the model, or in other words how well the model generalised. This data set is referred to as the *test* data set. In circumstances where there was a significant deterioration in the model's performance using the test data set, then the model was deemed to be over-fitted, then this required the removal of higher order parameters, or the addition of more observations.

As a cautionary note, we need to keep in mind that while we can test how well the model will fit the phase residuals, this does not guarantee that the model is an accurate representation of the site-specific error experienced at the station. For instance it was found from earlier simulations that there was small subset of scenarios where the least squares residuals are not guaranteed to always be an accurate representative of site-specific errors (e.g. h = 0.17).

4.2.2 Grid resolution

Firstly we investigated a range of resolutions to determine the most appropriate to use to model multipath using L3 phase residuals. The antenna's PCV models are provided at 5° intervals, which is suitable resolution for antenna PCV. Multipath

errors however can change rapidly with azimuth and elevation angle, especially for high monuments. If a 5° resolution was used to model multipath effect of a 2.00m high monument, the model would clearly be ineffective (see Fig: 4.2(a)).

Simulation test

To determine the best grid-sampling interval to characterise multipath, we simulated the multipath error as it varied with elevation angle (from 0° to 90°) for monument heights varying from 0.01m to 2.00m (at 0.01m intervals). We tested the effects of using grid intervals of 5°, 2°, 1°, 0.5°, and 0.1°. A continuous function approximation was obtained by simulating the multipath bias at very high resolutions (0.001°) to determine the misfit of the different grid intervals. Each grid spacing was tested by measuring the rms difference between a linear interpolation onto the higher resolution at each simulated monument height (see Fig. 4.2(b)).

Using this method we found that the most appropriate grid resolution was 0.5°. As the monument height increased, the L3 multipath bias becomes increasingly complex in its variation with elevation angle, thus requiring a higher resolution to effectively model the signal. The grid resolutions of 5° and 2° were too coarse of a resolution to represent multipath errors for monument heights greater than 0.5m. A 1° resolution performed well up to a monument height of 1.0m, but at monument heights above 1.5m the errors became significant. At the 0.5° resolution the RMS misfit was approximately 0.2mm for the highest monument simulated. This is well within the expected measurement noise. The 0.1° resolution has negligible errors, however they would probably have resulted in an over-fitting problem.

Validation of grid resolution

We validated that a 0.5° resolution grid was the optimum by testing the effect of using different grid spacings on observed L3 phase residuals. Using all of the residuals for the stations processed in 2013 (456 different stations); the residuals were split into a training set (used to create the ESM at different resolutions) and a testing data set. An assessment was then made on how well the model performed by computing the mean absolute error (MAE) of the model when applied to the test data set:

$$MAE = abs(\frac{1}{2 * n} \sum (f_{az,el} - y_{az,el})^2) \tag{4.5}$$

where, $f_{az,el}$ was the modelled value for a point at a given azimuth (az) and elevation (el), and y was the observed value at the given azimuth and elevation, n was the number of observations. This was carried out for each of the different grid resolu-

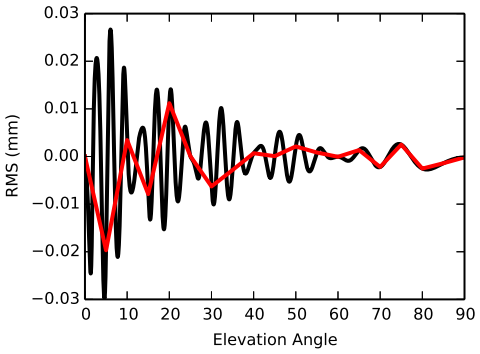

(a) The black line shows the theoretical L3 multipath for a monument height of 2.00m, the red line is the result of modelling the multipath error on a 5°grid.

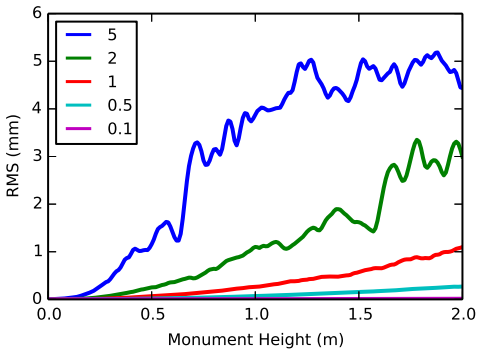

(b) RMS error of a multipath model for resolutions of Grid intervals of 5°,2°,1°,0.5°, and 0.1°

Figure 4.2: (a): Multipath bias for a monument height of 2.00m sampled at 0.001° (black line) and 5° (red line). (b): Error in grid intervals of 5°,2°,1°,0.5°, and 0.1° for the simulated L3 Multipath bias for a range monument heights (0.01 to 2.0m) compared to a higher resolution of 0.001°

tions of 0.1°, 0.5°, 1°, 2°, and 5°. The grid resolution with the smallest absolute mean error was then recorded as the optimum choice.

The majority of stations had a best fit with a 0.5° resolution (see Fig. 4.3). However there were also a large number of stations for which we determined the best fit resolution of 0.1°. One can expect that if we increased the number of observations used to compute the model that the number of stations falling into a higher resolution would increase. However the difference in the MAE for a 0.1° and 0.5° grid is small, consequently there was not much accuracy to be gained by using the higher resolution. Therefore a grid resolution of 0.5° was confirmed to be the most appropriate grid spacing to use for site-specific models.

The majority of IGS stations are now installed on pillars approximately 2.0m above the ground, situated in fields away from nearby obstructions in accordance to IGS site guidelines. Therefore for these stations a grid resolution of 0.5° is the best choice. However for stations which are installed in less ideal environment, such as on the corner of a roof top, or ext to reflective buildings may require a finer grid resolution.

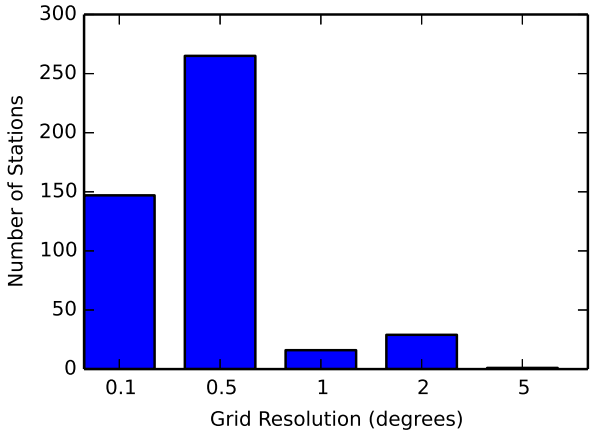

Figure 4.3: The number of stations which have an optimum grid resolution of 5°,2°, 1°, 0.5° and 0.1° based upon the grid spacing which produced the smallest MAE metric.

4.2.3 Integration interval

There is a relationship between the number of observations required to obtain a reliable model and the grid resolution used. This is illustrated in Figure 4.4 where we show the effect of using a resolution of 2° and 0.5° upon the length of time taken for the model to converge. At the coarser 2° resolution, the model quickly converged to the minimum mean absolute error (MAE) of 6.5 mm after a relatively short period (<50 days). At the higher 0.5° resolution, we found that the model reaches a lower minimum of approximately 6.0 mm after a considerably longer time. Despite this, both models reached a MAE of 6.5 mm in a similar amount of time, in addition the higher resolution model significantly decreased to a lower MAE. Consequently there was no advantage gained from using a coarser model to represent a complex multipath signal.

Using a grid resolution of 0.5° we then calculated the expected observation time to obtain a reliable model at this resolution. We tested the time needed to accumulate sufficient phase residuals to obtain an accurate ESM by computing the mean absolute error as a function of number of days for stacked residuals over the period ranging from 2010 to the end of 2013. We selected only those stations, which did not have any change of antenna or radome and therefore only required one model. From this set of stations, a subset of 100 stations was selected to test the integration interval. The stacking interval was started with daily increments of accumulating the phase residuals for the first 21 days. This was then increased to increments of 2 days up to the first 90 days observation, and then by increments of 15 days for the remaining

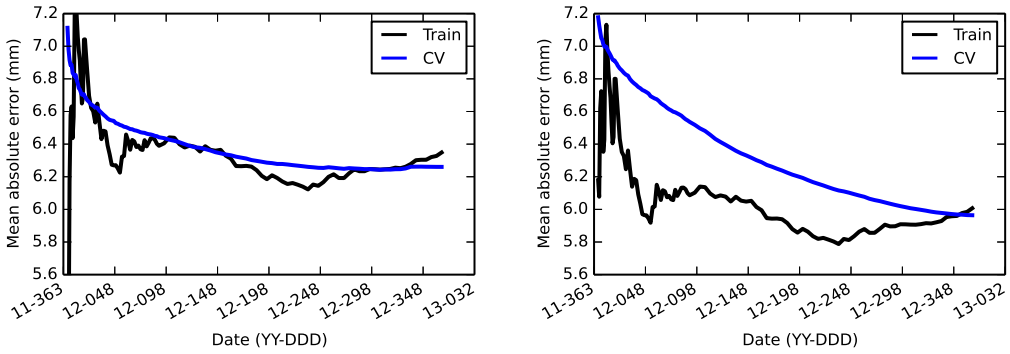

(a) HOB2 2

(b) HOB2 0.5

Figure 4.4: The computed mean absolute error as more phase residuals are accumulated with time for a block median ESM with a grid resolution of (a) 2° (b) 0.5°.

observations. A majority of stations showed a convergence after 120 days of residuals had been stacked.

4.3 Satellite specific-errors

The existence of elevation-dependent GPS satellite antenna phase centre variations was highlighted by [Rothacher, 2001], amongst others, and was first estimated by [Schmid and Rothacher, 2003]. One of the major problems they reportedly faced was the high correlation between several parameters, namely clock biases, tropospheric delays, as well as phase centre offsets and variation of both the receiver and satellite antennas. There is in fact a one-to-one relationship between the errors in the nadir dependent satellite errors, and the elevation dependent receiver antenna errors [Rothacher, 2001]. This implies that a site-specific approach cannot be achieved without first considering satellite specific effects.

For instance the nadir angle $z^{'}$ at the satellite is related to the zenith angle z for the receiver at the ground by:

$$sin(z^{'}) = \frac{R}{r} sin(z) \tag{4.6}$$

where R was the Earth's radius and r the geocentric distance of the satellite (see Fig 4.5). While the zenith angle z at the receiver ranges from 0° to 90°, the corresponding nadir angle $z^{'}$ as seen from the satellite only varies between 0° and approximately 14.28°. The maximum nadir angle observed by a station with a cut-off

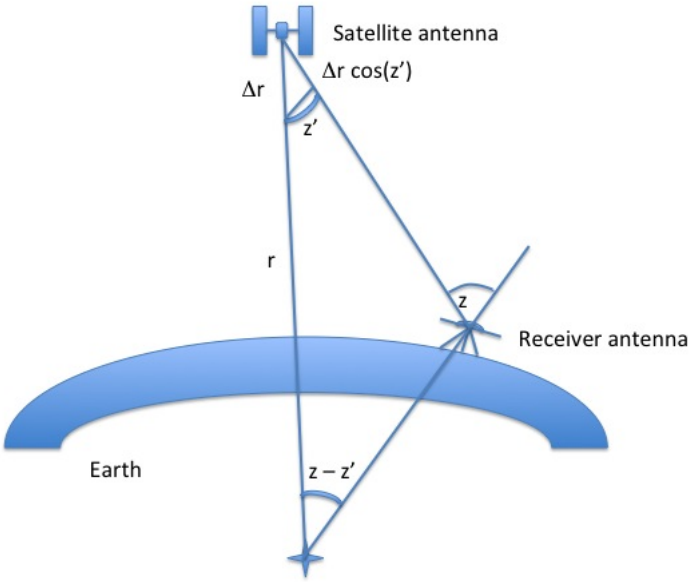

Figure 4.5: Relationship between satellite and receiver antenna phase centre variations.(Adapted from [Schmid and Rothacher, 2003])

elevation angle of 10° can be calculated from:

$$z'_{max} = arcsin(\frac{R_{max}}{r_{min}}.sin(z_{max})) \tag{4.7}$$

If we assume an R_{max} of approximately 6387 km, and for satellites close to the perigee in an orbit with comparatively high eccentricity ($e_{max} \approx 0.025$). This lead to a nadir angle that was always be below 14.06°.

With the aid of the nadir angle z' and elevation-dependent phase centre pattern $\phi(z)$ of the receiver antenna was interpreted as a phase centre pattern $\phi'(z')$ of the satellite antenna, and vice versa, with

$$\phi'(z') = \phi(z) \tag{4.8}$$

A change $\delta\phi(z)$ of the receiver antenna pattern affected the satellite antenna pattern with reversed sign.

$$\delta'\phi(z') = -\delta\phi(z) \tag{4.9}$$

Another correlation exists between phase centre offsets and variations. In the satellite case a change of δr of the antenna phase centre offset in the nadir direction

can be interpreted as a cosine-dependent change of the phase pattern (see Fig: 4.6).

$$\delta^{'}\phi(z^{'}) = -\delta r.(1 - cos(z^{'})) \tag{4.10}$$

Therefore the choice of PCO is arbitrary. In other words, it was impossible to estimate for the PCO and PCV simultaneously.

Besides the elevation-dependent phase centre variations, azimuth-dependent

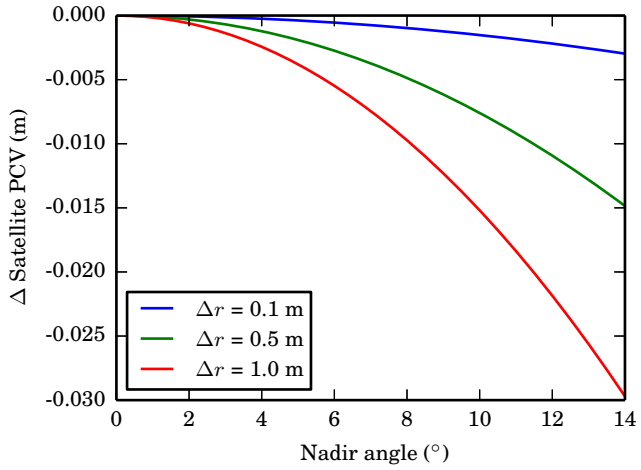

Figure 4.6: Change Δr of the phase centre offset interpreted as a change of $\delta\phi^{'}(z^{'})$ (nadir dependent PCV) of the phase pattern.

variations have been reported. In order to study these, the attitude of the satellite would also have to be taken into account. We have restricted our investigation to elevation dependent variations only.

4.4 Nadir approach

In this section we detail a refinement of the ESM modelling approach detailed earlier in Sec 4.2. This refinement is a two stage estimation process, which first takes into account satellite specific errors from the post-fit ambiguity fixed residuals, then estimates the site-specific errors. We refer to this as the nadir modelling technique.

If we assume atmospheric errors average out over time, then the undifferenced post-fit, ambiguity fixed L3 residuals are a function of the site-specific errors, and mismodelled satellite antenna model given by Eq. 4.11.

$$L3_{residual}(az, el) = SITE_{error}(az, el) + SATPCV_{error}(nadir) \tag{4.11}$$

The first stage of the nadir technique estimates a correction to the nadir PCV model by using a least squares fit of a piece-wise linear (PWL) model to the L3 residuals for each satellite. For each station the residuals were split into daily blocks. Any residuals greater than 100mm were automatically excluded, along with any outliers greater than 5 σ. Each daily block of phase residuals was weighted according to it's elevation dependent weighting function (see eq. 2.13) determined for that day.

The residuals were then stacked into normal equations by satellite for each station. Once the normal equations for the satellite corrections had been computed for each station, they were then combined and inverted to obtain an estimation of the satellite nadir PCV corrections for each satellite observed at a grid resolution of 0.2° (to stay consistent with the current IGS satellite models).

The second stage of the nadir technique was to perform another adjustment to estimate the azimuth and elevation dependent site models on a station-by-station basis. The satellite nadir PCV corrections were introduced as apriori values, and were tightly constrained. Creating an azimuth and elevation dependent site-model, requires the inversion of normal equation (NEQ) that would take an impractical amount of time to solve. For instance, a nadir model estimated over a four year period would need to account for approximately 40 satellite models, with a grid resolution of 0.2 °, this is a total of 141 * 40 parameters. Then to include an azimuth and elevation station model at 0.5° results in a total of 141 * 40 + 181 * 721 = 135960 parameters. Inverting a 135,960 x 135,960 matrix requires an impractical amount of computing resources to complete. To resolve this we isolated the PWL fit for each station into azimuth slices. For 0.5° resolution, we solved for 721 PWL fits for each azimuth slice. The PWL fits for each slice were then later combined to obtain a complete azimuth and elevation dependent station model. The estimates from the nadir adjustment technique were then added to there respective satellite model, or there respective station antenna model.

4.4.1 Distribution of observations

Looking at the distribution of observations with respect to nadir angle provides some insight into the issue with estimating for nadir PCV corrections (see Fig: 4.7). In general the number of observations increased as the nadir angle increased from 0° to 14°. Notably the number of observations decreased significantly for nadir angles above 13.6°. This corresponded to low elevation angle observations at the station, and are often below the 10° elevation cut-off angle.

The uncertainty of the corrections to the satellite nadir PCV appeared to follow a $\sqrt{n}$ relationship. However there was an increase in uncertainty for nadir angles

between 11° to 14°. This corresponds to lower elevation angle observations at the station, which also have a lower weighting. We viewed the very small uncertainty in the mid nadir angle regions between 2° to 10° as being overly optimistic. One possible reason for the unrealistic uncertainties could be due to the lack of any time-correlation effects included in the weighting of the observations.

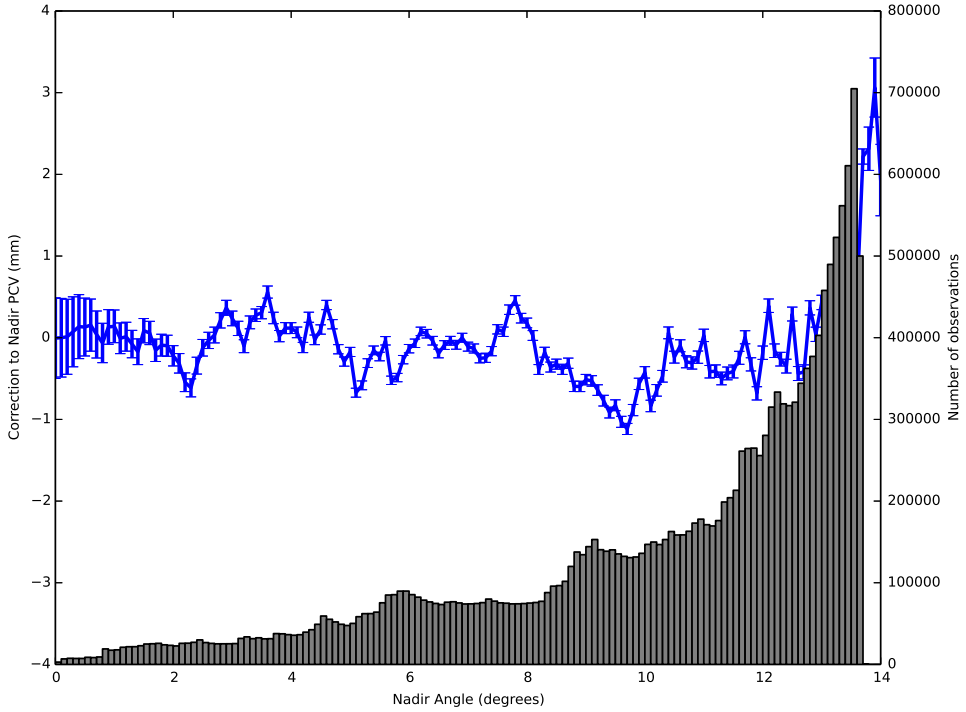

Figure 4.7: The calculated adjustment to the NADIR PCV model and distribution of observations with nadir angles for SVN G062. The results were obtained from a global network of 85 stations using the post-fit residuals for 2012 only, with a 10 mm constraint on the Satellite Nadir PCV.

Repeatability of nadir estimates

To assess the sensitivity of the nadir modelling approach to the ground station network we compared the estimates obtained from 5 global networks of approximately 80 stations each with a combined solution using all of the stations.

Comparing the results from 5 different global networks tested the dependence of the network on the estimates of the nadir PCV corrections. The station selection for each network was based upon the optimum network configuration of 5 global networks on 2012 DoY 100 (see Fig: 2.1). The phase residuals from these sites were stacked together for a 4 year period and then each network estimated there own cor-

rections to the satellite nadir PCV.

The results from the different networks closely agreed for nadir angles between 4° and 13.8° (see Fig. 4.8). For nadir angles less than 4°, there was an increased variability, due to the lower number of observations in these nadir angle bins. To reduce the variability or uncertainty in the estimates, particularly between 0° and 4°, the number of observations needs to be increased. Stacking phase residuals over a longer time span, or alternatively adding more sites into the adjustment can achieve this.

We took the approach of adding all of the stations processed in the solution into

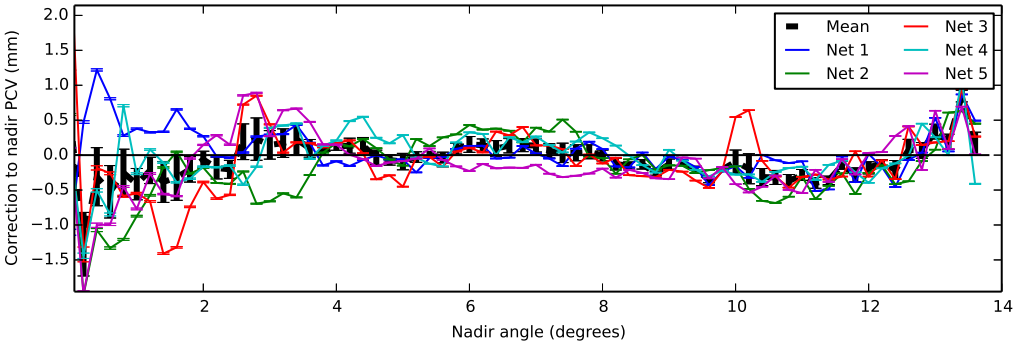

(a) SVN 62 Nadir angle correction estimates from 5 different networks over a 4 year period

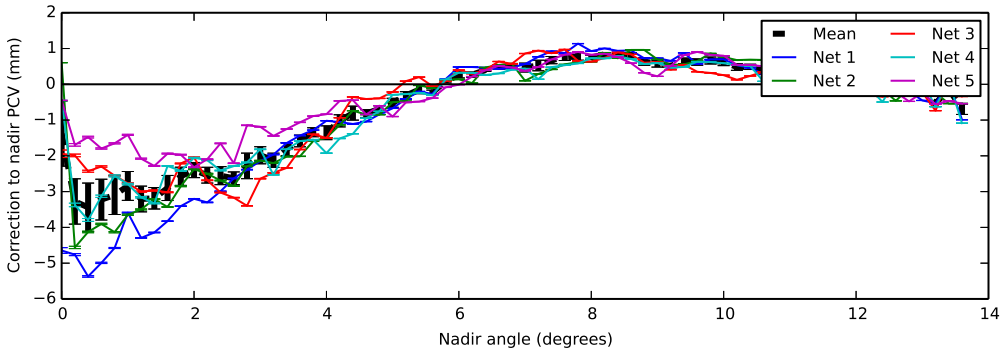

(b) SVN 56 Nadir angle correction estimates from 5 different networks over a 4 year period

Figure 4.8: Comparison of estimates for nadir angle corrections obtained from five different global networks, using residuals stacked over 4 years from 2010 to 2013.The black dashed line is the mean solution for all of the networks, and the error bars represent 1 standard deviation from the mean.

one adjustment of the satellite nadir PCV corrections. In order to let the NEQ be of an invertible size, we reduced the number of station parameters to 1 per site, and this was constrained to 0. In effect, this was the same as doing an adjustment without

including the station model. Using a large network produces reliable and consistent results, especially when we compare the solution to the mean of the 5 global networks. The results from all of the stations are shown in Fig: 4.9 as network 6. For all of the estimates for the nadir PCV corrections the larger network closely follows the mean of all of the 5 global networks.

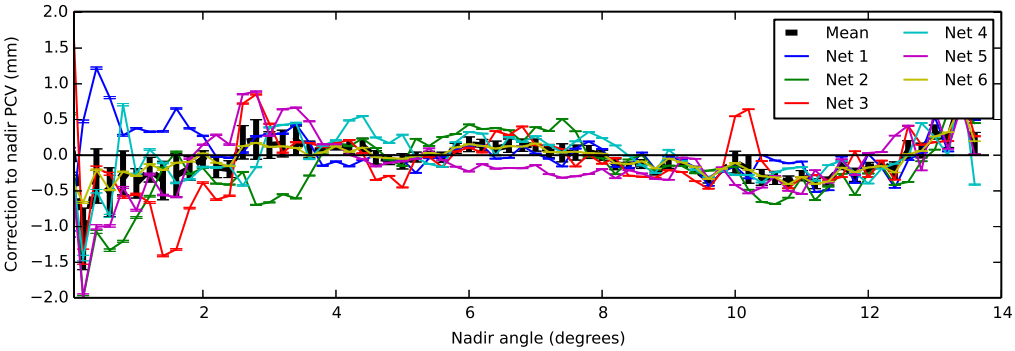

(a) SVN 62 Nadir angle correction estimates from 5 different networks over a 4 year period

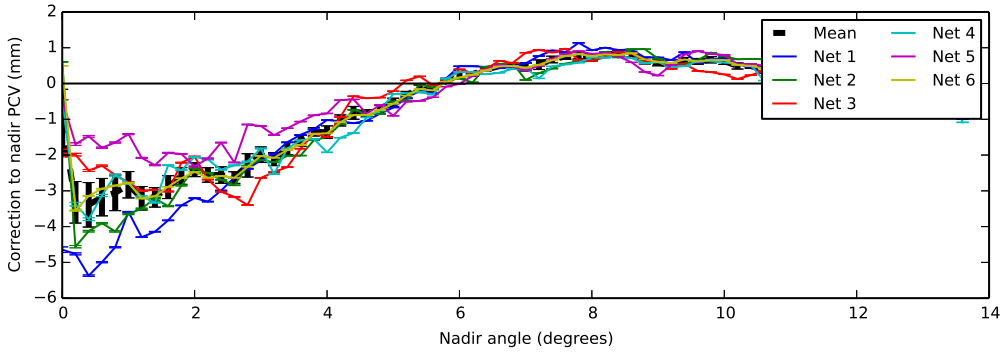

(b) SVN 56 Nadir angle correction estimates from 5 different networks over a 4 year period

Figure 4.9: Comparison of estimates for nadir angle corrections obtained from five different global networks consisting of 80 stations in each network, using residuals stacked over 4 years from 2010 to 2013. Network 6 is a larger network comprised of over 500 station phase residuals.

Classification of satellite blocks

The space segment of the GPS system consists of six different satellite blocks 4.1. However this classification scheme does not distinguish between the conventional Block IIR satellites and the modernized representatives of the same block as regards to the space vehicle number (SVN). For this reason the conventional Block IIR satellites are subdivided into two subgroups called Block IIR-A and Block IIR-B. The

Table 4.1: Official satellite block designations [Navstar, 2004], space vehicle number (SVNs) and manufacturers

Satellite block	SVNs	Manufacturer
Block I	1-11	Rockwell International
Block II	13-21	Rockwell International
Block IIA	22-40	Rockwell International
Block IIR/IIR-M	41-61	Lockheed Martin
Block IIF	62-73	Boeing
Prototype	12	Rockwell International

Table 4.2: IGS designations for the Block IIR satellites and the corresponding SVNs [Dorsey *et al.*, 2006]

Satellite antenna type	SVNs
Block IIR-A	41,43-46,51,54,56
Block IIR-B	47,59-61
Block IIR-M	48-50,52-53,55,57-58
Unsuccessful launch	42

classification of the three different subgroups of Block IIR is given in 4.2. For the remaining satellite blocks the official designations are used.

The nadir PCV corrections are similar for all of the satellites within each block type (see Fig. 4.11). Interestingly, there was an intriguing pattern to the nadir PCV corrections, where the majority of the corrections they pass through 0 at 5° and 12°. We are currently unaware of any reason why this might be occurring.

The satellite blocks IIF and IIR-B have a well resolved satellite nadir PCV that do not have a significant correction that needs to be applied, and the satellites within each of these block behave consistently with each other. There are some discrepancies near 0°, however this was more likely to be due to the lower number of observations available in these bins, than any physical difference in antenna characteristics.

Of all the nadir corrections estimated, satellite SVN 56 (a Block IIR-A satellite see Fig: 4.11(b)) had the most significant correction from it's respective block mean .

4.4.2 Post-fit residuals

Computing the ratio of the post-fit residuals with the pre-fit residuals for all of the satellite corrections estimated, indicated a very small level of improvement, as the ratio was very close to 1.00. Inspection of the post-fit/pre-fit ratio for each satellite, revealed a general underlying pattern, where the ratio was the smallest for nadir

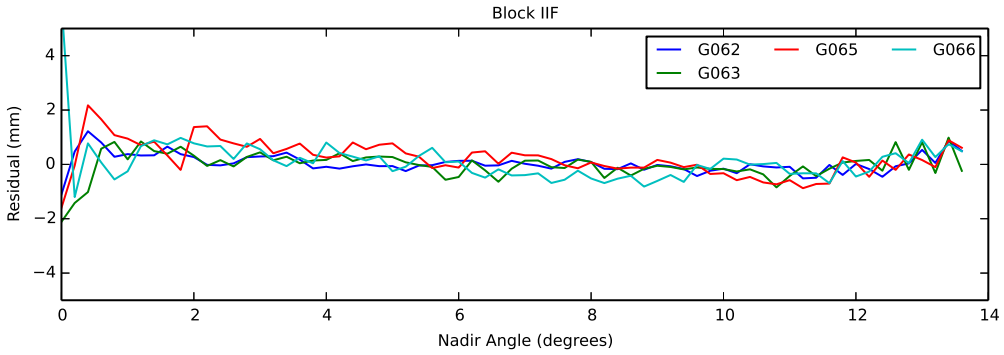

(a) Nadir PCV Correction estimates for Block IIF satellites

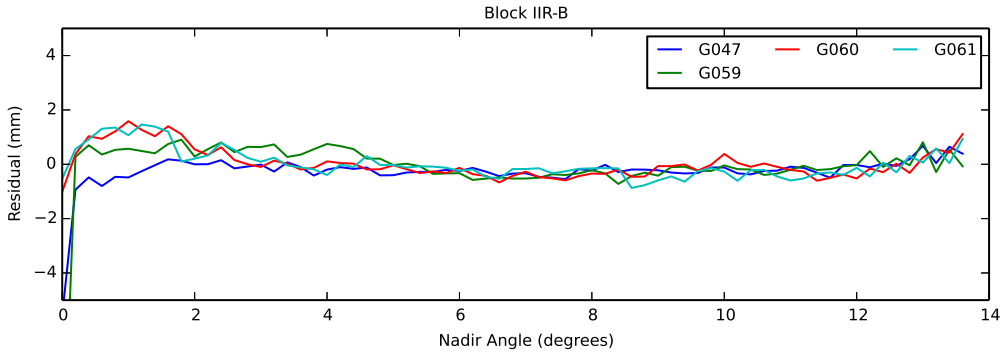

(b) Nadir PCV Correction estimates for Block IIR-B satellites

Figure 4.10: Estimates of Nadir PCV corrections without consistent satellite results, obtained from and PWL adjustment of phase residuals from 2010 to 2013.

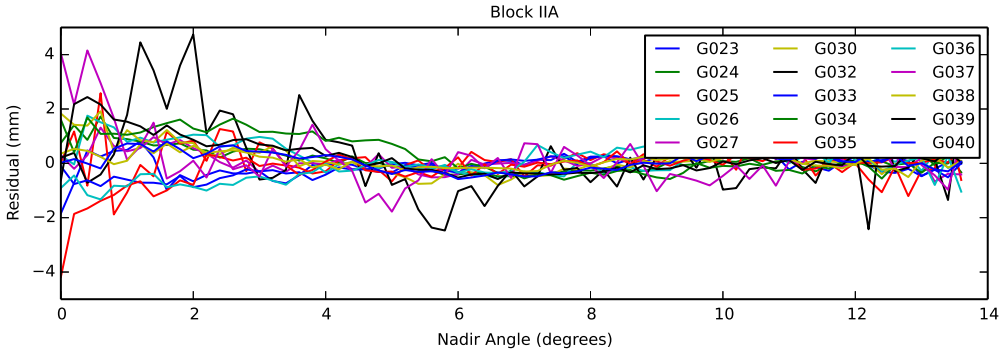

(a) Nadir PCV Correction estimates for Block IIA satellites

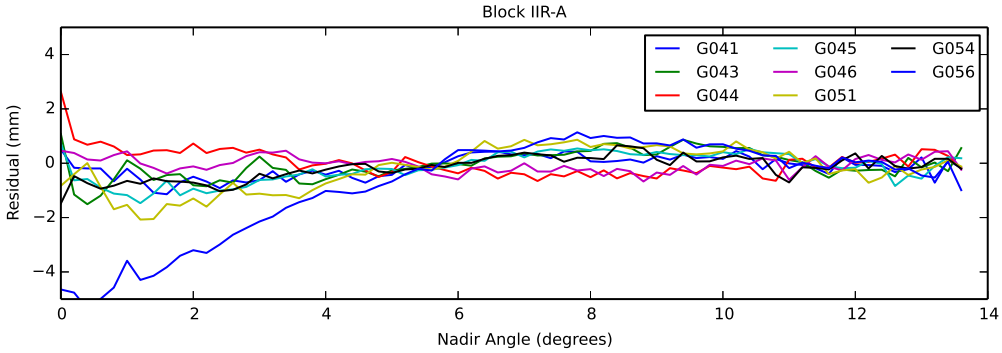

(b) Nadir PCV Correction estimates for Block IIR-A satellites

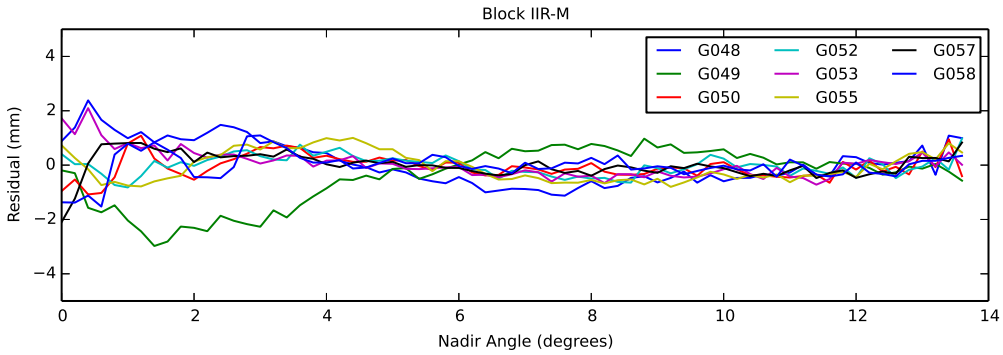

(c) Nadir PCV Correction estimates for Block IIR-M satellites

Figure 4.11: Estimates of Nadir PCV corrections with significant individual satellite departures from the block mean, obtained from and PWL adjustment of phase residuals from 2010 to 2013.

angles between 0° and 5° (see Fig 4.12). This corresponds to high elevation angles at the observing stations, which will have the highest weighting in the solution. Therefore these adjustments are more likely to have an impact upon the position estimates. However in some case there was little indication of an improvement in the post-fit/pre-fit residual. It is therefore likely that these satellite corrections were not significant, and did not need to be applied.

We then computed the post-fit residuals for the station models. The overall post-fit/pre-fit ratio was generally around 0.95 for the majority of stations. Again indicating there was not a significant level of improvement. However the ratio of post-fit/prefit computed at each station and for each individual grid in azimuth and elevation indicates that there are substantial regions within each model where there appears to have been significant improvement from application of the model. In addition the post-fit/pre-fit residuals for the elevation only PWL model (see Fig: 4.13(a)) shows there was a significant improvement.

4.4.3 Comparison of stacking and adjustment site models

Not adjusting for the nadir site PCV corrections can lead to a bias of over 1 mm in the Empirical Site Model. A visual comparison of the azimuth and zenith models with and without nadir corrections does not show an obvious difference between the two (Compare Fig. 4.14(a) and Fig. 4.14(b)). However when a difference is computed between the two models, there are distinct differences between the two techniques (see Fig: 4.14(c)). These differences are at the mm level, and they appear in bands, which follow distinct satellite tracks.

4.5 Summary

An advantage of the ESM approach is the ability to produce a site model for a particular station from historical data, which can then be made available in a common format (*e.g. a modified ANTEX file*) simplifying the implementation of the ESM. If such ESMs accurately model site-specific systematic error and then universally applied with success, they allow the retrospective recovery of site-specific errors as well to correct antenna mis-modelling errors for antennas and radome, which may be unavailable for conventional calibration techniques. This makes it a potentially attractive technique to be applied to long-term time series analysis, especially where small geophysical signals of comparable magnitude are being investigated.

A resolution of 0.5° is the most appropriate resolution to characterise multipath in site-specific models. Approximately a stack of 120 days is required to obtain a

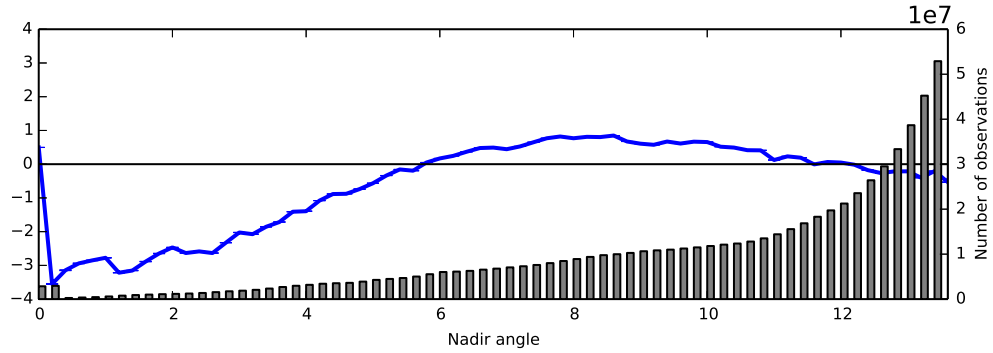

(a) Nadir PCV Correction estimates for SVN56

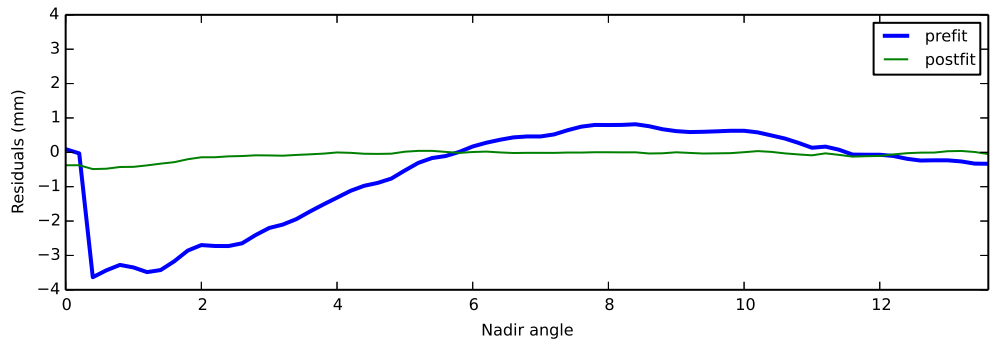

(b) postfit and prefit residuals for SVN56

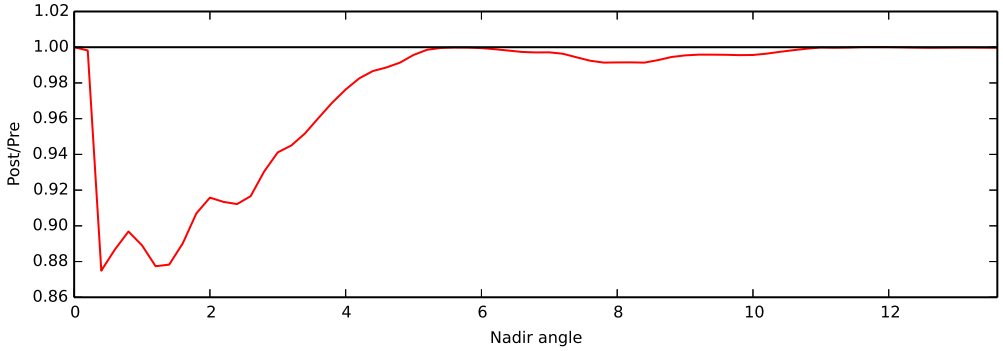

(c) Ratio of postfit/prefit elevation angle

Figure 4.12: Estimated Nadir PCV corrections for SVN56, obtained from and PWL adjustment of phase residuals from over 456 ground stations from 2010 to 2013.

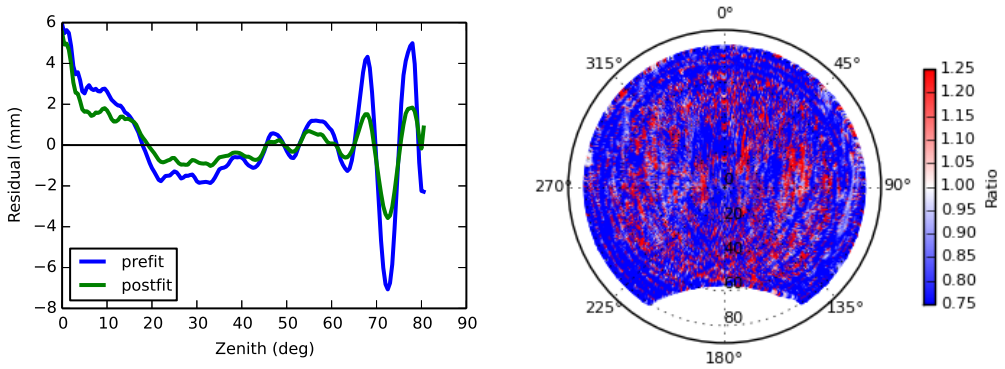

(a) post-fit and pre-fit residuals for an elevation only PWL model with for the IGS station COCO

(b) Ratio of post-fit/pre-fit residuals for azimuth and elevation PWL model with Nadir corrections for the IGS station COCO

Figure 4.13: Post-fit residuals for the IGS station COCO, using the nadir modelling approach.

reliable model.

Estimates for nadir angles between 13.6° to 14.0° are too unreliable, and should not be implemented. These may be improved if the observations in this region can be more accurately weighted in the adjustment, and within the original processing; or if a lower elevation mask is used in the original processing run. The formal uncertainties obtained from the adjustment do not truly reflect the magnitude of uncertainty of the model being estimated and overly optimistic. A large number of observations are key to the successful estimation of nadir PCV corrections. The most efficient away to achieve this is through the processing of a large global network, and including all of the phase residuals into one single adjustment.

The stacking approach is much simpler and easier to estimate that the two staged nadir PCV correction estimation and site model adjustment procedure. The differences between the models are small at the 1-2mm level, however they could be significant for long baseline solutions, or global processing where orbits are likely to be estimated.

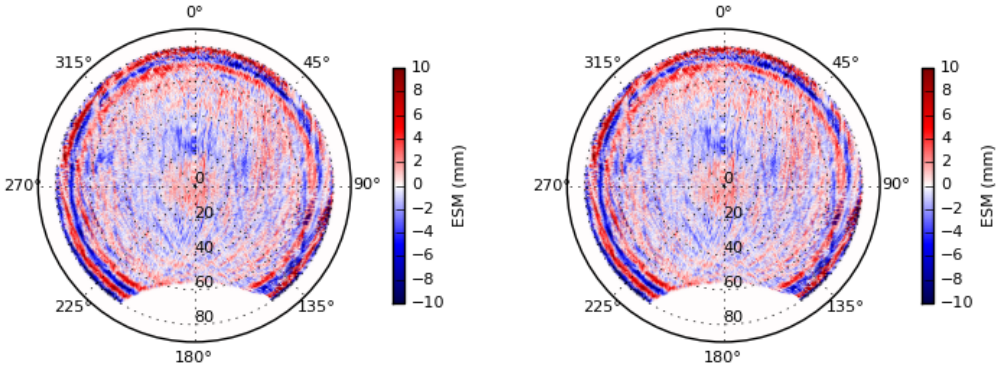

(a) PWL fit for COCO with no nadir PCV corrections applied

(b) PWL fit for COCO with nadir PCV corrections applied

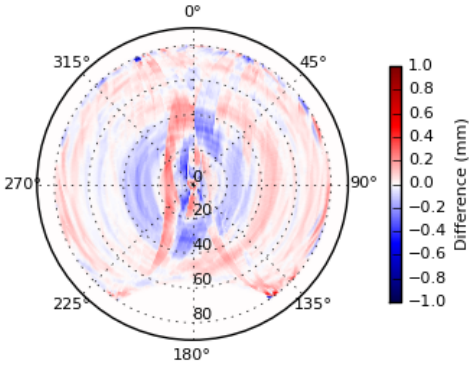

(c) Difference between (a) - (b)

Figure 4.14: Piecewise linear site models for COCO from and adjustment of phase residuals accumulated between 2010 to 2013 (a) without nadir PCV corrections applied, (b) with nadir PCV corrections applied, (c) difference between the two models.

Chapter 5

Case studies

In this section we focus on the impact of applying the ESM to short baseline kinematic processing using the L3 linear combination. We undertook three case studies at station locations with published local tie surveys, Goddard Geophysical and Astronomical Observatory (Maryland, USA), Wettzell Geodetic Observatory (Germany), and Yarragadee Geodetic Observatory (WA, Australia). Experienced surveyors applying the most rigorous methodologies applicable to terrestrial surveying perform local tie surveys. These surveys will serve as a good truth from which we can assess the impact an ESM is having on the GPS solution.

Using a kinematic solution, along with the L3 linear combination will amplify the multipath noise, as demonstrated in earlier simulations. The biases we detect in this section may be larger than those experienced from processing schemes. The advantage of concentrating our analysis to short baselines is the narrowing of potential errors sources. This will allow us to better conclude if the ESM is effective at mitigating multipath effects.

In all of the case studies presented here, the baseline length is very short (< 200 m). For this reason, we have ignored geoid effects between stations when comparing the height measured from the GPS observations to that measured from the local tie survey. Again as the baseline lengths are very short we have only applied the stacking technique, as satellite errors will not be a significant source of error.

5.1 Goddard geophysical and astronomic observatory

The Goddard Geophysical and Astronomic Observatory (GGAO) is located near the town of Greenbelt, Maryland, USA. At Goddard there are two VLBI stations, two SLR stations, and three GNSS stations named GODE, GODS, GODN. Images and characteristics of the Goddard GNSS stations are shown in Fig 5.1 and Table 5.1. Historically, the GODE station has hosted the primary GNSS instrument used by

Table 5.1: GPS stations located at the Goddard Observatory.

Station	Monument Type	Antenna Type	Monument Height
GODE	Wide, low pillar	AOAD/M_T JPLA	0.5m
GODN	Deep drilled braced	TPSCR.G3 SCIS	1.5m
GODS	Deep drilled braced	TPSCR.G3 SCIS	1.5m

(a) GODE (b) GODS (c) GODN

Figure 5.1: GPS stations installed near the Goddard Observatory, (a) GODE, (b) GODS, and (c) GODN. Photos obtained from Fancher *et al.* [2012]

IGS. The ITRF2008 local tie residuals[1] report a -6.1 mm height residual at GODE (residual= Space Geodesy - Tie). As with most local tie residuals, the source of the error is poorly understood.

Our short baseline analysis used the GPS stations GODE, GODN and GODS (see Fig :5.1) with the local tie survey carried out in 2012 [Fancher *et al.*, 2012] as the source of ground truth. GODN and GODS are deep-drilled braced monuments, which have recently been installed. The station GODE has been operating for a decade and is mounted on a low, wide concrete pillar monument with an uncalibrated 'JPLA' radome installed. The JPLA radome was removed on 2012 DoY 189 and re-installed on DoY 349. During the 'radome off' period the performance of the station degraded substantially. As this problem was being investigated, the antenna was changed for a period of 2 weeks from DoY 219 to DoY 219 of 2012. Data during this 2-week period has been excluded from this analysis. Subsequently, the fault was found to be due to an in-line amplifier, which was replaced and the radome re-installed.

[1] http://itrf.ensg.ign.fr/ITRF_solutions/2008/doc/ITRF2008-Tie-Residuals.dat

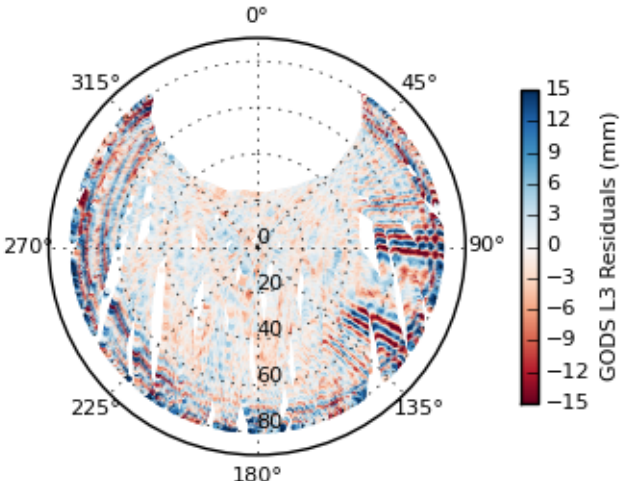

Figure 5.2: GODS L3 azimuth and elevation phase residuals, note the prominent stripes to the east and south east.

5.1.1 Multipath characteristics of the Goddard stations

The GODS station has two distinct azimuthal bands in the polar plot of the L3 phase residuals, which indicate multipath sources at 90° and at 120° (see Fig. 5.2). The remainder of the residual pattern is typical of a monument at a height of approximately 1.5 m above the ground. The stations GODN and GODE do not have any azimuthal dependent multipath sources visible in the L3 residuals.

The GODE phase residuals have a distinct oscillation at low elevation angles between 10° and 30°. This effect remains after the removal of the radome, indicating that it related to the antenna mount used. This pattern is also seen at YAR2, where a similar antenna mount is used (see Fig: 5.14). Close inspection of the GODE elevation phase residuals before and after the radome removal shows a small change at high elevations (see Fig. 5.3). Once the radome is removed the small kink above 85° in elevation has been removed. During the radome off period, an even larger bias in the phase residuals is now present at the highest elevation angles. This could be due the removal of the uncalibrated radome, or the faulty in-line amplifier.

5.1.2 Kinematic processing results

There is an improvement in the accuracy and precision of the kinematic baseline solution when the ESM model is used in the kinematic processing. All of the kinematic baseline solutions obtained using the ESM agreed closely, to within 2-3mm, with the survey results (see Table 5.2). The standard deviation of the height estimates also decreased significantly, by over 1 cm, when the ESM was applied.

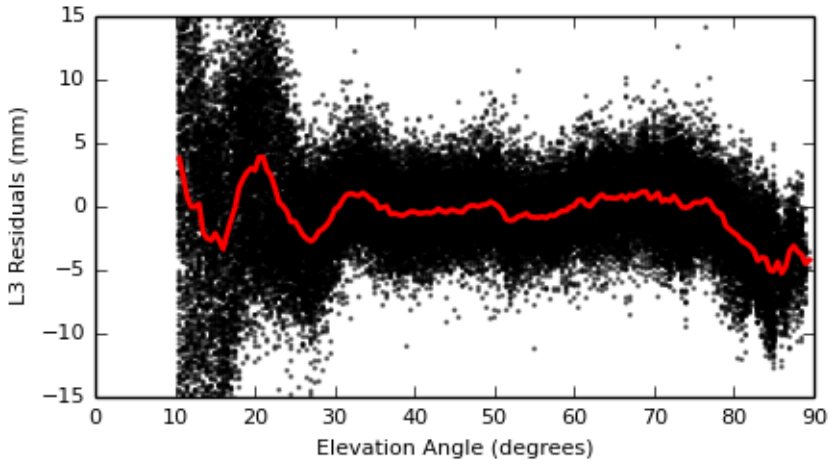

(a) GODE - with JPLA radome

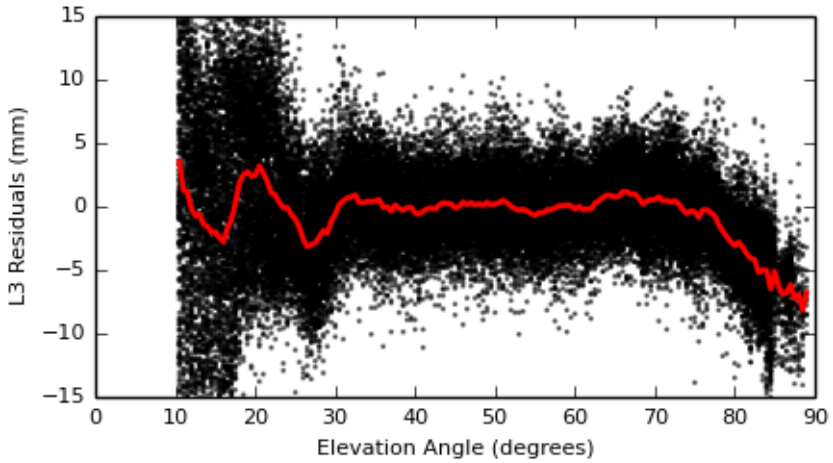

(b) GODE - without JPLA radome

Figure 5.3: GODE elevation only L3 phase residuals, (a) JPLA radome installed, and (b) after JPLA radome removed. There is a small change in the residuals above 85○ in elevation, however the large elevation dependent bias remains.

Table 5.2: Kinematic Processing results for GODE, GODS, GODN, and there differences with terrestrial survey results obtained from NGSWASH1206A.SNX

Baseline	Survey (m)	No ESM applied (m)	Diff. (m)	ESM applied (m)	Diff. (m)	Radome
GODN - GODE						
2012 001 to 189	-3.366	-3.315 ±0.020	0.049	-3.363 ±0.014	0.003	On
189 to 349		**-3.311 ±0.029**	**0.045**	**-3.365 ±0.019**	**0.001**	**Off**
349 to 365		-3.314 ±0.018	0.048	-3.357 ±0.020	0.009	On
GODS - GODE						
2012 001 to 189	-4.591	-4.542 ±0.025	0.049	-4.587 ±0.013	0.004	On
189 to 349		**-4.540 ±0.034**	**0.047**	**-4.591 ±0.021**	**0.000**	**Off**
349 to 365		-4.539 ±0.015	0.046	-4.586 ±0.011	0.005	On
GODS - GODN						
2012 001 to 365	-1.225	-1.224 ±0.014	0.001	-1.224 ±0.011	0.001	N/A

Application of the ESM is particularly effective at modelling the site-specific error experienced at the station GODE. For kinematic baselines which include GODE, there are significant difference in the height estimates of over 48mm from the terrestrial survey results. When the ESM is applied there is a closer agreement with the terrestrial survey results at the 2-3mm level (see Table 5.2).

Removal of the uncalibrated JPLA radome from GODE changed the height differences of baselines including GODE by approximately 3mm. As there is still a significant disagreement between the terrestrial survey results and the change in height from the kinematic solution, after the removal of the radome, we may infer that the majority of the site-specific bias at GODE is coming from the low-wide concrete pillar. There was also a marked increase in the standard deviation of the height estimates during the 'radome off period'. This can be attributed to problems with the in-line amplifier at the time (detailed in the IGS log sheet for GODE).

The kinematics processing results of the GODS-GODN baseline were consistent with the survey results to within 1 mm without the ESM model applied. This indicates that both stations are either installed in a favourable multipath environment despite azimuthal multipath source be apparent in the GODS phase residuals(see Fig: 5.2). Alternatively the multipath characteristics between the two stations is very similar and cancel out on a short baseline both stations. GODS and GODN have a similar monumentation and antenna height and monument installed at a similar. Application of the ESM to the GODS-GODN baseline reduced the standard deviation of the height estimates from the kinematic solution from 14mm to 11mm.

5.1.3 Spectral analysis

Analysis of the spectral characteristics of GPS time series can often reveal relationships and changes not apparent from the position time series. In particular we analysed the periodograms and continuous wavelet transforms (CWT) of the height estimate results obtained from kinematic processing with and without the ESM applied. Results obtained from the periodograms and CWT analysis of height estimates show a consistent decrease in the high frequency noise of height estimates, when applying the ESM.

Applying the ESM to the baseline GODE-GODN significantly reduces a bulge in PSD plots for periods ranging between 0.5 days to 7.5 minutes (0.005 days) (see Fig. 5.4). There is a ramp present in the PSD, with power increasing from high frequencies to low frequencies, regardless of whether an ESM was applied or not, indicating the presence of coloured noise in the time series. There is a change in the slope of the spectra. When the ESM is applied the spectra has a continuously slope, whereas processing without an ESM produces a spectra with slope which flattens at frequencies longer than a day.

The CWT of the same time series shows a similar trend consistent with the periodogram results (see Fig: 5.5). That is a decrease in high frequency noise from a period starting at 1 day through to 12 minutes (0.0089 of a day). Note, in these plots and subsequent plots, we had to recompute the cone-of influence following each gap in the time series data. To produce a continuous time series necessary for CWT, we applied an interpolation using the mean of the time series and with the addition of random noise characterised by the same standard deviation as the observed time series. However, caution should be used when interpreting this data as interpolation causes artefacts, which have no physical meaning.

As expected, the CWT also shows a change in noise characteristic when the radome not present on the station. This is exhibited as an overall increase in noise for periods shorter than 1 day. The power spectra of the GODS-GODN baseline data is flat, with little to no slope present in the periodogram (see Fig: 5.6). As with the GODE-GODN periodogram (Fig: 5.4) there is a bulge in PSD plot starting from 1/2 a day extending through to approximately 7.5 minutes. Again applying the ESM reduces the magnitude of this spectral bulge.

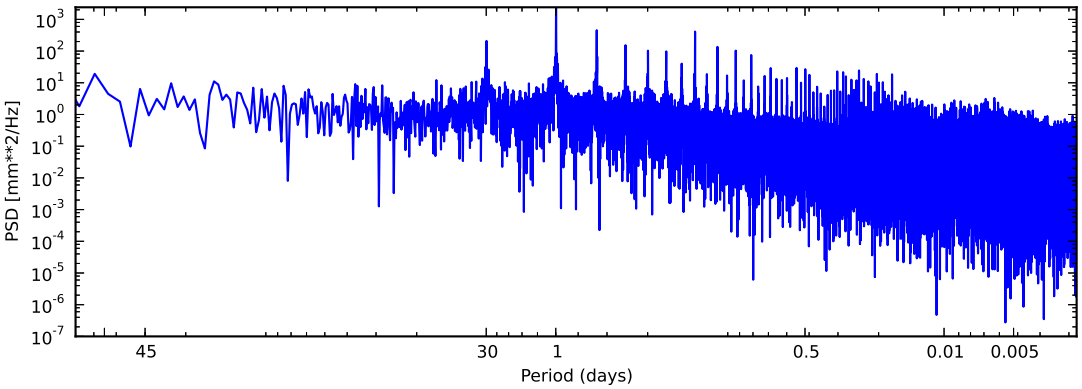

(a) GODE to GODN

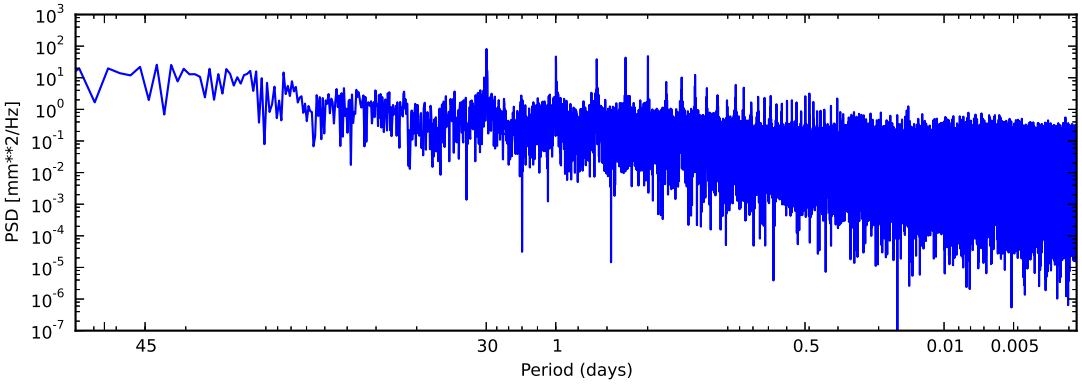

(b) GODE to GODN (ESM applied)

Figure 5.4: PSD of the difference in height from GODE to GODN for (a) standard kinematic solution, and (b) with an ESM model applied. The application of the ESM has removed a significant portion of the high frequency noise.

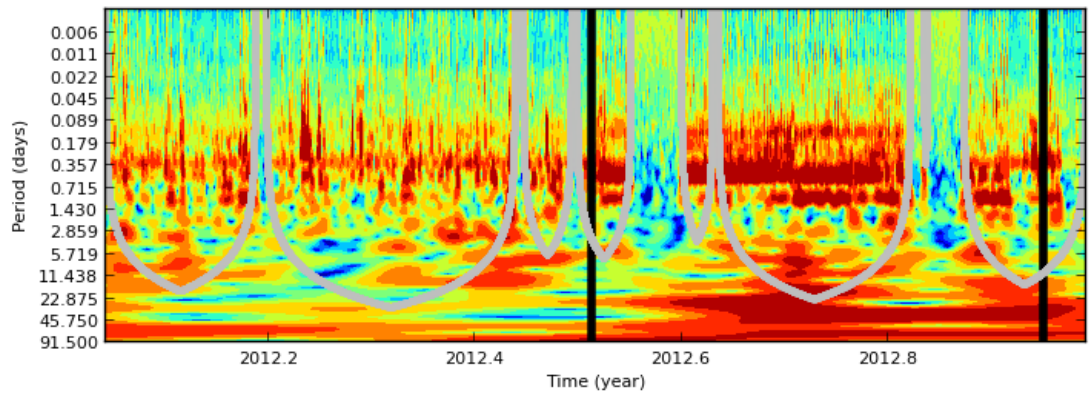

(a) GODE to GODN

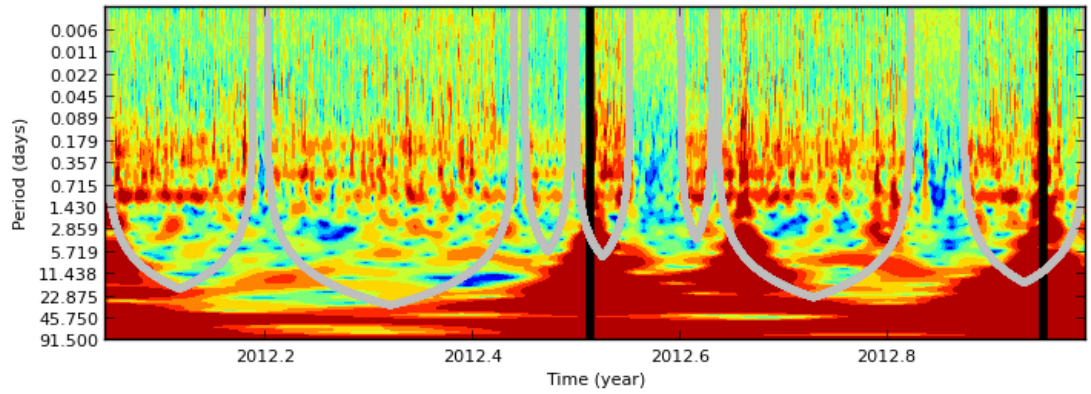

(b) GODE to GODN (ESM applied)

Figure 5.5: Morlet CWT variogram of the height difference between GODE to GODN for (a) standard kinematic solution, and (b) kinematic solution with the ESM modelling applied. The application of the ESM has reduced the high frequency noise components.

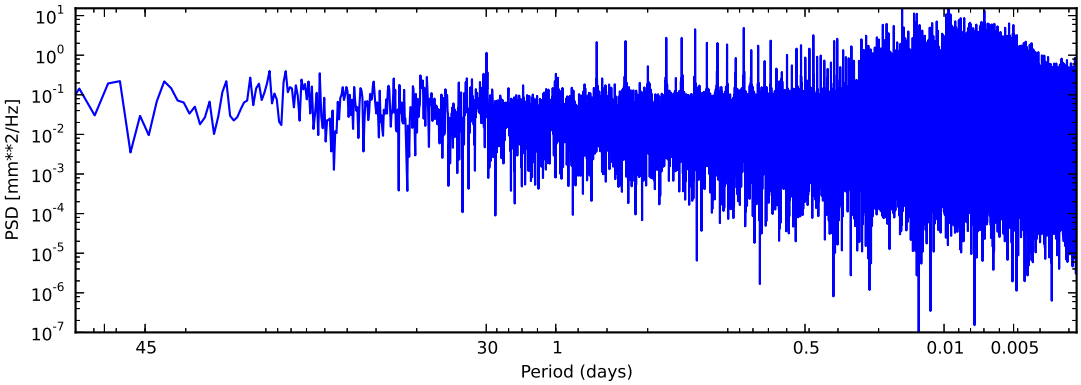

(a) GODS to GODN

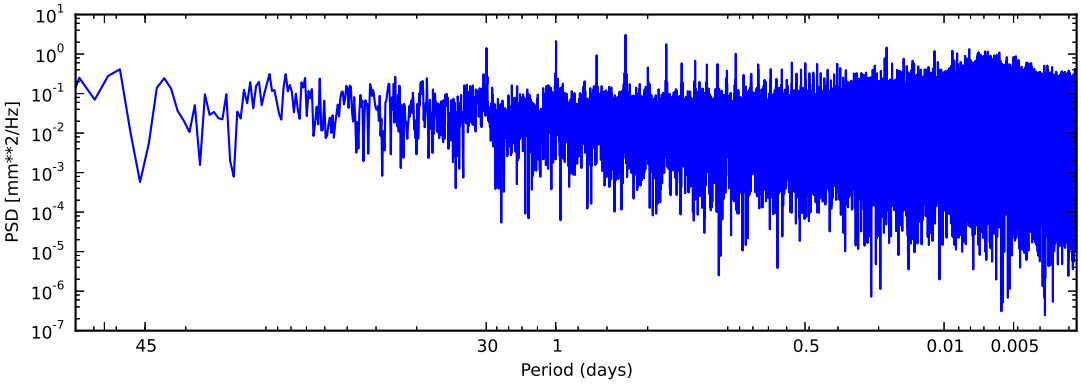

(b) GODS to GODN (ESM applied)

Figure 5.6: PSD of the difference in height from GODS to GODN for (a) standard kinematic solution, and (b) with an ESM model applied. The application of the ESM has removed a significant portion of the high frequency noise.

Table 5.3: GPS stations located at the Wettzell Observatory.

Code	Monument	Antenna
WTZZ	roof top 7.5m	LEIAR25.R3 LEIT
WTZA	roof top 7.5m	ASH700936C_M SNOW
WTZR	roof top 7.5m	LEIAR25.R3 LEIT
WTZS	pole mount	LEIAR25.R3 LEIT

5.2 Wettzell geodetic observatory, Germany

The Wettzell geodetic observatory is outfitted for observations using three different space geodetic techniques for the realisation of the International Terrestrial Reference Frame (ITRF), GNSS, SLR and VLBI. There are up to six GNSS permanent sites operated in parallel with baseline distances of only a few metres, which is an ideal antenna array configuration for studying the impact of site-specific effects. For simplicity we restricted our analysis to four GNSS stations WTZZ, WTZS, WTZR, WTZA. For images and the characteristics of these stations see Fig. 5.7 and Table 5.3. The WTZZ station is the primary station utilized by the IGS with a reported ITRF2008 local tie residuals of up to 13.5mm [Seitz *et al.*, 2013].

Thomas Klüegel provided the terrestrial measurements used as the ground truth for the kinematic processing results from BKG. The results were obtained from a free net solution of terrestrial observations observed in 2012. The height differences from this survey are tabulated in the 2nd column of Table 5.4.

5.2.1 Multipath characteristics

The polar plots of the L3 phase residuals from WTZA show some significant differences in the level of multipath. The strength of the multipath signal is considerably more to the South, and South West of the station, compared to the south east (see Fig.: 5.8). This is expected as the station WTZA is mounted on the North East corner of a roof (see Fig 5.7(e)) with the high residuals in the South West direction likely due to multipath reflections caused by the roof.

The stations WTZR and WTZZ (see Fig: 5.9(a) for WTZZ) are very noisy, whereas the new station WTZS has been mounted away from the roof has distinctly cleaner multipath characteristics (see Fig: 5.9(a)). However there may be a multipath source to the east of WTZS. The contrast in phase residual plots between WTZZ and WTZS highlights the importance of mounting the antenna as far away from reflecting surface as possible.

(a) WTZZ

(b) WTZA

(c) WTZR

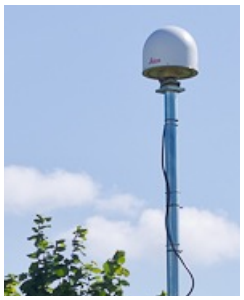

(d) WTZS

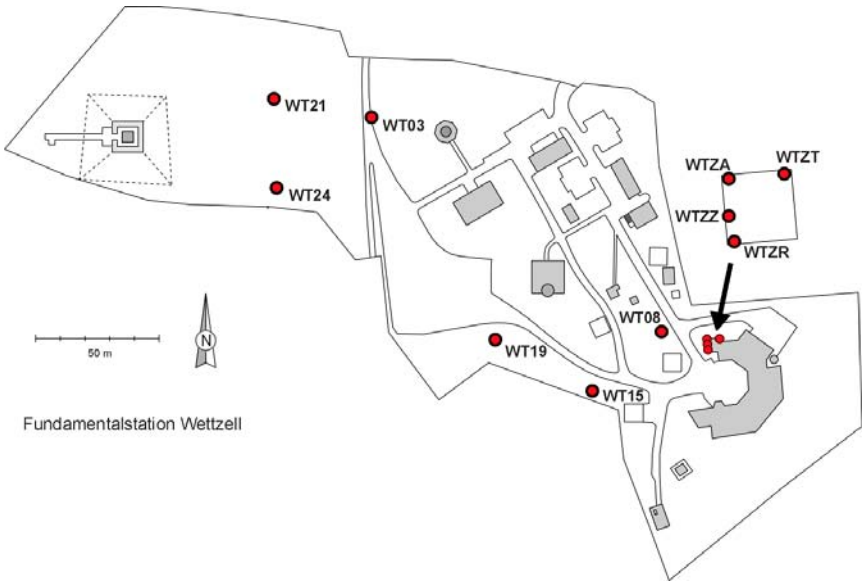

(e) Wettzell Local tie survey map

Figure 5.7: The GPS stations installed at the Wettzell Observatory, WTZZ, WTZA, WTZR and WTZS. Photos obtained from http://www.igs.org, map obtained from [Schlüter *et al.*, 2005] (WTZS is not shown).

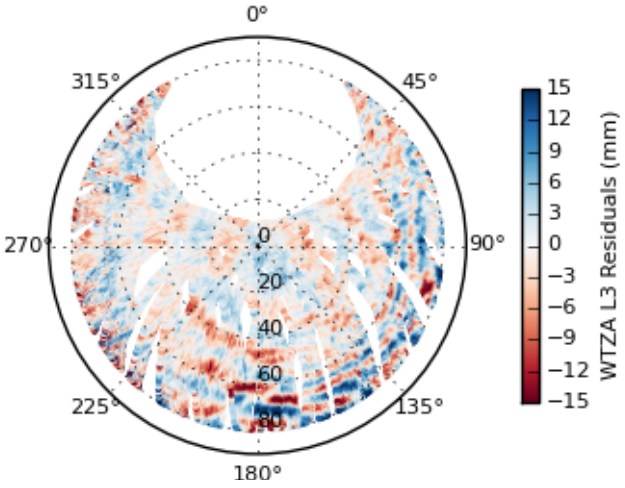

Figure 5.8: WTZA L3 residuals vs Azimuth and Elevations

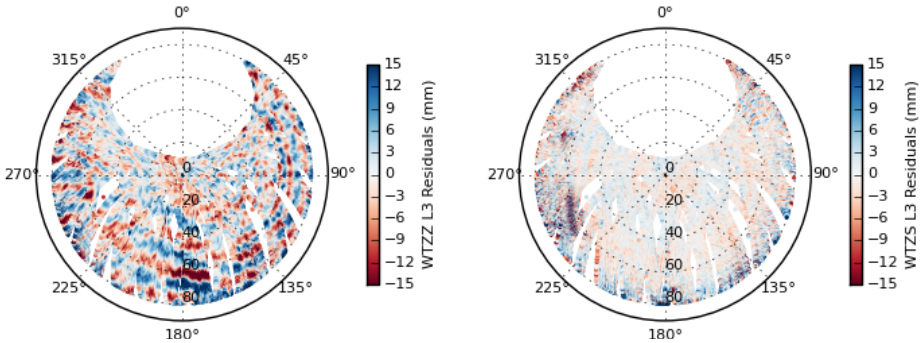

(a) WTZZ (b) WTZS

Figure 5.9: Azimuth and Elevation L3 phase residual plots for (a) WTZZ and (b) WTZS

Table 5.4: Kinematic L3 processing results for WTZZ, WTZA, WTZS, WTZR, and terrestrial survey results.

Baseline	Survey	No ESM applied	diff.	ESM applied	diff.
WTZS - WTZZ	2.467	2.467±0.023	0.000	2.467±0.013	0.000
WTZR - WTZZ	-0.131	-0.131±0.026	0.000	-0.131±0.018	0.000
WTZA - WTZS	-2.486	-2.497±0.012	0.011	-2.491±0.009	0.005
WTZA - WTZZ	-0.019	-0.033±0.020	0.014	-0.023±0.013	0.004
WTZA - WTZR	0.112	0.098±0.026	0.014	0.106±0.014	0.006

5.2.2 Kinematic processing results

Again when the ESM is applied to kinematic short baselines at Wettzell there an improvement in the accuracy and precision of the height estimates (see Table 5.4). In general for all baselines processed the standard deviation of the height estimates decreases in the order of 3 to 12 mm.

Without the ESM applied, baselines which include the station WTZA, have a significant disagreement with the terrestrial survey, of 14 mm for WTZA-WTZZ, 11 mm for WTZA-WTZS, and 14 mm for WTZA-WTZR . Whereas the WTZS-WTZZ baseline and the WTZR-WTZS baseline, agree to better than 1 mm with the terrestrial survey results. This indicates that there is a local site-specific multipath effect at WTZA causing a bias of approximately 11 -14 mm.

Application of the ESM effectively mitigated much of the local site-specific error at WTZA, reducing the disagreement with the terrestrial survey from 11-14 mm to an agreement with the terrestrial survey results within 5 mm. Spectral analysis Again there is a consistent reduction in the high frequency noise components, for sub-daily periods, for all of the baseline processed at Wettzell when an ESM is applied.

The periodograms for the WTZA-WTZR baseline show a reduction in the power of the over broad range of sub-daily starting from approximately of 0.5 days (see Fig: 5.10) through to approximately 7.5 minutes (0.005 day).

The CWT of the height estimates for the baseline WTZS - WTZZ shows a distinct change of noise characteristics (see Fig. 5.11). This change coincides with a change in receiver (on the 9th of July 2012), which caused a significant increase in noise for periods less than 1 day. The cause of the change in noise characteristics is unexpected as the receiver was installed at the time is reported of being the same make and having the same firmware installed. Comparing the CWT analysis with and without the ESM applied, it is apparent that the ESM significantly reduces the noise in sub daily periods, even when the receiver has been changed.

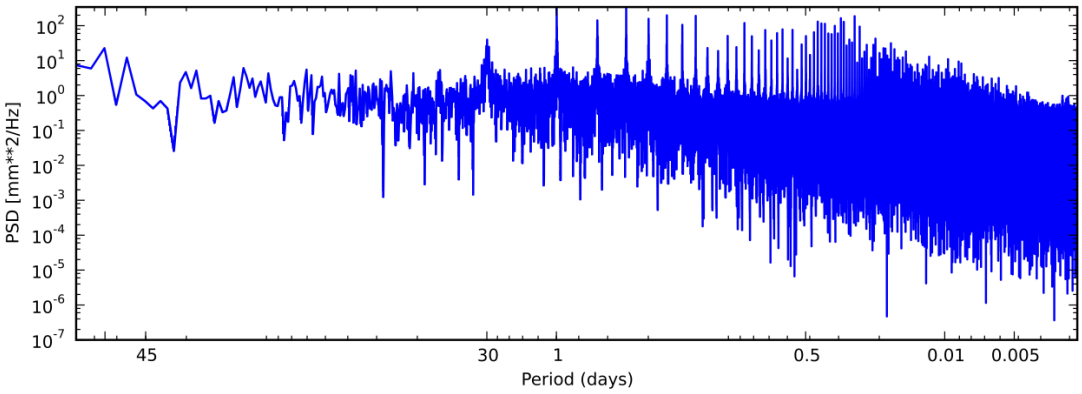

(a) WTZA to WTZR

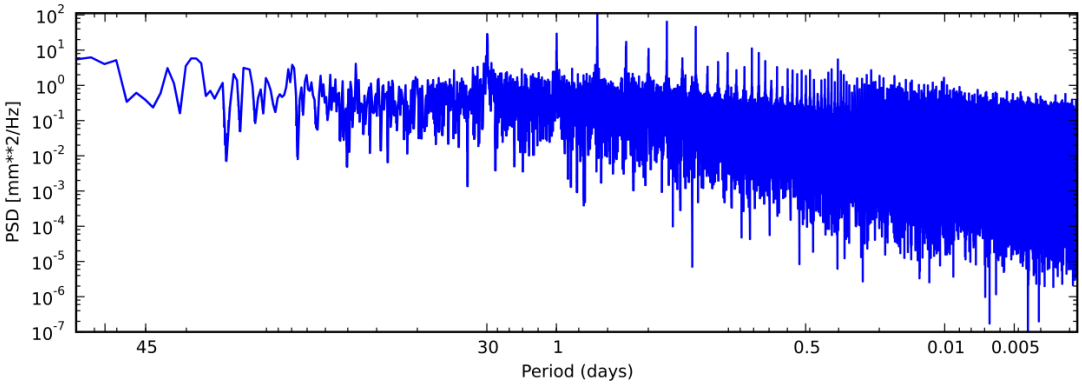

(b) WTZA to WTZR (ESM applied)

Figure 5.10: PSD of the difference in height from WTZA to WTZR for (a) standard kinematic solution, and (b) with an ESM model applied. The application of the ESM has removed a significant portion of the high frequency noise.

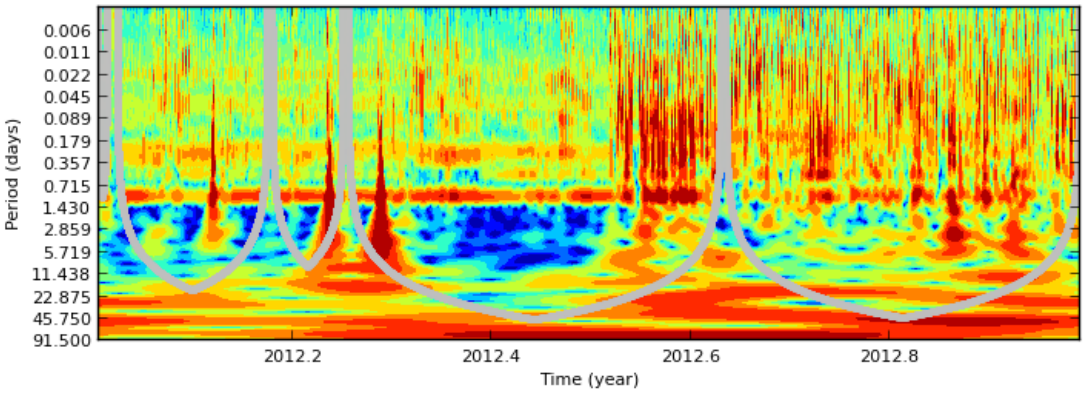

(a) WTZS to WTZZ

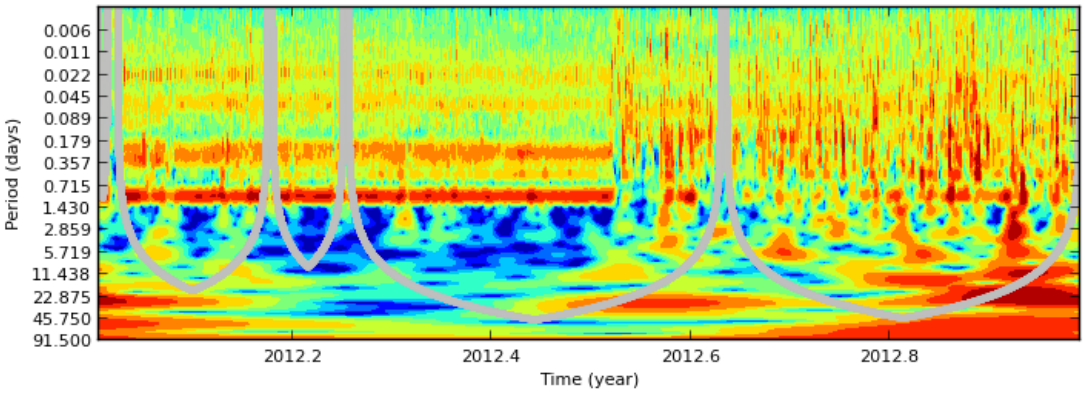

(b) WTZS to WTZZ(ESM applied)

Figure 5.11: Morlet CWT variogram of the height difference between WTZZ to WTZS for (a) standard kinematic solution, and (b) kinematic solution with the ESM modelling applied. There is a significant change in spectral characteristics following a receiver firmware change at WTZZ near 2012.5. The application of the ESM has reduced the high frequency noise components.

Table 5.5: GPS stations located at the Yarragadee Observatory.

Station	Monument Type	Antenna Type	Monument Height
YAR2	Raised from ground in a steel support	AOAD/M_T JPLA [2]	0.01 m
YAR3	Tall narrow pillar	LEIAR25 NONE	1.5 m

Figure 5.12: The YAR2 GPS station installed at the Yarragadee Observatory (photo provided by Nicholas Dando).

5.3 Yarragadee geodetic observatory, Western Australia

The Yarragadee geodetic observatory is equipped for observations using four different space geodetic techniques for the realisation of ITRF: SLR, VLBI, GPS, and DORIS. For this case study we focus on the two GNSS stations run in parallel at Yarragadee, YAR2 and YAR3 (see Figure 5.12 and Table 5.5). The YAR2 station is the primary station used by the IGS, with a reported ITRF2008 local tie residual between YAR2 and the SLR station (7090) of 14mm [Altamimi *et al.*, 2011]. The VLBI station has only recently been constructed and local tie residuals between the GPS and VLBI station are not yet available. The local tie survey carried out in 2007 [Woods and Ruddick, 2007] serves as the ground truth for the kinematic analysis.

The YAR2 antenna is mounted close to the ground upon a steel frame similar in style to the station GODE(see Fig: 5.1(a)), whereas YAR3 is mounted on a 1.5m high pillar. The YAR2 station has an uncalibrated 'JPLA' radome of the same design as that installed at GODE. As part of the same international uncalibrated radome experiment, the YAR2 radome was removed on 2012 DoY 144, and re-installed on 2012 DoY 272. The radome was later permanently removed on 2013 DoY 171. It is also worth noting that there is a misalignment of the JPLA radome with the centre of the antenna, noticeable if you look closely at Fig: 5.12.

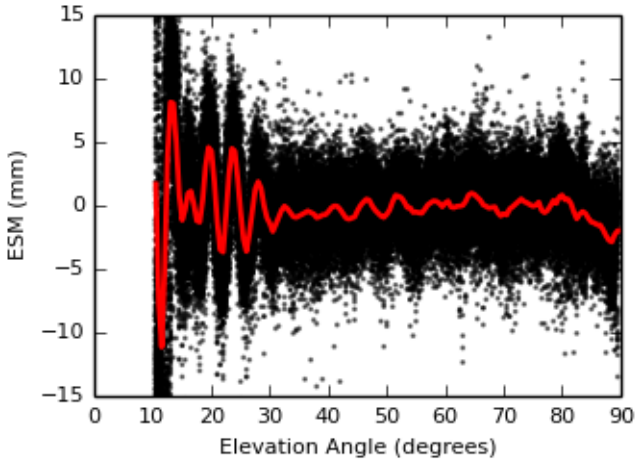

Figure 5.13: YAR3 elevation dependent L3 phase residuals vs. elevation angle

5.3.1 Multipath characteristics

There no significant azimuthal multipath sources apparent in the stacked phase residual plots for YAR2 and YAR3. The elevation dependent plot of phase residuals for YAR3 are consistent with those expected from a high monument, with the exception of bias at the high elevation angles (see Fig 5.13). The phase residuals at YAR2 has a distinct oscillation present for low elevation angles between 10° to 30 °. Superimposed on this is a slow varying change in phase residuals similar to that simulated for low monuments (see Sec: 3.2.1 and Fig. 3.1(c)). The removal of the JPLA radome from YAR2 caused a small change in the L3 phase residuals - removing the small kink at elevations above 85° (see Fig. 5.14). However the oscillation at low elevation angle persists, indicating that this is caused by the mounting holding the antenna above the ground, and not by the radome. The effect is similar to the one seen at GODE (see Fig 5.3), which uses a similar mount.

5.3.2 Kinematic processing results

As for the previous two case studies, application of the ESM significantly improved the accuracy and precision of the baseline solutions when the JPLA radome is installed at YAR2 (see Table 5.6). However, when the JPLA radome is absent at YAR2, the ESM degraded the accuracy of the solution.

The kinematic solution of the YAR2 - YAR3 baseline observations with the JPLA radome installed had a mean difference of 9.7mm from the levelling results. With the ESM is applied, the height difference to the terrestrial survey results decrease to 1 mm, and the standard deviation decreases from 10mm to 7mm.

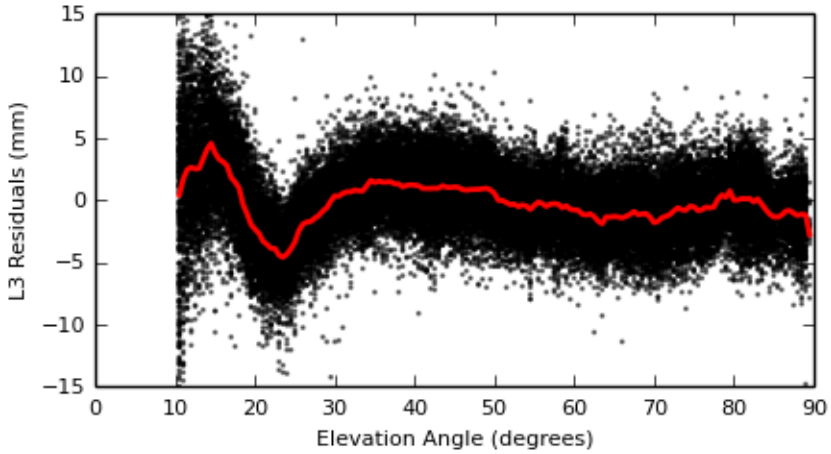

(a) YAR2 - with JPLA radome

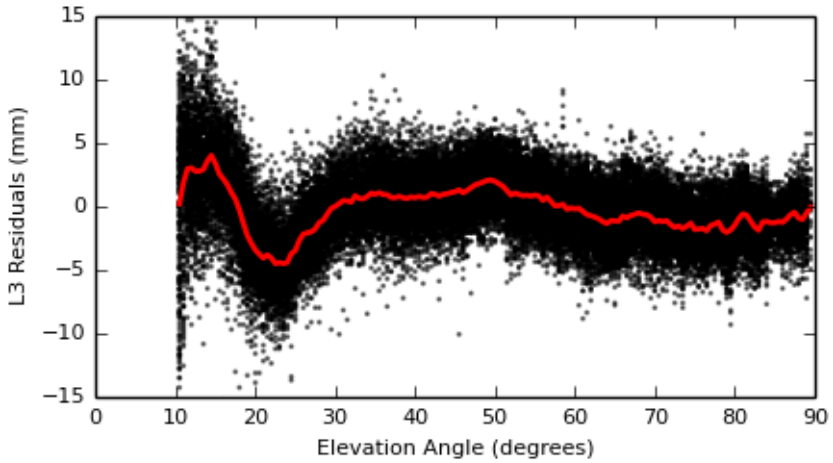

(b) YAR2 - without JPLA radome

Figure 5.14: YAR2 L3 elevation only phase residuals for (a) JPLA radome installed, and (b) after JPLA radome removed. There is a small change in the residuals above 80° in elevation, however the large elevation dependent bias remains.

Table 5.6: Kinematic Processing results for YAR2, YAR3, and terrestrial survey height differences

Baseline	Survey (m)	No ESM applied (m)	Diff. (m)	ESM applied (m)	Diff. (m)	Radome
YAR3 - YAR2	-1.155					
2012 001 to 144		-1.146 ±0.011	0.009	-1.156 ±0.008	0.001	On
144 to 272		**-1.152 ±0.010**	**0.003**	**-1.162 ±0.007**	**0.007**	**Off**
272 to 365		-1.146 ±0.011	0.009	-1.156 ±0.009	0.001	On

In the absence of the JPLA radome at YAR2, the agreement with the terrestrial survey improves to a difference of 3.1mm (no ESM applied). However, application of the ESM to YAR2 observations without the radome present, resulted in a larger disagreement with the terrestrial survey results to 7mm, although the standard deviation still decreased by 2mm. The removal of the JPLA radome reduces the site-specific error considerably at YAR2, and was the dominant source of error at this station.

If the true multipath environment is similar to that generated for $H = 0.17$m in the simulations, then we are not expecting to obtain a good result from the phase residuals at YAR2. We infer that the uncalibrated radome is introducing a larger site-specific multipath causing a bias in the height measurement, which can be mitigated by an ESM. However, when the radome is removed the site-specific error changes its characteristics significantly to one which is likely to varying slowly with elevation, and thus poorly removed by the ESM technique. This needs to be confirmed through a calibration of the JPLA radome to check the misalignment may affect the antenna PCV pattern.

5.3.3 Spectral analysis

The spectral analysis shows a change in spectral characteristics when the ESM is applied. Analysis with the CWT also shows changes in spectral characteristics when the radome is removed from YAR2. For the baseline YAR2 - YAR3 the sub-daily period between 1/2 day to 5 minutes has been reduced through the application of the ESM (see Fig: 5.15. However when we look at the results from the CWT transform, the changes are significantly more complex (see Fig: 5.16). When the radome is removed from YAR2 the power in the CWT at periods near 0.2 of a day disappear. Whereas the power at the higher frequency persists throughout the time series. Application of the ESM reduces the highest frequency noise, however the noise near the 0.2 day period increases.

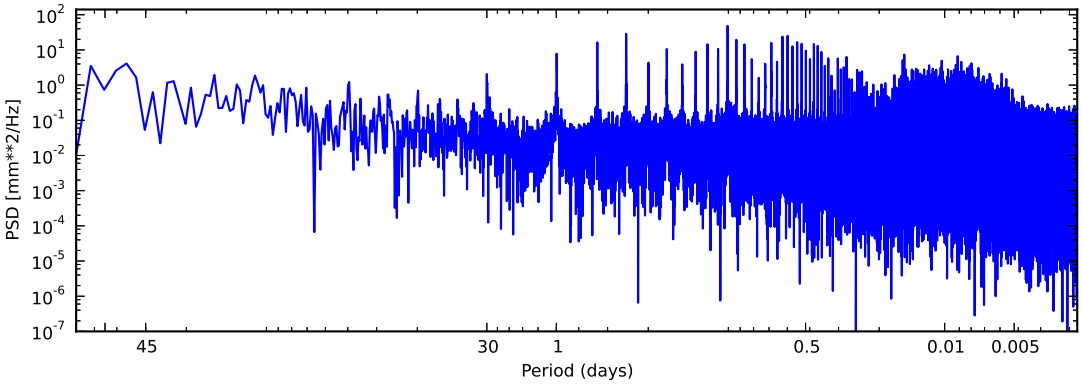

(a) YAR2 to YAR3

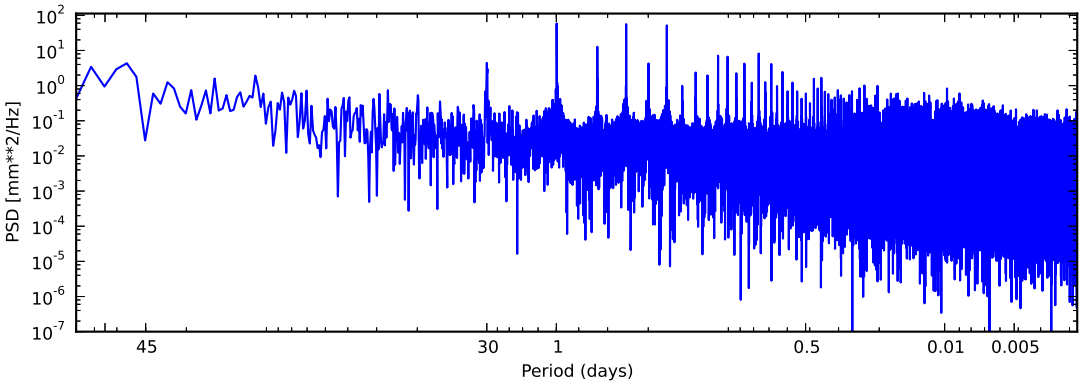

(b) YAR2 to YAR3(ESM applied)

Figure 5.15: PSD of the difference in height from YAR2 to YAR3 for (a) standard kinematic solution, and (b) with an ESM model applied. The application of the ESM has removed a significant portion of the high frequency noise.

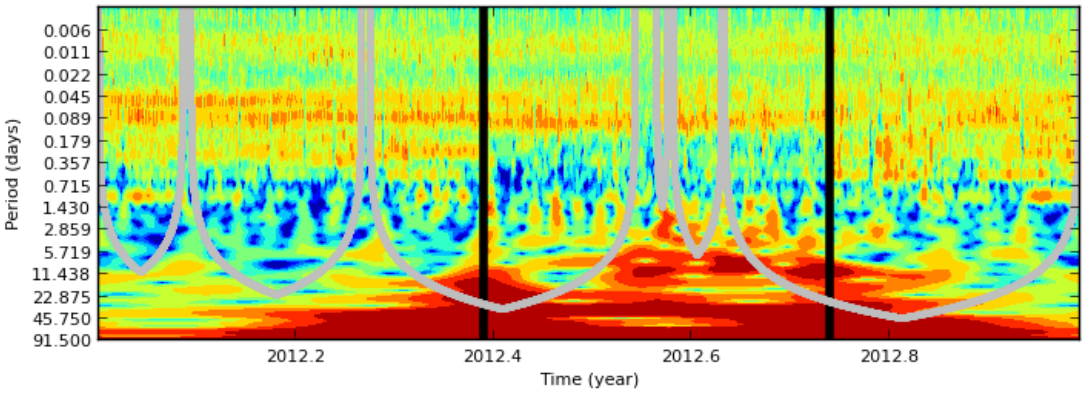

(a) YAR2 to YAR3

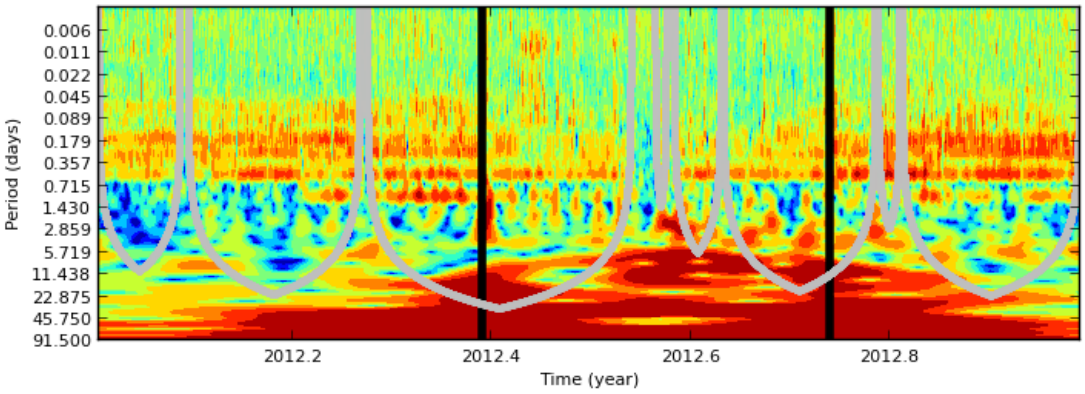

(b) YAR2 to YAR3(ESM applied)

Figure 5.16: Morlet CWT variogram of the height difference between YAR2 to YAR3 for (a) standard kinematic solution, and (b) kinematic solution with the ESM modelling applied.

5.4 Summary

In this section we have analysed the application of an ESM to three different case studies. For each of these case studies there was a significant difference between the GPS height difference and the terrestrial levelling results. The application of the ESM to the short baseline kinematic processing significantly reduced the discrepancy by over 10 mm. In addition to the reduction of the bias, was a reduction in the variance of the positioning solutions. Spectral analysis shows that there was a marked reduction in the power of the noise for the high frequency components. The favourable results here confirm that the models derived from phase residuals obtained from a large global solution can be applied to different processing strategies, and within different software packages.

We will now investigate the impact of applying the ESM and nadir modelling techniques to large global solutions.

Chapter 6

Global solutions

In this chapter we assess the performance of applying the two different empirical modelling techniques, upon a global solution. In particular we have analysed how the different modelling approaches affect positioning and velocity estimates as well as IGS products, such as satellite orbits, and clock estimates.

The analysis presented here is based on a subset of data computed from 2010 through to the end of 2013. In this chapter we refer to the ANU/MIT solution submitted to IGS second reprocessing campaign, as the *standard solution*. The *ESM solution* refers to the global solution which has had the block median site-specific models applied, and the *nadir solution* refers to the global solution which applied the piecewise linear fit for satellite and site-specific errors. Unless otherwise stated the position time series have been derived from the final set of coordinates obtained from the IGS reprocessing run. That is the orbit parameters, clock terms and satellite antenna offsets have been estimated, from previous processing, and are then held fixed to obtain the final set of station coordinates.

For the time period from 2010 to 2013 over 605 different GPS stations were processed. For our subsequent analysis the stations selected required a minimum of 1000 observations, and a horizontal random walk of less than $0.5\text{m}^2/\text{yr}$. This filters out stations that have experienced a large earthquake and the subsequent earthquake model does not yet fit the time-series satisfactorily. This reduced the total number of stations to be analysed to be 183 (see Figure 6.1).

Assessing which solution was performing the best is not a trivial task. When we make our comparisons we have to keep in mind that we can be improving the precision of the solution, but this could be coming at the cost of accuracy. Determining the accuracy of a solution obtained from a global solution is particularly difficult, as it is hard to come across another solution to which we can define as the *truth* from which to make a comparisons with.

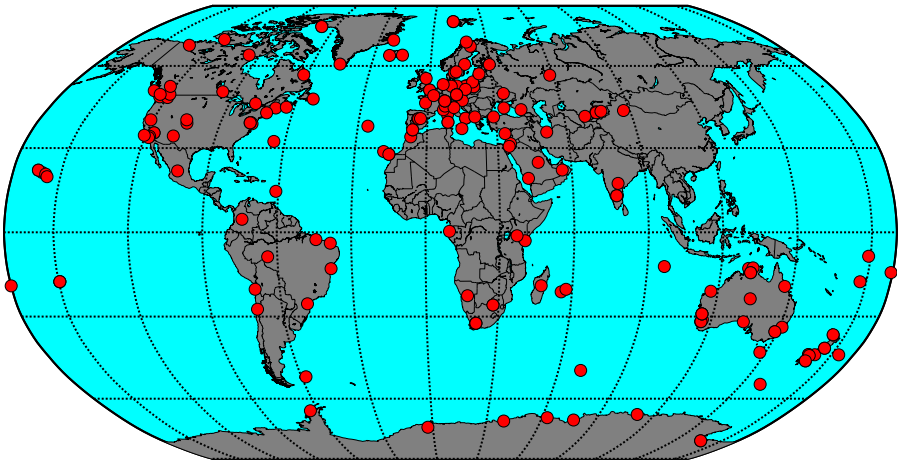

Figure 6.1: Map showing the selected stations with over 1000 observations between the period of 2010 to 2013, and a horizontal random walk less than $0.5 m^2/yr$ (a total of 183 stations).

6.1 Phase residuals

Analysing the phase residuals on a site-by-site basis after the modelling has been applied will gives us an indication of how much of the systematic error has been removed from the observations. First we looked at the impact of the different models had upon the phase residuals on a station-by-station basis. Then we investigated the impact the modelling had upon the nadir residuals.

6.1.1 Station stacked phase residuals

There was a significant difference in the character of the post-fit phase residuals upon after an ESM or nadir model was applied. Stacking the phase residuals at each station from an ESM solution resulted in significantly less variation in the phase residuals, and the RMS of the phase residuals was substantially reduced. The effectiveness of the block median ESM in reducing the variation in the phase residuals is summed up by the histogram (see Fig: 6.2). The ESM solution produced a marked shift in the distribution of RMS values to the majority of stations having an RMS well below 2 mm. The nadir solution had less of an impact, but still resulted in a reduction in the phase RMS.

We observed substantial decreases even in low multipath environments, such as CEDU, where there was a significant decrease in RMS from 3.05 mm to 1.21 mm. Applying the Nadir model still resulted in a reduction in the variation of the phase residuals, but this was substantially less than just applying the ESM model.

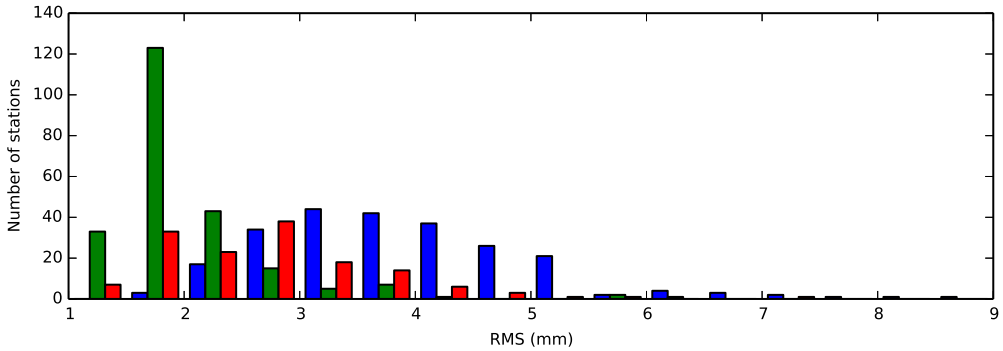

Figure 6.2: Phase residual RMS for standard, ESM and nadir solutions. The ESM solution has significantly improved the phase RMS

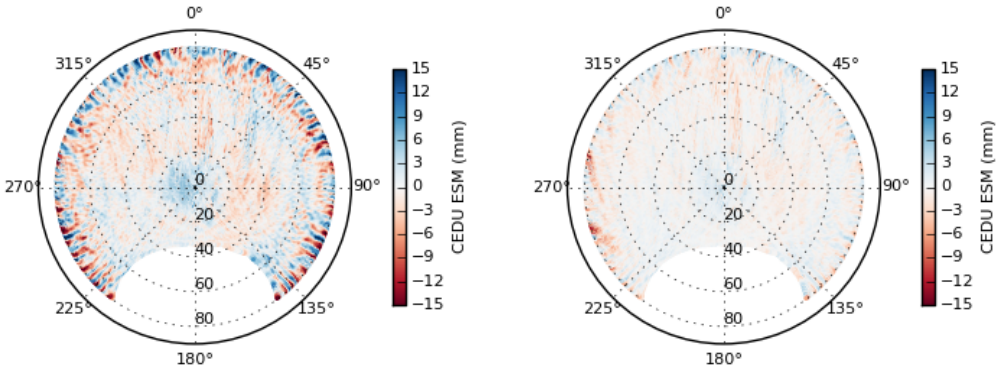

(a) Standard solution RMS = 3.05

(b) ESM solution RMS = 1.21

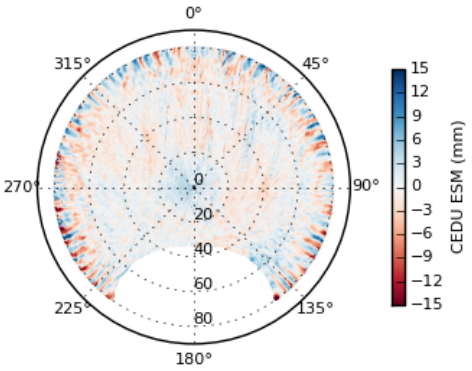

(c) Nadir solution RMS = 2.21

Figure 6.3: Stacked phase residuals for the GPS station CEDU obtained from the standard, ESM and nadir solutions. A block median fit at resolution of 0.5° was used to calculate the RMS of the model.

6.1.2 Nadir stacked phase residuals

To assess the impact of the modelling techniques have had upon the corrections to the nadir PCV models for each satellite, we computed the adjustment that would be required to the nadir model if a second iteration was to be computed. Recall that from the standard solution the phase residuals indicated that there were some significant adjustments required for several SVNs, particularly for nadir angles between 0° to 5° (see Fig: 6.4(a)).

If the ESM technique was performing correctly, that is only the site-specific errors were being modelled, then there should be a minimal impact on the adjustment of the nadir phase residuals. The overall RMS for all of the nadir PCV adjustments only decreased marginally from 0.51mm to 0.47mm (compare Fig: 6.4(b) to Fig: 6.4(c)).However there are several SVNs for which the adjustments required have substantially increased. For instance SVN 66 performs poorly when we compared the adjustment model obtained from standard solution with those obtained from the ESM solution (see Fig: 6.6(a)). The correction to the nadir PCV model obtained from the ESM solution, for SVN 66, appears random in nature. For SVN 49, the ESM solution had a significant difference in nadir adjustment model near a nadir angle 1°, and then again between 3° and 5° (see Fig: 6.6(b)). Indicating that the corrections to the nadir PCV appear to be diverging for the satellite.

After applying the nadir model, there is an overall reduction in the adjustment required (see Fig: 6.4(c)), with the total RMS decreasing to 0.29mm. Notably there is no longer any significantly outlying SVN that appears to require a significant adjustment to the nadir phase model, with all of the adjustments being at our below the 1mm level. However when we closely inspect the change in RMS of the adjustment model for each SVN (see Fig: 6.5) we found a number of cases where the RMS had increased, for instance SVN 023 increased in RMS, despite originally having a very small adjustment required from the standard solution.

Comparing the nadir adjustment model derived from the standard solution and the nadir solution (see Fig: 6.7) there has been an overall increase in magnitude in the correction estimated for all nadir angles. This is mostly likely to be due to the original model not being significantly different to the original phase model and should not have been applied. That is the original corrections were not significant, and should not have been applied.

Looking at the RMS for the estimated corrections on a satellite by satellite basis (see Fig: 6.5) an overall pattern emerges. If the RMS was below 0.58mm, then the adjustment model should have been disregarded. As any improvement through its application would be minor, or result in degradation as observed for SVN 23.

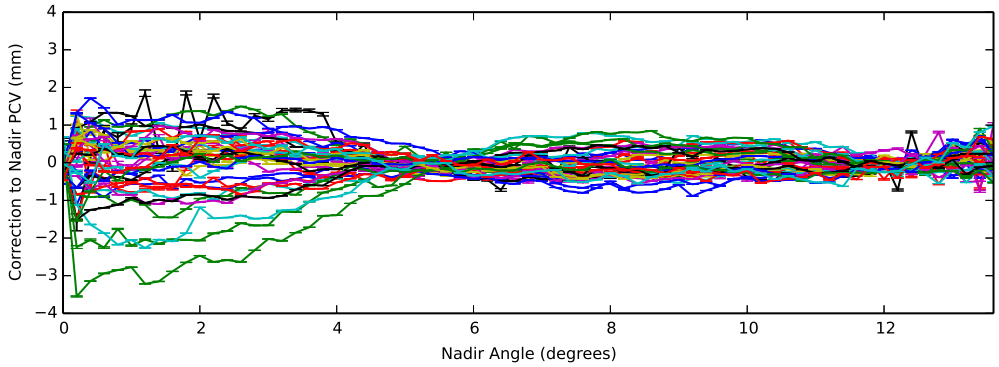

(a) Standard solution, RMS = 0.51 mm of all satellites

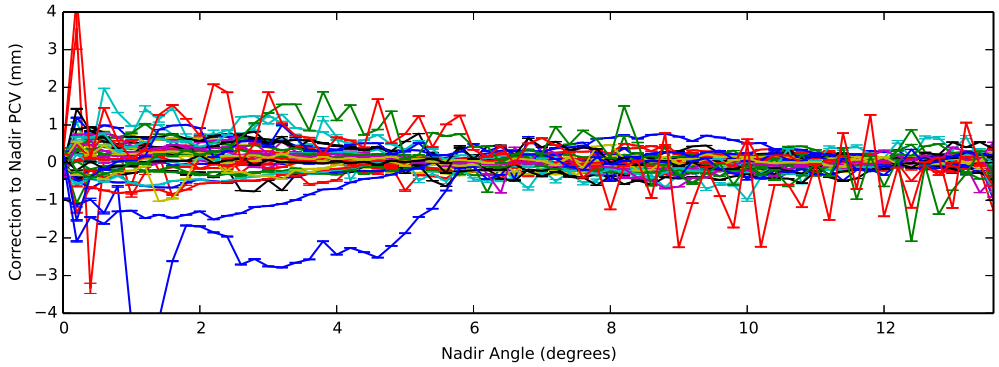

(b) ESM solution, RMS = 0.47 mm of all satellites

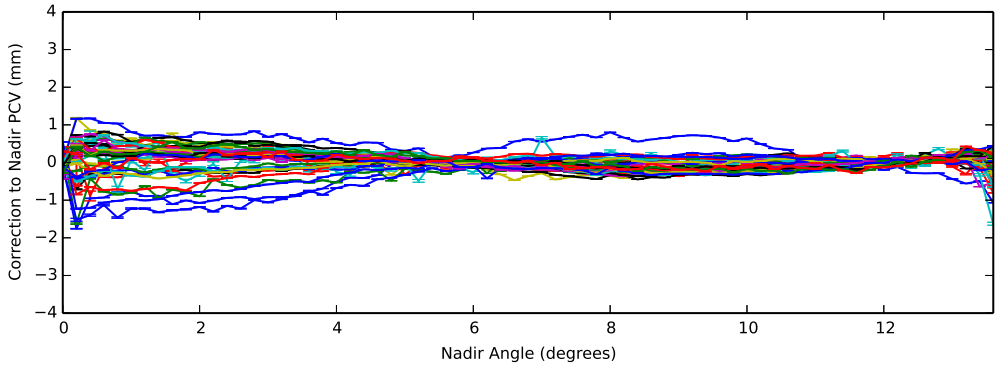

(c) Nadir solution, RMS = 0.29 mm, of all satellites

Figure 6.4: The calculated adjustments to the Nadir PCV model obtained from the (a) standard, (b) ESM , and (c) nadir solutions

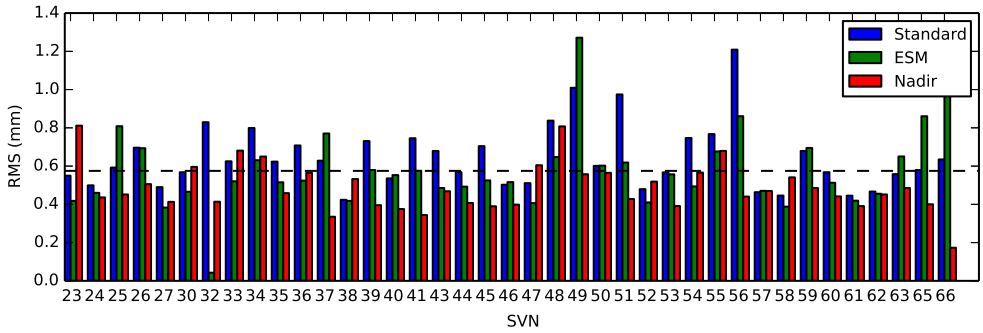

Figure 6.5: Comparison of Nadir Phase residual RMS for standard, ESM, and nadir solutions for each SVN. The dashed line indicates a cut-off RMS where the adjustments to the nadir PCVs may be considered significant. Adjustments from the standard solution which fall below this line should not have been applied.

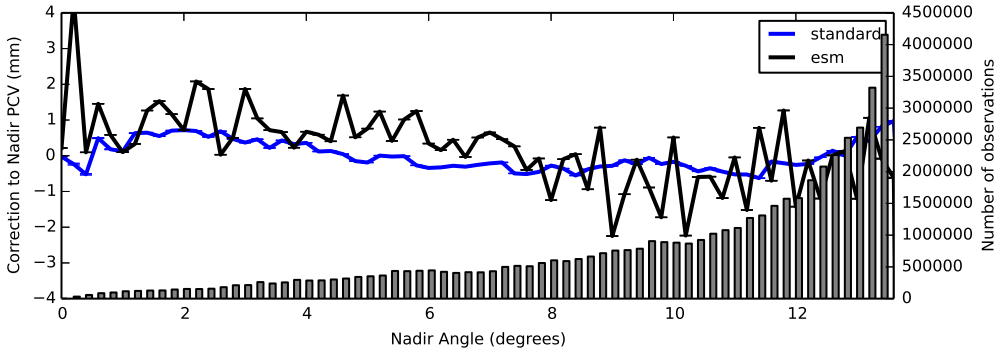

(a) SVN 066

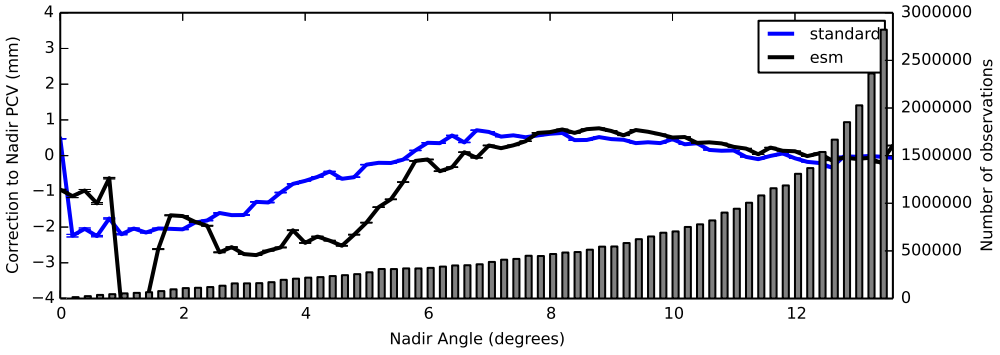

(b) SVN 049

Figure 6.6: Comparison of nadir adjustment models derived from the standard and ESM solutions.

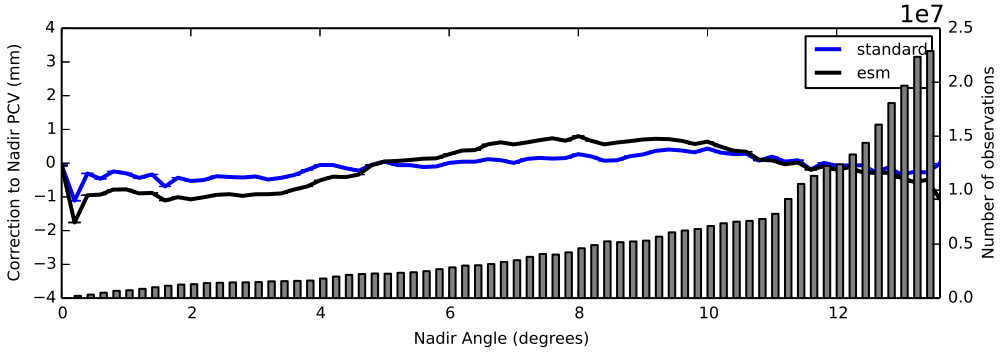

Figure 6.7: Comparison of Nadir phase residuals stacked for the standard and nadir solution for SVN 23

The ESM solution had a marked impact upon the residuals stacked on a station-by-station basis. However the performance of the ESM solution with respect to the nadir PCV adjustments indicates that the ESM can have an unpredictable effect. This is an indication that the ESM modelling technique is absorbing some of the satellite specific effects within the station model.

The nadir solution resulted in a reduction in the RMS of the station models, however systematic effects, of a smaller magnitude than the standard solution could still be observed. This indicates that the station model needs to be improved or a second iteration of the model needs to be applied. The nadir adjustments reduced significantly for the majority of SVNs, however there is a need to only apply adjustments to those SVNs, which have the largest differences. An RMS value, for the adjustment model of 0.58mm is a good cut-off value.

6.2 Time series comparison

To obtain the residual time series we first introduced a discontinuity to the time series if there was an earthquake of magnitude greater than 7 near an observing station. Then from the station metadata discontinuities were introduced whenever there was a change in the antenna set-up. Initially all of the discontinuities were set to be a linear jump in the time series. A linear trend to the time series, as well as an annual and semi-annual terms were estimated, and then an offset due to the discontinuities were also estimated. The uncertainties for the time-series were computed using the real-sigma algorithm, which takes into account time-correlation. The data was filtered for outliers which had a σ greater the 2cm, any value which lay outside of 4 normalized σ were also removed. The estimates of the discontinuities were checked to make sure

Table 6.1: Median Random walk (m^2/yr), minimum number of observations = 1000, nsigma = 4 , maxsigma 0.02

Solution	Annual Semi	North	East	Up
standard	N	1.79	1.94	31.54
ESM	N	1.65	1.79	29.95
nadir	N	1.65	1.70	29.95
standard	Y	1.07	1.07	18.41
ESM	Y	1.07	1.28	20.00
nadir	Y	1.02	1.07	17.61

they were statistically significant. If discontinuities had a $\tilde{\chi}^2$ value of less than 3, then the discontinuity with the smallest $\tilde{\chi}^2$ was removed from the discontinuity file, and the fit to the time series was re-run. Where necessary the earthquakes were fitted with a non-linear function.

A random walk noise model was fitted to the subset of stable GPS time series. This was computed with and without annual/semi-annual terms fitted to the time-series. The median value from each solution is shown in Table 6.1. When no annual or semi-annual terms are fitted the ESM and nadir solutions have a very similar performance. Both solutions were slightly quieter than the standard solution. However, if annual and semi-annual terms are first fitted to the time series, and then the ESM solution is noisier than the standard and nadir solutions for the east and vertical components. Whereas the nadir solution produced a slightly quieter solution in the order of 0.8 m^2/yr.

Comparing the mean weekly RMS of the height estimates for the standard solution (3.47 mm), the ESM solution (3.36 mm) and nadir solution (3.37 mm) had the same level of improvement. However comparing the time series of weekly median RMS of the coordinate solution (see Fig: 6.8) shows that the performance of the ESM is some what erratic. For some weeks the application of the ESM has decreased the RMS noise level (see Fig: 6.8(a)), while for others it actually increases the RMS noise level. The nadir solution on the other hand results in marginally less of a decrease in the RMS, but the decrease is consistent throughout the time series.

One of the key factors controlling how reliably GPS time series can be utilised for further analysis of geophysical signals or in reference frame determination is the level of uncertainty in velocity estimates are. Traditionally the statistics to describe the reliability of GPS time series has been significantly overly optimistic, in part due to the lack of time correlation being taken into account. One approach to overcome this limitation of white statistics is to estimate a power law and white noise model

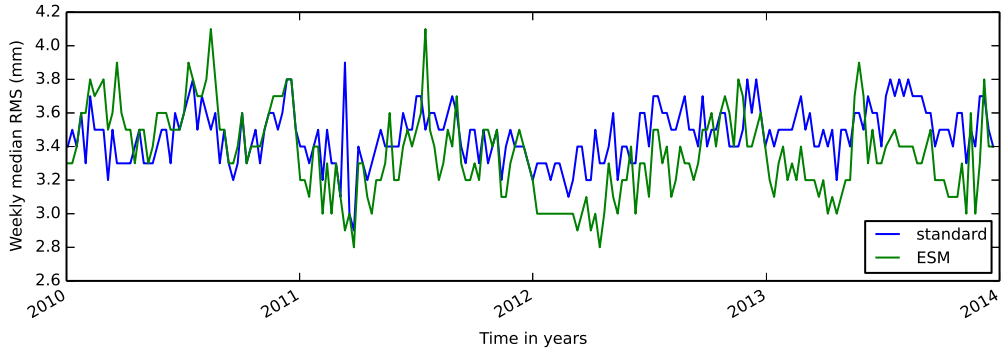

(a) Weekly median RMS for the Standard and ESM solutions

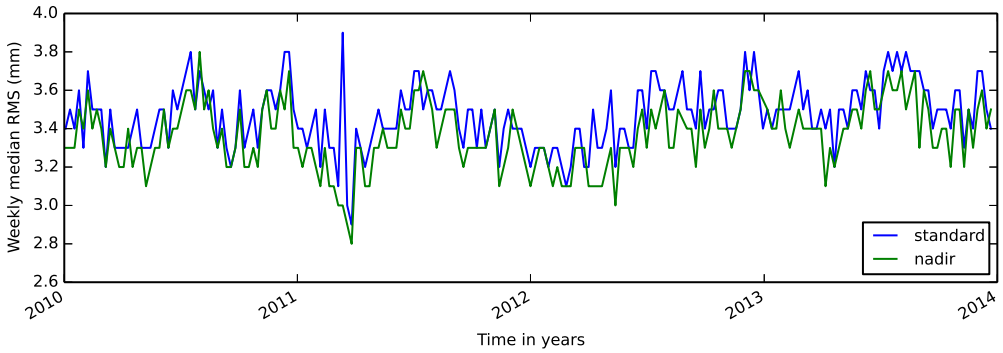

(b) Weekly median RMS for the Standard and nadir solutions

Figure 6.8: Comparison of the median RMS of weekly height estimates, for all of the stations processed, for the standard solution (blue), the ESM (top - green), and nadir (bottom -green) solutions.

Table 6.2: mean height rate uncertainty derived from a power law + white noise model

Monument Height	Number of stations	Standard (mm/yr)	ESM (mm/yr)	Nadir (mm/yr)
Low (h < 0.2 m)	11	2.8	2.6	1.9
Medium (0.2 < h < 2.0 m)	105	3.1	2.6	2.4
High (h > 0.2 m)	35	2.5	2.2	1.7
All	183	2.9	2.4	2.2

to the residuals of the GPS time series. From the noise model a more realistic uncertainty can be derived for the GPS time series.

For the stable subset of GPS time series we fitted a combination of a power law and white noise model, assuming a non-stationary time series for each solution (see Table: 6.2). The ESM solution performs well reducing the uncertainty from 2.9 to 2.4 mm/yr. The nadir solution produces the time series with the lowest height uncertainty, reducing the uncertainty from 2.9 mm/yr to 2.2 mm/yr.

If we breakup the results by monument height classify low monuments as being below 0.2 m, medium monument being between a height of 0.2 m to 2.0 m, and high monument being greater than 2.0 m, we found that the same pattern was repeated. That is the ESM reduced the uncertainty, but the nadir solution produced the solution with the lowest mean uncertainty.

6.2.1 Solution Spectra

To assess any change in the periodic components of the de-trended coordinates obtained from the different solutions we used a stack of the residual time series using a Lomb-Scargle periodogram [Scargle, 1982]. To obtain a spectral stack we normalised each time series with the median variance obtained from the standard solution. From the selected 180 stations we computed a spectral stack, without annual or semi-annual terms fitted to the de-trended time series (see Fig: 6.9).

For the three different solutions there were significant peaks located at the GPS satellite draconitic year (351.2 $\pm$2.8 days), the average repeat period of GPS satellites in inertial space relative to the sun, and its harmonics, as has been reported by other authors [e.g. Ray *et al.*, 2008; Collilieux *et al.*, 2007; Agnew and Larson, 2007; King and Watson, 2010]. For the ESM solution there is a significant decrease in power at the draconitic. Apart from this the solutions are actually fairly similar in terms of spectral characteristics.

From the position time series the ESM solution produced results, which were on occasion degraded when compared to the standard solution. There was an improve-

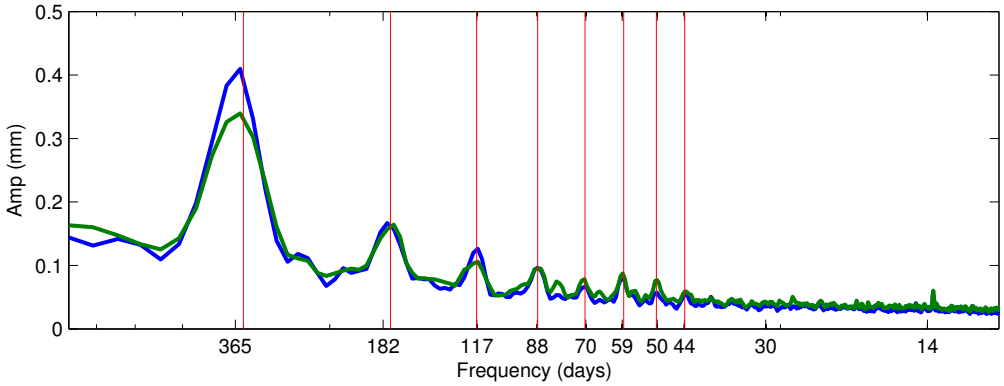

(a) Lomb Periodogram stack for standard (blue) and ESM solution (green)

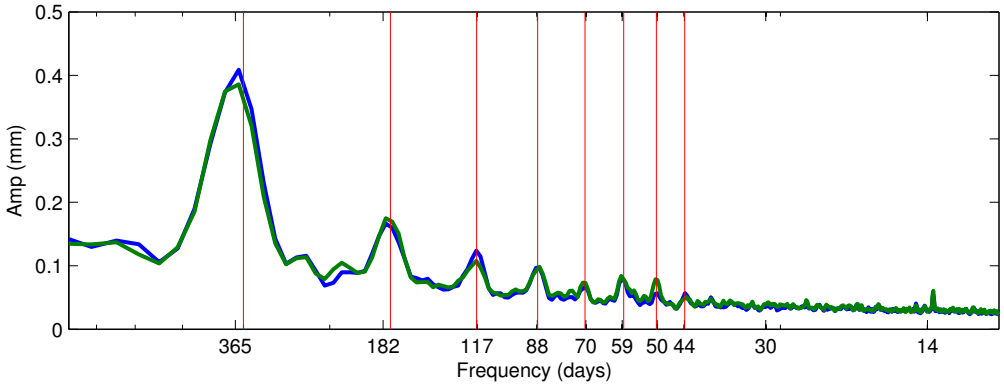

(b) Lomb Periodogram stack for standard (blue) and nadir solution (green)

Figure 6.9: Comparison of a Lomb periodogram stack of the stable stations, for the standard,ESM, and nadir solutions. The draconitic and harmonics are marked by vertical red solid lines.

ment in the random walk noise for the height time series, but this was negated when an annual and semi-annual signal was fitted to the time series. The weekly median position RMS estimates were sometimes significantly lower than the standard solution, and on other occasions were higher than the standard solution. A comparison of spectral stacks of the time series from the standards and ESM solution showed a significant reduction in power at the annual/draconitic periods.When a power law and white noise model was fitted to the GPS time series from the ESM solution, there was a systematic decrease in the velocity uncertainties.

The nadir solution showed consistent improvement in the GPS time series for the random walk noise model, median weekly RMS statistics, velocity uncertainties and spectral stack comparisons. This consistent performance across all of the position time-series metrics is an encouraging sign that the modelling has been effective, without introducing any detrimental effects.

6.3 Orbit overlaps

In generating the daily orbit solutions, the orbit arcs are extended out by 2.5 hours each side of the day boundary. By analysing the difference in solutions at these overlapping boundaries we can obtain and independent measure of the orbit precision. Figure 6.10 shows the mean RMS of the orbit overlaps for all of the satellites as a function of the total difference in position, and the difference in the radial, along, and cross-track directions.

In general the variation in overlap differences with time corresponds to variations in performance among satellites over time, such as during Earth eclipse periods, especially when the eclipsing occurs across the day boundary. Conversely the magnitude of an overlap difference may occasionally be small due to a fortuitously good agreement for a satellite orbit between two successive days.

Comparing the mean RMS of the orbit overlap errors for all satellites in the radial, along and cross track components obtained from the standard and nadir solution reveals a small and consistent improvement from the nadir solution (see Fig: 6.11). Analysing a time series of orbit overlap from one satellite (see Fig: 6.12) shows that there are on occasions a degradation in the consistency of the orbit overlaps, compared to the standard solution, however there was a net improvement in the consistency or the orbit overlaps for PRN 29 of 7 mm in RMS error.

While the ESM solution shows a larger improvement in the radial and cross track directions, this comes at the cost of a degradation in precision for the along track direction.

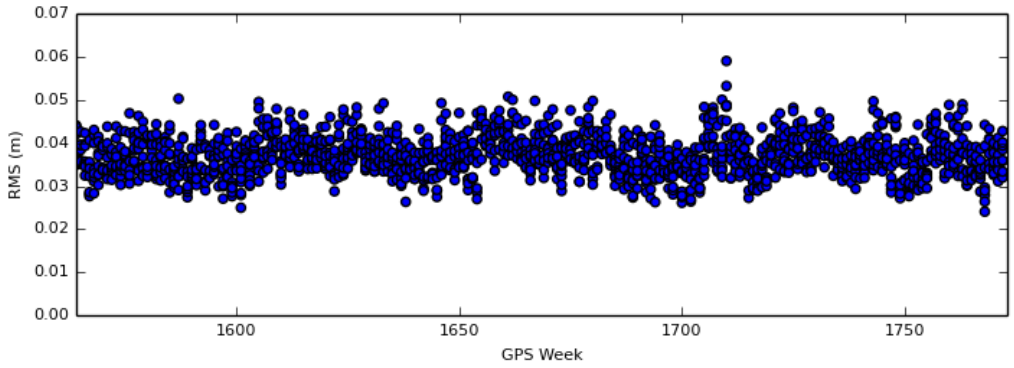

Figure 6.10: Overlap differences in Total position for the standard solution

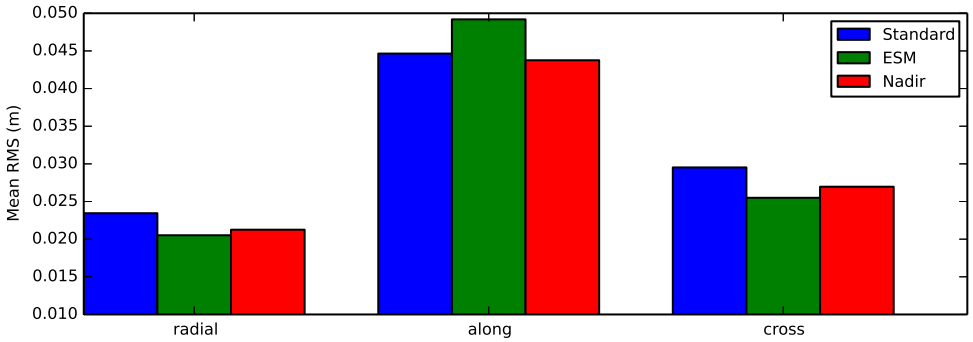

Figure 6.11: Mean RMS Orbit overlap error, broken down into radial, along and cross track components obtained from the standard, ESM, and nadir solutions

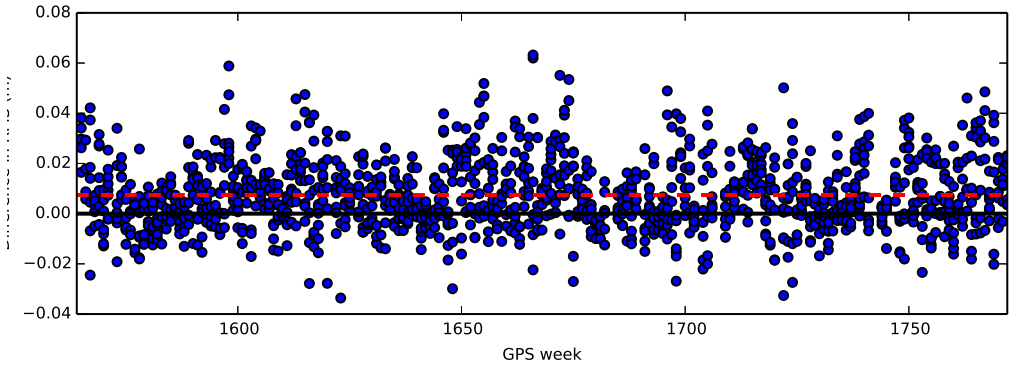

Figure 6.12: Mean difference in the RMS between the standard solution and the nadir solution orbit overlap errors, for the radial component of satellite PRN29. The red-dashed line is the mean rms difference (0.007m), a positive difference indicates that the nadir solution orbits have a closer agreement

6.3.1 Periodicities in orbit overlaps

In order to reduce the spectral noise and search for common mode signals, spectra for all satellites have been stacked then averaged at each frequency step. Figure 6.13 shows the power spectrum of the stacked orbit overlap differences using the lomb-scargle periodogram for the three different processing solutions.

For all three solutions there is a background of declining power with frequency indicative of temporally correlated orbit errors. The overall continuum could be consistent with the power law behaviour close to flicker noise process commonly seen in GPS time series [e.g Williams *et al.*, 2004]. The high frequency noise is does not appear to be significant.

The standard solution (see Fig: 6.13(a)) has peaks near 28, fortnightly, weekly and daily periods. There are also sharp peaks in power at the weekly and daily periods. However these peaks are not present in the ESM and nadir solutions (see Fig: 6.13(b) and Fig: 6.13(c)). For the nadir solution this is an indicative sign that the adjustment to nadir PCV may removing some of the systematic errors in the satellite specific errors.

For the ESM, this was an unexpected result, and indicates that the site-specific models have absorbed some of the satellite specific errors. The issue is further compounded as the application of the ESM appears to re-distribute the errors in the orbit modelling in an inconsistent manner, with improvements in some components (radial and cross), but a degradation in the along track. This goes against the objectives of the ESM technique, that is to isolate the errors particular to an individual station without absorbing errors from other geophysical signals, and other error sources.

Whereas the nadir solution appears to be performing well, the magnitude of improvement is smaller than the ESM solution, however it is consistent throughout the time series. The magnitude of improvement in the radial along and cross component is also consistent.

6.3.2 Station and satellite clock estimates

Comparing the difference in the mean of the daily station clock estimates between the standard, ESM, and nadir solutions indicates a small improvement from the ESM and nadir solutions (see Fig 6.14). The ESM solution has an average improvement of 0.62 ps in the mean RMS, whereas the nadir solution had a mean improvement of 0.52 ps. Both solutions appear to show a consistent improvement with time.

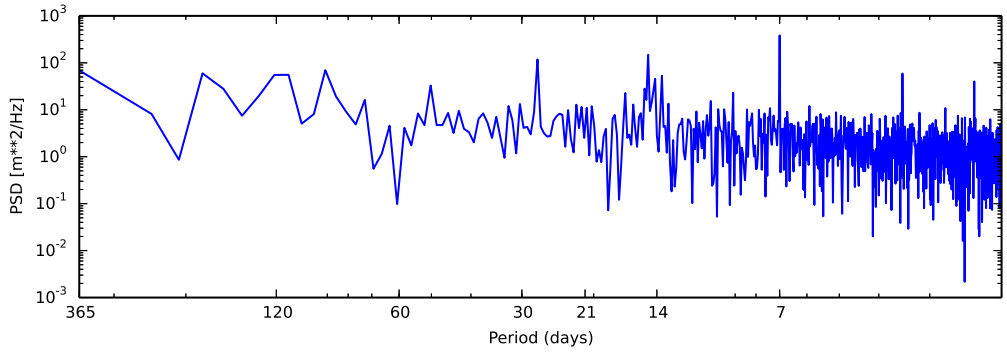

(a) PSD of Orbit overlaps from the standard solution

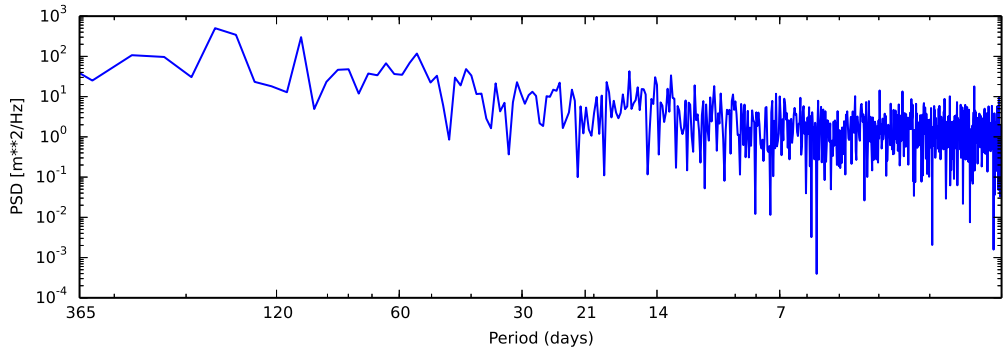

(b) PSD of Orbit overlaps from the ESM solution

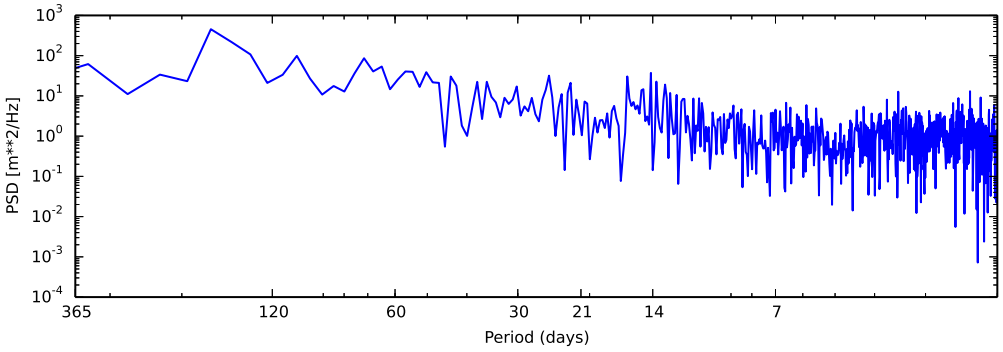

(c) PSD of Orbit overlaps from the nadir solution

Figure 6.13: PSD of Orbit overlaps for the different solutions

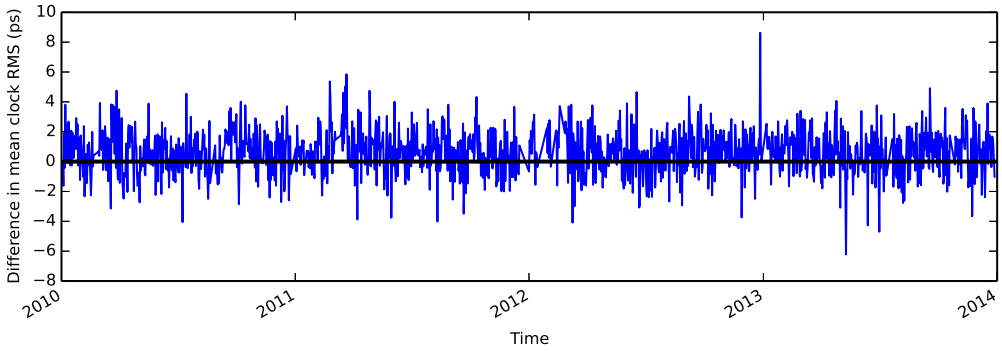

(a) standard - esm (0.62 ps)

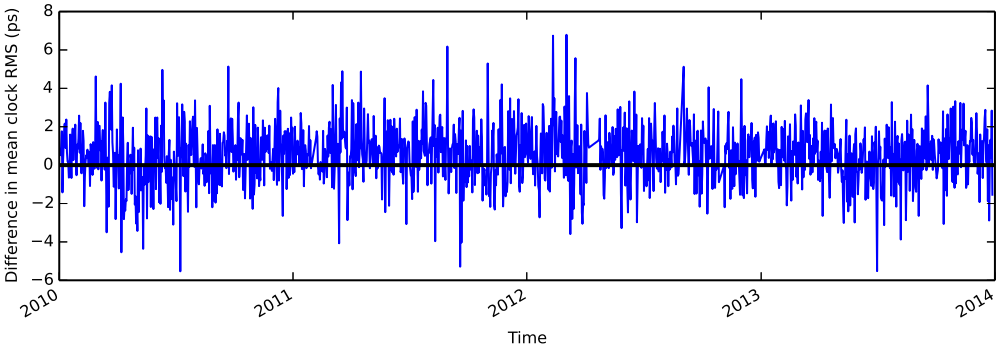

(b) standard - nadir (0.52 ps)

Figure 6.14: The difference in daily mean of station clock rms, between the standard, ESM and nadir solutions

6.4 Comparison with GRACE estimates of elastic deformation

We have obtained estimates of the elastic deformation of the surface of the earth as a time series for a selected number of GPS stations using the ANU GRACE data visualisation tool[Darbeheshti *et al.*, 2013]. This uses the spherical harmonic models produced by GRGS[Bruinsma *et al.*, 2010], which are provided at degree and order 50. The vertical deformation is computed using the empirical expression provided by [Purcell *et al.*, 2011]. We then compared the estimate of elastic deformation for the vertical component with the GPS height time series from the standard, ESM, and nadir solutions. The difference in the vertical component from the GPS time series and the estimated elastic deformation was computed and then the RMS of the differenced time series was calculated and tabulated in Table 6.3. A decrease in the RMS from the standard solution indicates that the modelling that has been improved and better matched the geophysical deformation occurring at the station.

The application the ESM modelling produced a variable level of improvement, for some stations there was a significant improvement in the agreement with the GRACE estimates (e.g. ALIC, DARW and MCM4), however for other stations there was actually a degradation in the agreement with the elastic estimates (e.g. YAR2, MAC1, etc.). However the application of the Nadir modelling technique saw a significant systematic improvement for all of the Antarctic stations in the range of 15 to 21 %. For other stations at mid latitudes there was a minor improvement.

For all of the time-series listed in Table 6.3, and for each solution, there was a phase lag in the amplitude of the estimated Grace elastic estimate and the GPS height time series. The elastic deformation estimates from GRACE were also significantly smaller in magnitude than the GPS height variations. The improvements in correlation between the two techniques can be largely attributed by the reduction in magnitude of the GPS height component through the application of the modelling technique, rather than an improvement in correlation with the phase of the estimated GRACE elastic deformations.

6.5 Summary

The ESM technique produced a larger magnitude of improvement for some of the position estimates, however this was not consistent throughout the time series. This pattern was also apparent in the orbit overlaps where there was an improvement in the radial and cross, but a degradation in consistency for the along track component. It was also apparent from the nadir residuals, obtained after the ESM modelling had

Table 6.3: RMS of differenced time series of GPS Height - GRACE height elastic deformation, for the standard, ESM, and nadir solutions.

Station	Standard RMS (mm)	ESM RMS (mm)	difference (%)	nadir RMS (mm)	difference (%)
ALIC	5.72	4.99	13%	5.68	1%
CEDU	5.45	5.08	7%	5.59	-2%
DARW	7.45	6.72	14%	7.18	4%
STR1	4.84	5.25	-8%	4.65	4%
YAR2	4.73	5.07	-7%	4.59	3%
YAR3	4.19	4.49	-7%	4.06	3%
ONSA	4.96	4.60	7%	5.14	-4%
MCM4	7.57	6.39	16%	6.02	20%
MAW1	5.81	5.58	4%	4.89	15%
DAV1	5.84	5.67	3%	4.74	19%
KAT1	6.01	5.59	7%	5.85	3%
KAT2	6.65	6.23	6%	6.26	5%
WTZS	6.01	5.84	3%	5.38	10%
WTZR	5.15	5.42	-5%	4.91	5%
GODE	5.20	5.63	-8%	4.96	5%
VESL	6.17	5.95	4%	5.08	18%
SYOG	5.35	4.57	15%	4.24	21%
KERG	8.34	8.46	-1%	8.23	1%
MAC1	4.85	5.26	-8%	4.67	4%
DUM1	7.90	7.14	10%	7.18	9%
OHI2	7.07	6.54	7%	6.61	6%
ROTH	10.34	9.90	4%	10.25	1%
RIO2	4.84	5.72	18%	4.69	3%
PARC	7.95	7.88	1%	7.74	3%

been applied, that the impact upon orbit parameters could be significantly detrimental to some satellites. If the ESM approach is in fact absorbing the orbit modelling errors into the station models, then this may explain why there was a large reduction in the power of the station stacked periodogram near the draconitic/annual period.

For the ESM approach, it is best to derive this model and apply this model in an orbit fixed solution. This will help to mitigate the effects the ESM has in absorbing some of the satellite dependent errors into the station model. This could be significant for periods when there is significant constellation change, and where the SVN nadir model is in error.

The nadir modelling technique performed well, with consistent incremental improvements in all of the estimates analysed. Encouragingly this was consistent throughout the time series. There was also a significant level of improvement, of almost 1 mm/yr, in the level of uncertainty for the height rate (based on the power law + white noise model) for all of the stations which had the nadir model applied.

Comparing the phase residuals at each station obtained after each modelling technique had been applied indicates that the site-specific estimation component of the nadir technique could be improved. We would recommend estimating for the nadir PCV corrections use a PWL fit to the residuals for each satellite, but to then use these satellite specific corrections to adjust the station-stacked phase residual before a block median is applied.

Close inspection of the nadir dependent residuals, after the nadir technique has been applied, indicates that this technique could be improved, as the residuals increased for some satellites. This could be improved by only applying the nadir corrections, which have a significant departure from the a priori nadir PCV model. A first step would involve screening out any corrections which do not have enough observations to form a reliable model, these can be easily distinguished by there jig-saw pattern at the high and low nadir angles, or a threshold where a minimum number of observations required could be set. As the certainties obtained from the PWL fit are overly optimistic we recommend calculating the RMS of each satellites nadir correction model, and only applying those with an RMS greater than 0.58 mm.

Chapter 7

Conclusion

This body of work proposes a method to model site-specific and satellite-specific effects based upon post-fit carrier phase residuals obtained from a least squares solution. The techniques detailed here are applicable to historic time series as well as future data sets, and have the potential for use in commercial applications such as real-time kinematic processing. The results obtained from the modelling technique are straightforward to implement into other processing packages without the need for any major re-development of the code. However to ensure the most consistent results it is best to apply the model using the same modelling techniques used to derive the empirical model.

I confirmed the theoretical findings in this thesis that residuals can be used to recover unmodelled biases through a comprehensive range of simulations. The simulations demonstrated that the propagation of multipath into GPS estimates is complex. The magnitude and characteristics of the resulting errors introduced into the GPS time series depends on many factors, such as the immediate local surrounding environment to the station, antenna height, the antenna design characteristics as well as the station location. The presence of multipath will introduce a time-correlated noise into the time series, which will be non-stationary, and often not sufficiently characterized by one particular noise model. This can significantly increase the uncertainty of the velocity estimates, thus degrading the utility and reliability of GPS estimates. Antennas mounted near planar reflectors are more likely to introduce significant biases into the estimates. I therefore recommend that antennas be mounted at least 0.5 m, or preferably as far as practical away from planar reflectors underneath the antenna.

Visual inspection of the stacked phase residuals for each station reliably detected multipath sources, which could be verified by station photos. Creating an ESM model is a straightforward task, and a reliable model can be achieved with a minimum of 120 days of stacked phase residuals with a grid resolution of 0.5°. Application of the ESM to kinematic processing of short baselines resulted in significant improvements

in positioning of over 10 mm, when compared to terrestrial survey results. There was also a significant reduction in the variance of the solution, spectral analysis using FFT and wavelets confirmed a substantial reduction in high frequency components.

Producing a site model using the nadir technique is more computationally intensive, requiring a big data set from a large global network observed over several years in order to obtain a reliable model. Application of the models, derived from the nadir technique, produces a consistent improvement for all of the position time-series investigated, as well as improving the reliability of the derived IGS products. In particular we found that the removal of the site-specific effects, using this technique, improved the reliability of the velocity measurements.

The consistent improvements seen throughout the time series and across all of the estimated parameters obtained from applying the nadir technique suggest that the modelling methodology may be suitable for mitigating site-specific and satellite-specific effects for reference frame determination.

Further testing is required to ensure that the ESM technique is not absorbing errors from other mismodelling effects. For instance, in the global network scenario, investigating the impact of applying and not applying non-tidal loading would be worthwhile. To further prove the validity of the modelling technique it would be worthwhile attempting to introduce a long term time series derived using this methodology into a multi-technique combination to help assess if it is having a positive impact on absolute positioning.

Appendix A

A.1 Reference systems

A.1.1 International Earth Rotation and Reference Systems Service

The IERS consists of a large number of facilities and sub-groups that provide key functions and services to the geodetic community. The facilities include the central bureau, International Terrestrial Reference System (ITRS) combination centres, in addition to technique centres, product centres, research centres, and research centres. The IERS board of directors and working groups also have an important role in the community. Numerous organisations contribute to the IERS, either directly or indirectly, via different autonomous, independent services. One key contributor is the International Global Navigation Satellite Systems Service (IGS, also called the International GNSS Service), which jointly runs a technique centre with the IERS. The IERS provides the following services:

- Earth orientation data
- International Celestial Reference Frame (ICRF)
- International Celestial Reference System (CRS)
- International Terrestrial Reference Frame (ITRF)
- International Terrestrial Reference System (TRS)
- geophysical fluids data
- development and maintenance of the IERS conventions

A.1.2 International GNSS service

The IGS is a joint international activity, involving more than 200 participating organisations in over 80 countries. It provides high quality GPS data and support to

the geodynamic and geodetic communities, such as enabling GPS data to be used for earthscience research. IGS services include the standardisation of equipment, site selection and preparation, data handling and analyses are fundamental pre-requisite enabling the scientific use of GPS products. Some critical IGS services are the generation of precise GPS satellite orbits, clocks and additional by-products, such as measurement of the earth rotation parameter (ERP) (Mueller, 1993). The IGS was initially established in 1992 as a test campaign, followed by a pilot project which continued until the IGS officially started on the 1st of January 1994 (Beutler et al., 1999). Since its establishment, its purpose has not changed significantly up to the present day. IGS products (such as GPS orbit and clock solutions) continue to serve as the de-facto world standard for high-precision GNSS applications (IGS, 2008).

In addition to these core data products, the IGS defines and provides standards for GNSS-related file formats and processing strategies (Kouba, 2009). It also provides for free the GNSS observation data from hundreds of globally distributed GNSS tracking stations (IGS, 2013).

IGS working groups and pilot projects

The IGS has a number of working groups on high interest topics to the IGS and the geodynamic and geodetic communities. These include working groups on antennas, bias and calibration, improving the IGS products and infrastructure, and a working group for the data centre. Within the Working Groups, there is structure for the establishment and evaluation of pilot project outcomes to enable new capabilities and products to be envisioned, developed, tested prior to being implemented in production.

These pilot projects (such as the IGS Multi-GNSS Experiment (MGEX) and others) enable the IGS to keep up-to-date with ongoing changes in the GNSS environment and to further develop and improve IGS standards and products. The IGS working groups and pilot projects are integral to maintaining the its role as the leading international provider of geodynamic and geodetic services.

The Antenna Working Group is a useful example of the valuable services provided by the IGS. The Antenna Working Group coordinates IGS research activities relating to GNSS receiver and satellite antenna characterisation (including the phase centre location), and maintains the official IGS antenna file (Schmidt, 2013). The AWG develops standard antenna file formats, such as ANTEX, and maintains the official IGS antenna files relating to naming convention, reference point definition, phase centre corrections, etc. This information service and standard file formats assist the production of consistent IGS products.The knowledge and the outcomes

produced by the AWG and other working groups of the IGS are indispensable to high accuracy GNSS analysis.

A.1.3 Reference systems and realisations

The key reference systems used in this work is the Internal Terrestrial Reference System (TRS) provided by the IGS. The TRS describes terrestrial processes, positions and time. In GPS analysis, the TRS is used to produce coordinate and velocity estimates of a selected set of stations. The kinematics of the stations can be observed using a range of complementary geodetic techniques, including GNSS, Very Long Baseline Interferometry (VLBI), Lunar Laser Ranging(LLR), Satellite Laser Ranging (SLR) and Doppler Orbitography and Radio positioning Integrated by Satellite (DORIS). GPS plays a major role in the ITRF combination by linking together the other observational techniques [Altamimi and Collilieux, 2009].

The accuracy of the ITRF scale is currently limited to approximately 1 part-per-billion (ppb), i.e. a temporal stability of 0.05 ppb/yr [Altamimi *et al.*, 2011]. This total error budget includes systematic errors from the VLBI and SLR, and also the GPS. Analysis of the ITRF2008 local tie residuals revealed large discrepancies in the height component, which might have been caused by the presence of un-calibrated radomes which cover the GPS antennas, in addition to other site-specific errors Altamimi *et al.* [2011]. In this thesis study we have used the IGS realisation IGS08 (Rebischung et al., 2012). Reference systems are necessary for measurement of many important earth science studies, including:

- the rotation and gravity field of the Earth;
- global and regional sea level change;
- tectonic motion and deformation;
- postglacial rebound;
- geocenter motion;
- large-scale land deformation due to earthquakes; and
- local subsidence.

Only space geodesy is able to produce a sufficiently precise global reference frame suitable for these applications.

Appendix B

B.1 GPS observation modelling

In the following representation of the observation equation, for reasons of clarity the different effects are grouped according to their characteristics, such as relativistic effects (rel), clock errors (clk), the propagation path related effects, split in atmospheric Troposphere(Trop), and Ionosphere (Ion), and multipath (mp) delays, site displacements (site), and antenna dependent delays (ant). For carrier phase observations the phase wind-up (pwu) and the unknown number of ambiguities (N) need to be considered. All insufficiently modelled disturbances are finally absorbed by the measurement error (ϵ)

$$\phi(t) * \lambda = \rho(t)_{rec}^{sat} + rel(t) + clk(t) + Trop_{\phi}(t) - Ion_{\phi}(t) + site(t) + ant_{\phi}(t) + mp\phi(t) + \epsilon_{\phi}(t) + pwu(t) + N\lambda_{L1} \quad \text{(B.1)}$$

Linear combinations (LCs) are combinations of measurements belonging to the same link and to the same epoch. LCs are designed to optimise the observation characteristics for specific tasks. There are two main objectives for the formation of LC. The first objective is the mitigation of errors such as the ionospheric delay. The second objective is the generation of observations with different wavelengths, required to facilitate the recovery of the integer ambiguities. It is possible to generate observations with different wavelengths (λ) or different sensitivities to atmospheric and environmental disturbances. However, the advantages of LCs are accompanied by increased noise and a loss of the physical observation characteristics. The noise of the different LCs can be determined using the law of error propagation. Table B.1 summarises the wavelength and the noise characteristics of the introduced ionosphere-free linear combination (L3).

Table B.1: The advantages gained from the ionosphere-free linear combination is a significant decrease in ionosphere noise, however this comes at the expense of an increased measurement noise.

LC / Carrier	λ [m]	Noise Rel. to L1	Iono.Delay Rel. to L1
L1	0.19	1.00	1.00
L2	0.24	1.28	1.63
L3 ($L1 - \frac{f_{L2}}{f_{L1}} L2$)	0	3.22	0.00

B.1.1 Ionosphere free linear combination

For most applications, the ionospheric delay on signals cannot be sufficiently modelled. The ionosphere-free L3 is the basis of most GNSS processing approaches. This combination aims to mitigate the impact of the first-order ionospheric delay by the combination of observations on two frequencies. The mathematical model of the undifferenced (or one-way) carrier phase measurement has been given earlier (eqn: B.1). If we neglect the satellite and receiver clock error terms, which are eliminated during double-differencing, and the troposphere and orbit biases which are significantly reduced for short baselines then:

$$\phi(t) * \lambda = \frac{f_1}{c} * \rho(t)^{sat}_{rec} - \frac{f_1}{c} Ion_{\phi_{L1}}(t) + N\lambda_{L1} \tag{B.2}$$

$$\phi(t) * \lambda = \frac{f_1}{c} * \rho(t)^{sat}_{rec} - \frac{f_1}{c} Ion_{\phi_{L2}}(t) + N\lambda_{L2} \tag{B.3}$$

Multiplying each of the phase observations (in units of cycles) by the signal frequency, and then differencing them gives:

$$f_1 * \phi_{L1} - f_2 * \phi_{L2} = \frac{f_1^2 - f_2^2}{c}\rho - \frac{1}{c}(f_1^2 - Ion_{L1} - f_2^2 Ion_{L2}) + f_1 N_1 - f_2 N_2 \tag{B.4}$$

The second term of equation B.4 is equal to zero, due to the following relation: The effect of the ionosphere on GPS observations can be considered on terms of the time delay (τ_{ion}), phase change (ϕ_{ion}) or range (or group delay (δ_{ion}). A first order approximation for the ionosphere bias is:

$$\tau_{ion} = \frac{\phi_{ion}}{f} = \frac{\delta_{ion}}{c} \approx (1.35x10)\frac{STEC}{f^2} \tag{B.5}$$

where f is the signal frequency in (Hz), and $STEC$ is the Slant Total Electron Content of a column of ionosphere condensed onto a disc, expressed as the number of free electrons per square metre (el/m^2). The ionosphere causes the integrated car-

rier phase count to decrease (that is the apparent phase velocity is greater than the velocity of light). Note that the time delay is proportional to the inverse of the frequency squared. That is higher frequencies are less affected by the ionosphere, and hence the ionosphere time delay for L1 observation (1575.42 Mhz) is less than for L2 observations * 1227.60 MHz). The relationship between the time delays on the two frequencies f_1 and f_2 due to the ionosphere is:

$$f_1^2 \delta_{ion}(L1) = f_2^2 \delta_{ion}(L2) \tag{B.6}$$

So the L2 ionosphere effect is approximately 1.646 times that on L1 ($1.646 \approx f_1^2/f_2^2$). Hence equation B.5 simplifies to:

$$\frac{f_1\phi_{L1} - f_2\phi_{L2}}{f_1^2 L_1 - f_2^2 L_2} = \frac{1}{c}\rho + \frac{f_1 N_{L1} - f_2 N_{L2}}{f_1^2 L_1 - f_2^2 L_2} \tag{B.7}$$

In order to combine the L1 and L2 phase observations, which are in units of cycles, they have to be converted to the same units, for example, scaling by the L1 frequency:

$$\frac{f_1(f_1\phi_{L1} - f_2\phi_{L2})}{f_1^2 L_1 - f_2^2 L_2} = \frac{f_1}{c}\rho + \frac{f_1(f_1 N_{L1} - f_2 N_{L2})}{f_1^2 L_1 - f_2^2 L_2} \tag{B.8}$$

Which gives the following *corrected* L1 phase measurement:

$$\phi_{L1ion-free} = \alpha_1\phi_{L1} + \alpha_2\phi_{L2} \tag{B.9}$$

$$= \phi_{L1} - \frac{f_2}{f_1}\phi_{L2} \tag{B.10}$$

$$= \frac{f_1}{c}\rho + \alpha_1 N_1 + \alpha_2 N_2 \tag{B.11}$$

$$\alpha_1 = \frac{f_1^2}{f_1^2 - f_2^2} \approx 2.546 \tag{B.12}$$

$$\alpha_2 = \frac{-f_1 f_2}{f_1^2 - f_2^2} \approx -1.984 \tag{B.13}$$

Eq B.9 has the exact form of the original raw carrier beat phase observations, except that the integer ambiguity term is replaced by the linear combination of the L1 and L2 ambiguities. This is known as the ionosphere-free LC, or simply L3. The relationship between the L1, L2 and L3 cycles, where the units of L1 wavelength, is:

$$L3_{(L1cycles)} \approx 2.546 L1_{(L1cycles)} - 1.984 L2_{(L2cycles)} \tag{B.14}$$

In order to obtain the L3 observable in units of metres, both sides of eq B.9 have to be multiplied by λ_1. ÂŁ

Bibliography

Agnew, D. and Larson, K. (2007). Finding the repeat times of the GPS constellation. *GPS Solutions*, **11**, 71–76. (cited on pages 12, 21, and 116)

Alber, C., Ware, R., Rocken, C., and Braun, J. (2000). Obtaining single path phase delays from GPS double differences. *Geophys. Res. Lett.*, **27**. (cited on pages 19, 21, and 63)

Altamimi, Z. and Collilieux, X. (2009). IGS contribution to the ITRF. *Journal of Geodesy*, **83**, 375–383. 10.1007/s00190-008-0294-x. (cited on page 131)

Altamimi, Z., Collilieux, X., and M??tivier, L. (2011). ITRF2008: an improved solution of the international terrestrial reference frame. *Journal of Geodesy*, **85**, 457–473. 10.1007/s00190-011-0444-4. (cited on pages 100 and 131)

Axelrad, P., Comp, C., and MacDoran, P. (1994). Use of Signal-To-Noise Ratio for Multipath Error Correction in GPS Differential Phase Measurements: Methodology and Experimental Results. In *Proceedings of the 7th International Technical Meeting of the Satellite Division of The Institute of Navigation (ION GPS 1994)*, pages 655–666. (cited on pages 18 and 21)

Baire, Q., Bruyninx, C., Legrand, J., Pottiaux, E., Aerts, W., Defraigne, P., Bergeot, N., and Chevalier, J. (2013). Influence of different GPS receiver antenna calibration models on geodetic positioning. *GPS Solutions*, pages 1–11. (cited on pages 6 and 45)

Bedford, L., Brown, N., and Walford, J. (2009). Leica AR25 White Paper. Technical report, Leica Geosystems. (cited on page 14)

Benton, C. J. and Mitchell, C. N. (2011). Isolating the multipath component in GNSS signal-to-noise data and locating reflecting objects. *Radio Science*, **46**(6). (cited on page 18)

Beutler, G., Bauersima, I., Botton, S., Gurtner, W., Rothacher, M., and Schildknecht, T. (1987). Accuracy and biases in the geodetic application of the Global Positioning System. *Mitt. Satell.-Beobachtungsstn. Zimmerwald, Nr. 22, 18 pp.*, **22**. (cited on page 40)

Beutler, G., Brockmann, E., Gurtner, W., Hugentobler, U., Mervart, L., Rothacher, M., and Verdun, A. (1994). Extended orbit modeling techniques at the code processing center of the international GPS service for geodynamics (IGS): theory and initial results. *Manuscr. Geod.*, **19**, 367–386. (cited on page 27)

Bilich, A. and Larson, K. M. (2007). Mapping the GPS multipath environment using the signal-to-noise ratio (SNR). *Radio Sci.*, **42**(6). (cited on pages 18 and 21)

Bilich, A. and Mader, G. (2010). GNSS absolute antenna calibration at the national geodetic survey. In *Proceedings of the 2010 ION GNSS Conference*. (cited on page 4)

Bock, Y., Nikolaidis, R. M., de Jonge, P. J., and Bevis, M. (2000). Instantaneous geodetic positioning at medium distances with the global positioning system. *Journal of Geophysical Research*, **105**. (cited on page 18)

Boehm, J., Niell, A., Tregoning, P., and Schuh, H. (2006a). Global mapping function (GMF): A new empirical mapping function based on numerical weather model data. *Geophys. Res. Lett.*, **33**. (cited on pages 1, 26, and 27)

Boehm, J., Werl, B., and Schuh, H. (2006b). Troposphere mapping functions for GPS and very long baseline interferometry from european centre for medium-range weather forecasts operational analysis data. *J. Geophys. Res.*, **111**. (cited on page 1)

Bos, M., Fernandes, R., Williams, S., and Bastos, L. (2013). Fast error analysis of continuous GNSS observations with missing data. *Journal of Geodesy*, **87**(4), 351–360. (cited on pages xiv, 34, 49, and 50)

Braun, J. J. (2007). Assessing the Impact of the SCIGN Radome on Geodetic Parameter Estimates. Technical report, UNAVCO, UCAR/COSMIC Program. (cited on pages 8 and 46)

Bruinsma, S., Lemoine, J.-M., Biancale, R., and Valès, N. (2010). CNES/GRGS 10-day gravity field models (release 2) and their evaluation. *Advances in Space Research*, **45**, 587–601. (cited on page 123)

Byun, S. H., Hajj, G. A., and Young, L. E. (2002). Development and application of GPS signal multipath simulator. *Radio Science*, **37**(6), 10–1–10–23. (cited on page 17)

Carrère, L., Lyard, F., Cancet, M., Guillot, A., and Roblou, L. (2012). Fes2012: A new global tidal model taking advantage of nearly 20 years of altimetry. In *Proceedings of meeting*, volume 20. (cited on page 60)

Choi, K. (2007). *Improvements in GPS precision: 10 Hz to one day*. Ph.D. thesis, University of Colorado, Boulder. (cited on pages 18, 19, and 21)

Choi, K., Bilich, A., Larson, K. M., and Axelrad, P. (2004). Modified sidereal filtering: Implications for high-rate GPS positioning. *Geophysical Research Letters*, **31**. (cited on pages 12 and 18)

Collilieux, X., Altamimi, Z., Coulot, D., Ray, J., and Sillard, P. (2007). Comparison of very long baseline interferometry, GPS, and satellite laser ranging height residuals from ITRF2005 using spectral and correlation methods. *Journal of Geophysical Research: Solid Earth*, **112**(B12), n/a–n/a. (cited on page 116)

Darbeheshti, N., Zhou, L., Tregoning, P., Mcclusky, S., and Purcell, A. (2013). The ANU GRACE visualisation web portal. *Comput. Geosci.*, **52**, 227–233. (cited on page 123)

Daubechies, I. (1990). The wavelet transform, time-frequency localization and signal analysis. *Information Theory, IEEE Transactions on*, **36**(5), 961–1005. (cited on page 29)

Desai, S., Gross, J., Haines, B. J., and Stowers, D. A. (2013). Verification and Validation of the GNSS Stations at the Prototype Core Site for NASAs Next Generation Space Geodesy Network. In *2013 Fall AGU Meeting, San Francisco, C.A., Poster Presentation G53B-0928*. (cited on page 20)

Dilßsner, F., Seeber, G., Wubbena, G., and Schmitz, M. (2008). Impact of near-field effects on the GNSS position solution. *Proceedings of the 21st International Technical Meeting, ION GNSS-2008, Savannah*, pages 612–624. (cited on pages 6, 18, and 21)

Dorsey, A., Marquis, W., Fyfe, P., Kaplan, E., and Wiederholt, L. (2006). GPS system segments. *Understanding GPSâĂŤprinciples and applications, 2nd edn. Artech House, Norwood*, pages 67–112. (cited on pages xix and 77)

Elòsegui, P., Davis, J. L., Jaldehag, R. T. K., Johansson, J. M., Niell, A. E., and Shapiro, I. I. (1995). Geodesy using the global positioning system: The effects of signal scattering on estimates of site position. *J. Geophys. Res.*, **100**. 10.1029/95JB00868. (cited on pages 7, 12, and 17)

Fancher, K. L., Breidenbach, S., and Geoghegan, C. (2012). Local tie information report IERS network site: Goddard. (cited on pages xvi and 86)

Farge, M. (1992). Wavelet transforms and their applications to turbulence. *Annual Review of Fluid Mechanics*, **24**(1), 395–458. (cited on pages 29, 30, and 31)

Fuhrmann, T., Luo, X., Knapfler, A., and Mayer, M. (2014). Generating statistically robust multipath stacking maps using congruent cells. *GPS Solutions*, pages 1–10. (cited on pages 20 and 21)

Görres, B., Campbell, J., Becker, M., and Siemes, M. (2006). Absolute calibration of GPS antennas: laboratory results and comparison with field and robot techniques. *GPS Solutions*, **10**(2), 136–145. (cited on pages xiii and 5)

Griffiths, J. and Ray, J. (2013). Sub-daily alias and draconitic errors in the igs orbits. *GPS Solutions*, **17**(3), 413–422. (cited on page vii)

Haines, B. J., Desai, S. D., and Born, G. H. (2013). GPS monitoring of vertical seafloor motion at platform harvest. *Advances in Space Research*, **51**(8), 1369 – 1382. Satellite Altimetry Calibration and Deformation Monitoring using GNSS. (cited on pages 19 and 21)

Hatanaka, Y., Sawada, M., Horita, A., Kusaka, M., Johnson, J., and Rocken, C. (2001). Calibration of antenna-radome and monument-multipath effect of GEONET-part 1: Evaluation of the phase map by GEONET data. *Earth Planets Space*, **53**, 23–30. (cited on pages 12 and 17)

Herring, T. A., King, R. W., and McClusky, S. C. (2010). *Documentation for the GAMIT GPS analysis software.* (cited on pages 24 and 27)

Hill, E. M., Davis, J. L., ElÃşsegui, P., Wernicke, B. P., Malikowski, E., and Niemi, N. A. (2009). Characterization of site-specific gps errors using a short-baseline network of braced monuments at yucca mountain, southern nevada. *Journal of Geophysical Research: Solid Earth*, **114**(B11), n/a–n/a. B11402. (cited on page 3)

HofmannWellenhof, B., Lichtenegger, H., and Collins, J. (2012). *Global positioning system: theory and practice*. Springer Science & Business Media. (cited on page 12)

Hurst, Kenneth, J. and Bar Server, Y. (1998). In-situ GPS antenna phase center calibration. In *Proceedings of the Workshop 'GPS/MET Japan Has Come!'*, pages 54–63. (cited on pages 19 and 21)

Iwabuchi, T., Shoji, Y., Sihimada, S., and Nakamura, H. (2004). Tsukuba GPS dense net campaign observations: Comparison of the stacking maps of post-fit phase residuals estimated from three software packages. *Journal of the Meteorological Society of Japan*, **82**(1B), 315–330. (cited on pages 19 and 21)

Jaldehag, R. T. K., Johansson, J. M., Ronnong, B. O., Elòsegui, P., Davis, J. L., Shapiro, I. I., and Niell, A. E. (1996). Geodesy using the Swedish permanent GPS network:

Effects of signal scattering on estimates of relative site positions. *J. Geophys. Res.*, **101**. (cited on page 7)

Kaniuth, K. and Huber, S. (2003). An assessment of radome effects on height estimates in the EUREF network. *EUREF publication*, **12**, 97–102. (cited on page 10)

King, M., Coleman, R., and Nguyen, L. N. (2003). Spurious periodic horizontal signals in sub-daily GPS position estimates. *Journal of Geodesy*, **77**, 15–21. (cited on page 35)

King, M. A. and Watson, C. S. (2010). Long GPS coordinate time series: Multipath and geometry effects. *Journal of Geophysical Research*, **115**. http://dx.doi.org/10.1029/2009JB006543. (cited on pages 1, 12, 14, 17, 35, and 116)

Kouba, J. (2009). A simplified yaw-attitude model for eclipsing GPS satellites. *GPS solutions*, **13**(1), 1–12. (cited on page 27)

Kozakoff, D. J. (2010). *Analysis of radome-enclosed antennas*. Artech House. (cited on page 7)

Larson, K. M., Bilich, A., and Axelrad, P. (2007). Improving the precision of high-rate GPS. *Journal of Geophysical Research*, **112**. (cited on page 18)

Lau, L. and Cross, P. (2007). Development and testing of a new ray-tracing approach to GNSS carrier-phase multipath modelling. *Journal of Geodesy*, **81**, 713–732. 10.1007/s00190-007-0139-z. (cited on pages 17 and 21)

Lyard, F., Lefevre, F., Letellier, T., and Francis, O. (2006). Modelling the global ocean tides: modern insights from FES2004. *Ocean Dynamics*, **56**, 394–415. (cited on pages 26 and 27)

Mader, G. L. (1999). GPS antenna calibration at the national geodetic survey. *GPS Solutions*, **3**, 50–58. 10.1007/PL00012780. (cited on page 4)

Mandelbrot, B. B. and Van Ness, J. W. (1968). Fractional brownian motions, fractional noises and applications. *SIAM review*, **10**(4), 422–437. (cited on page 33)

Meyers, S. D., Kelly, B. G., and O'Brien, J. J. (1993). An introduction to wavelet analysis in oceanography and meteorology: With application to the dispersion of yanai waves. *Monthly Weather Review*, **121**(10), 2858–2866. (cited on page 31)

Moore, M., Watson, C., King, M., McClusky, S., and Tregoning, P. (2014). Empirical modelling of site-specific errors in continuous GPS data. *Journal of Geodesy*, **88**(9), 887–900. (cited on page 21)

Navstar, G. (2004). Global positioning system standard positioning service signal specification. (cited on pages xix and 77)

Park, K.-D., Nerem, R., Schenewerk, M., and Davis, J. (2004). Site-specific multipath characteristics of global IGS and CORS GPS sites. *Journal of Geodesy*, **77**, 799–803. (cited on pages 3 and 21)

Pavlis, N. K., Holmes, S. A., Kenyon, S. C., and Factor, J. K. (2012). The development and evaluation of the Earth Gravitational Model 2008 (EGM2008). *Journal of Geophysical Research: Solid Earth (1978–2012)*, **117**(B4). (cited on page 27)

Penna, N. T., King, M. A., and Stewart, M. P. (2007). GPS height time series: Short-period origins of spurious long-period signals. *Journal of Geophysical Research: Solid Earth*, **112**(B2). (cited on page 35)

Petrie, E. J., King, M. A., Moore, P., and Lavall?e, D. A. (2010). Higher-order ionospheric effects on the GPS reference frame and velocities. *J. Geophys. Res.*, **115**. (cited on pages 26 and 27)

Prüllage, A. (2013). *For the calibration and compensation of multipath effects on GNSS stations in the networking SAPOS Lower Saxony*. Master's thesis, Jade Hochschule Wilhelmshaven Oldenburg Elsfleth, Department of Applied Geodesy, Oldenburg. (cited on page 18)

Purcell, A., Dehecq, A., Tregoning, P., Potter, E.-K., McClusky, S. C., and Lambeck, K. (2011). Relationship between glacial isostatic adjustment and gravity perturbations observed by grace. *Geophysical Research Letters*, **38**(18). (cited on page 123)

Ragheb, A., Clarke, P., and Edwards, S. (2007). GPS sidereal filtering: coordinate- and carrier-phase-level strategies. *Journal of Geodesy*, **81**, 325–335. (cited on pages 18 and 21)

Ray, J., Altamimi, Z., Collilieux, X., and Dam, T. (2008). Anomalous harmonics in the spectra of GPS position estimates. *GPS Solutions*, **12**, 55–64. (cited on pages 12 and 116)

Rodriguez-Solano, C., Hugentobler, U., and Steigenberger, P. (2012). Adjustable box-wing model for solar radiation pressure impacting GPS satellites. *Advances in Space Research*, **49**(7), 1113–1128. (cited on page 26)

Rost, C. and Wanninger, L. (2010). Carrier phase multipath corrections based on GNSS signal quality measurements to improve CORS observations. In *Position Location and Navigation Symposium (PLANS), 2010 IEEE/ION*, pages 1162–1167. IEEE. (cited on page 18)

Rothacher, M. (2001). Comparison of absolute and relative antenna phase center variations. *GPS solutions*, **4**(4), 55–60. (cited on page 70)

Rothacher, M., Gurtner, W., Schaer, S., Weber, R., Schlater, W., and Hase, H. (1996). Azimuth- and elevation-dependent phase center corrections for geodetic GPS antennas estimated from GPS calibration campaigns. In G. Beutler, W. Melbourne, G. Hein, and G. Seeber, editors, *GPS Trends in Precise Terrestrial, Airborne, and Spaceborne Applications*, volume 115 of *International Association of Geodesy Symposia*, pages 333–338. Springer Berlin Heidelberg. (cited on page 4)

Santerre, R. (1991). Impact of GPS satellite sky distribution. *manuscripta geodaetica*, **16**(1), 28–53. (cited on pages 9 and 35)

Satirapod, C. and Rizos, C. (2005). Multipath mitigation by wavelet analysis for GPS base station applications. *Survey Review*, **38**(295), 2–10. (cited on page 21)

Scargle, J. (1982). Studies in astronomical time series analysis. ii - statistical aspects of spectral analysis of unevenly spaced data. *apj*, **263**, 835–853. (cited on page 116)

Schlüter, W., Zernecke, R., Becker, S., Klügel, T., and Thaller, D. (2005). Local ties between the reference points at the fundamentalstation Wettzell. (cited on pages xvi and 95)

Schmid, R. and Rothacher, M. (2003). Estimation of elevation-dependent satellite antenna phase center variations of GPS satellites. *Journal of Geodesy*, **77**, 440–446. (cited on pages xv, 4, 70, and 71)

Schmid, R., Rothacher, M., Thaller, D., and Steigenberger, P. (2005). Absolute phase center corrections of satellite and receiver antennas. *GPS Solutions*, **9**, 283–293. (cited on pages 4 and 6)

Schmid, R., Steigenberger, P., Gendt, G., Ge, M., and Rothacher, M. (2007). Generation of a consistent absolute phase-center correction model for GPS receiver and satellite antennas. *Journal of Geodesy*, **81**, 781–798. 10.1007/s00190-007-0148-y. (cited on pages 1, 6, 26, and 27)

Schmidt, M., Dragert, H., Lu, Y., and Schofield, B. (2003). The Effect of SCIGN Domes on the Vertical Antenna Phase Centre Position in Routine Processing of GPS Data. *AGU Fall Meeting Abstracts*, page B42. (cited on pages 8 and 47)

Schulper, B. R. and Clark, T. A. (2001). Innovation: Characterization the behaviour of geodetic GPS antennas. *GPS World*, **2**, 48–55. (cited on page 4)

Seitz, M., Angermann, D., and Drewes, H. (2013). Accuracy assessment of the ITRS 2008 realization of dgfi: Dtrf2008. In Z. Altamimi and X. Collilieux, editors, *Reference Frames for Applications in Geosciences*, volume 138 of *International Association of Geodesy Symposia*, pages 87–93. Springer Berlin Heidelberg. (cited on page 94)

Torrence, C. and Compo, G. P. (1998). A practical guide to wavelet analysis. *Bulletin of the American Meteorological society*, **79**(1), 61–78. (cited on pages 31 and 32)

Tregoning, P. and Herring, T. A. (2006). Impact of a priori zenith hydrostatic delay errors on GPS estimates of station heights and zenith total delays. *Geophys. Res. Lett.*, **33**. (cited on page 1)

Wanninger, L. and May, M. (2001). Carrier-phase multipath calibration of GPS reference stations. *Navigation*, **48**(2), 112–124. (cited on pages 18, 19, and 21)

Williams, S. D. (2008). CATS: GPS coordinate time series analysis software. *GPS solutions*, **12**(2), 147–153. (cited on page 34)

Williams, S. D. P. (2003). Offsets in Global Positioning System time series. *J. Geophys. Res.*, **108**. (cited on page 33)

Williams, S. D. P., Bock, Y., Fang, P., Jamason, P., Nikolaidis, R. M., Prawirodirdjo, L., Miller, M., and Johnson, D. J. (2004). Error analysis of continuous gps position time series. *Journal of Geophysical Research: Solid Earth*, **109**(B3). (cited on pages 33, 49, and 120)

Woods, A. and Ruddick, R. (2007). The 2007 Yarragadee (Moblas) Local Tie Survey. Technical report, Geoscience Australia. (cited on page 100)

Wu, J. and Hsieh, C.-H. (2010). Statistical modeling for the mitigation of GPS multipath delays from day-to-day range measurements. *Journal of Geodesy*, **84**, 223–232. (cited on page 19)

Wübbena, G. and Schmitz, S. (2011). On GNSS Station Calibration of Near-Field Multipath in RTK-Networks. In *International Symposium on GNSS, Space-based and Ground-based Augmentation Systems and Applications, Berlin*. (cited on pages 18 and 21)

Wübbena, G., Menge, F., Schmitz, M., Seeber, G., and Volksen, C. (1996). A new approach for field calibration of absolute antenna phase center variations. *Proceed-*

ings of the International Technical Meeting, ION GPS-96, Kansas City, pages 1205–1214. (cited on pages 1, 4, and 6)

Wübbena, G., Schmitz, M., F., M., V., B., and Seeber, G. (2000). Automated absolute field calibration of GPS antennas in real-time. *Proceedings of the 13th International Technical Meeting of the Satellite Division of the Institute of Navigation ION GPS 2000, Salt Lake City*. (cited on page 13)

Wübbena, G., Schmitz, M., and Boettcher, G. (2006). Near-field effects on GNSS sites: analysis using absolute robot calibrations and procedures to determine corrections. In *Proceedings IGS Workshop*, pages 8–12. (cited on pages 13, 18, and 21)

Zeimetz, P. and Kuhlmann, H. (2008). On the accuracy of absolute GNSS antenna calibration and the conception of a new anechoic chamber. In *FIG Working Week 2008*. (cited on pages 4 and 6)

Zhang, J., Bock, Y., Johnson, H., Fang, P., Williams, S., Genrich, J., Wdowinski, S., and Behr, J. (1997). Southern california permanent GPS geodetic array: Error analysis of daily position estimates and site velocities. *Journal of Geophysical Research: Solid Earth (1978–2012)*, **102**(B8), 18035–18055. (cited on page 34)